MICROSTRUCTURAL CHARACTERIZATION OF FRICTION STIR WELDED ALUMINUM-STEEL JOINTS

By

ERIN ELIZABETH PATTERSON

A thesis submitted in the partial fulfillment of the
requirements for the degree of

MASTER OF SCIENCE IN MATERIALS SCIENCE AND ENGINEERING

WASHINGTON STATE UNIVERSITY
School of Mechanical and Materials Engineering

AUGUST 2013

UNCLASSIFIED: Distribution Statement A. Approved for public release.

To the faculty of Washington State University:

The members of the Committee to examine the thesis of ERIN ELIZABETH PATTERSON find it satisfactory and recommend that it be accepted.

_____

David P. Field, Ph.D., Chair

_____

Jow-Lian Ding, Ph.D.

_____

Hussein M. Zbib, Ph.D.

ACKNOWLEDGMENTS

I would like to thank Yuri Hovanski with Pacific Northwest National Laboratory for his work producing the dissimilar weld samples used in this study. Without his work, this project would not have been possible. I would also like to thank David Field who has mentored me as his research student for four years, both as an undergraduate and graduate student. His guidance has given me an education that reaches far beyond the classroom.

Funding for this project was provided by the United States Army Tank Automotive Research, Development, and Engineering Center.

MICROSTRUCTURAL CHARACTERIZATION OF FRICTION STIR WELDED ALUMINUM-STEEL JOINTS

Abstract

by Erin Elizabeth Patterson, M.S.
Washington State University
August 2013

Chair: David P. Field

This work focuses on the microstructural characterization of aluminum to steel friction stir welded joints. A lap weld configuration, coupled with scribe technology used for the weld tool, have produced joints of adequate quality, despite the significant differences in hardness and melting temperatures of the alloys. Common to friction stir processes, especially those of dissimilar alloys, are microstructural gradients including grain size, crystallographic texture, and precipitation of intermetallic compounds. Because of the significant influence that intermetallic compound formation has on mechanical and ballistic behavior, the characterization of the specific intermetallic phases and the degree to which they are formed in the weld microstructure is critical to predicting weld performance. This study used electron backscatter diffraction, energy dispersive spectroscopy, optical and scanning electron microscopy, and Vickers micro-hardness indentation to explore and characterize the microstructures of lap friction stir welds between 6111-T4 aluminum and dual phase galvannealed steel, as well as an applique 6061-T6 aluminum armor plate alloy and a wrought homogeneous armor plate steel alloy.

Macroscopic defects such as voids and micro-cracks were observed in the cross-sectional samples, and binary and ternary intermetallic compounds were found to exist at the aluminum-steel interfaces of the steel particles stirred into the aluminum weld matrix and across the interfaces of the weld joints. Energy dispersive spectroscopy chemical analysis identified the intermetallic layer present in the 6061-T6/wrought steel weld as monoclinic Al_3Fe. Dramatic decreases in grain size in the thermo-mechanically affected zones and weld zones evidenced grain refinement through plastic deformation and recrystallization. Crystallographic grain orientation and texture were examined using electron backscatter diffraction. Striated regions in the orientations of the two aluminum alloys were determined to be the result of the severe deformation induced by the complex weld tool geometry. Many of the textures observed in the weld zones and thermo-mechanically affected zones exhibited shear texture components, however there were many textures that deviated from simple shear. Factors affecting the microstructure which are characteristic of the friction stir welding process, such as post-recrystallization deformation and complex deformation induced by tool geometry were discussed as causes for deviation from simple shear textures.

Table of Contents

List of Figures

List of Tables

Dedication

To my parents, Albert and Melanie Diedrich, who provided me with an education and always encouraged me to work hard to achieve my goals,

To my loving husband Loren, whose support and understanding made this work possible.

Chapter One: Introduction and Background

1.1 Benefits of Friction Stir Welding

Friction stir welding (FSW) is a solid state joining process that uses heat generated by a rotating tool plunged into the work piece base materials to create plastic flow in order to stir them together [1,2]. This process creates high strength welds in materials that are difficult or impossible to weld using traditional fusion welding methods because of defects that are produced in the microstructures which are detrimental to mechanical performance [2,3]. It also removes the need for filler metal or shielding gas and eliminates hazards to workers such as fumes, and ultraviolet and electromagnetic radiation [2,4]. Such materials include 2XXX and 7XXX series aluminum alloys; titanium alloys, which have a high affinity for oxygen making them especially susceptible to embrittlement; dissimilar metal combinations like aluminum (Al) and copper (Cu), Al and magnesium (Mg), Mg and steel, or Al and steel; and metal-matrix composites [3-6]. The ability to weld these types of materials is of particular importance for weight reduction in structural components for applications in the marine, aerospace and automotive industries, as well as military applications such as armored combat vehicles where the coupling of light-weight structural components to ballistic protection components is highly beneficial [2,7,8].

Because FSW is a solid state process and does not reach the melting temperatures of the base metal alloys, problems which are associated with fusion welding such as dendritic and eutectic solidification structures, post weld cracking, grain boundary liquation cracking, hydrogen absorption, and porosity in the weld are generally avoidable [4,5,7-12]. The decreased amount of energy input during FSW reduces the residual stresses in the weld and improves mechanical properties and performance compared with fusion welding; typically an FSW

maintains 80-85 percent of the base metal strength of the weaker alloy [5,8-10,12,13]. When using FSW for similar-alloy welds, there are minimal changes to the microstructure within the weld and surrounding regions, despite the significant amount of plastic deformation [9]. FSW in dissimilar metals, on the other hand, can produce rather complex microstructures [14].

1.2 FSW Process

Friction stir welds are performed with a non-consumable rotating tool that consists of a central pin and an upper shoulder. The pin may be cylindrical, tapered, threaded, or shaped with flat sides, or a combination of these. The tool used in this study had a tapered, threaded pin like the one shown in Figure 1 [9,15,16]. In the case of friction stir spot welding (FSSW), a concave shoulder is frequently used to enhance bonding of upper and lower plates [14,17]. Threaded pins help to create a downward flow of material that aids in the mixing within the weld [12]. Schematic diagrams of FSW in the butt weld and lap weld configurations are shown in Figure 2 and Figure 3.

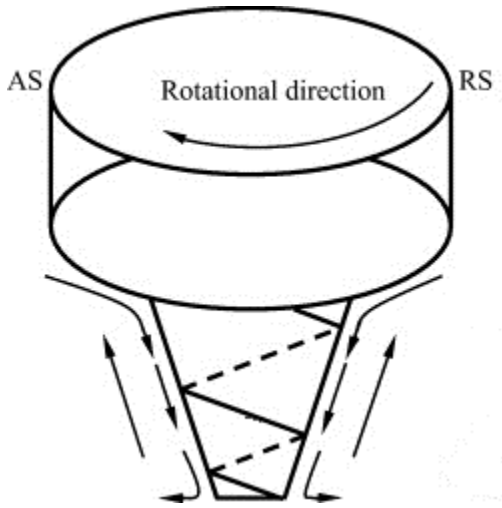

Figure 1 Schematic of material flow around threaded pin [16].

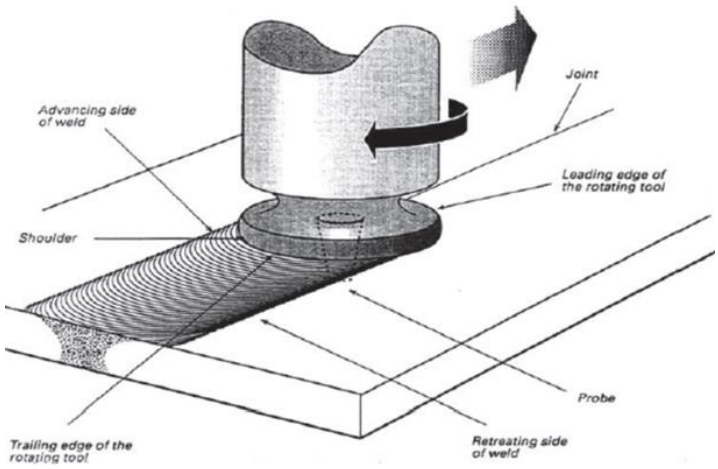

Figure 2 Schematic of friction stir weld in a butt weld configuration [2,15].

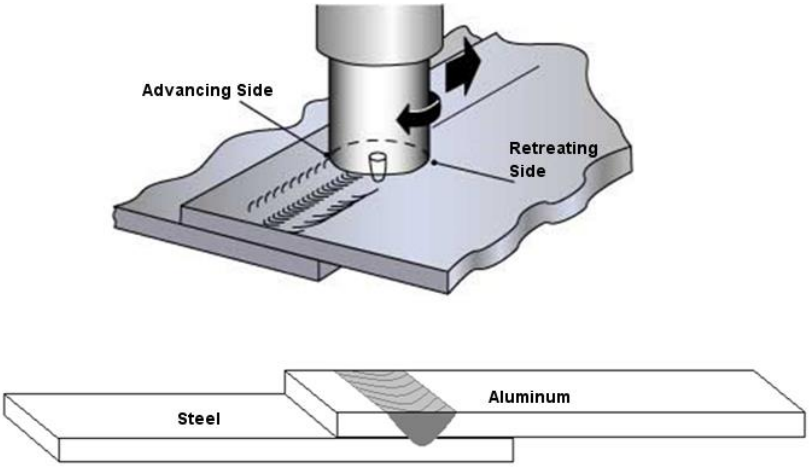

Figure 3 Schematic of friction stir weld in a lap weld configuration [18].

Process parameters include tool dimensions and morphology; tool plunge, rotation, and travel speeds; and rotation direction [1,7,9]. Plunge depth, the width/diameter of the weld, weld temperature, and quality of the bond depend on these parameters [11]. In butt weld configuration for dissimilar alloys, the softer material will generally be placed on the retreating side of the weld and the tool pin may be offset into it, pushing toward the harder metal's faying surface during welding [1,19]. This configuration allows the softer material to be highly plasticized by the rotation around the back of the tool in preparation for adhesion to the faying surface of the other alloy. In the case of a lap weld, the softer material will be placed on top with only the tip of the pin plunged into the harder bottom piece. In some cases the pin will not contact the harder material at all but only create plastic flow in the upper alloy [14,20,21]. Typically, when two metals of very different hardness and melting temperature are joined by FSW, the weld parameters and tool position are selected such that the softer metal will experience more plastic deformation than the harder material to reduce tool wear, prevent overheating of the lower-melting temperature metal, and help ensure better plastic flow of the

material around the tool [1,3,20]. Occasionally, when welding dissimilar metals of significantly different melting points, there can be regions of localized melting [22], but it is not typical of the process. The material chosen for the fabrication of the tool is also important, as base metal alloys such as steel require much harder and more wear-resistant materials like polycrystalline cubic boron nitride (PCBN), and tend to be less commercially available than alloys like H-13 tool steel chosen for FSW in softer alloys like Al and Mg [21,23].

1.3 Tool Technology

In lap weld configuration, bond efficiency is dependent on the ability of the plasticized material of the upper plate to adhere to lower plate, creating a mechanical and sometimes chemical bond. One method of avoiding overheating in lower-melting temperature base materials and wear on the tool is the use of scribe technology. Developed at Pacific Northwest National Laboratory (PNNL) in Richland, WA, scribe technology couples the FSW tool with a carbide cutting tool, or scribe, that is responsible for the stirring action within the harder metal. Without the scribe, the tool pin would need to penetrate deeper into the harder alloy, increasing excess wear to the pin and necessitating higher tool rotation speeds in order to achieve sufficient frictional heat to plasticize the material [24-26]. Because the carbide scribe is much harder than the tool and work piece materials, it prevents these problems and creates higher quality weld joints.

Jana et al. [26] studied the difference in joint performance of lap welds between an AZ31-O Mg alloy and hot-dipped galvanized high strength low alloy (HSLA) and electo-galvanized mild steels using weld tools with and without WC scribes. The tool itself was made from H-13 tool steel and had a convex scrolled shoulder and threaded, tapered pin, much like the

weld tool used in the current study. The weld performed using the tool without the scribe resulted in much lower failure strengths from lap-shear tests than the welds performed using the tool with the scribe. The cross-sectional morphology of the weld was different as well. The weld without the scribe showed a slight depression of the weld interface at the center where the pin tip penetrated into the steel, and slight elevations of the Mg-steel interface on either side of the depressed region relative to the original interface depth. Very few particles of steel were present in the Mg weld nugget. In the welds performed using the tool with the scribe, very distinct hooks of steel were drawn up into the Mg alloy on either side of the weld zone, creating an interlocking mechanical bond. In addition, the scribe also served to "machine" the surface of the steel work piece, breaking off large pieces of steel and stirring them into the Mg weld zone, creating a composite-like structure with the Mg alloy serving as the matrix. Lap-shear samples from the welds performed with the scribe not only produced higher failure stresses but were also more consistent in failure stress than samples from the weld performed without the scribe [26]. Two different weld tools were utilized in the current study, both with convex scrolled shoulders and tapered, threaded pins with scribes affixed to the pin tips, but with different dimensions to accommodate the significant differences in thickness between the plates used for the two welds.

1.4 Microstructure and Mechanical Performance

FSW produces four distinct regions within the microstructure that exhibit different properties and mechanical performance. These regions are the base metal (BM), heat affected zone (HAZ), thermo-mechanically affected zone (TMAZ), and the weld zone (WZ) [4,7-10]. The HAZ typically shows evidence of heating without plastic deformation resulting in grain growth and over-aging of strengthening particles, while the TMAZ experiences plastic

deformation and elongation of the grains as they are extruded around the tool [9]. The severe plastic deformation and heating that occurs in the WZ results in a recrystallized deformation structure to produce fine, equiaxed grains [4,10].

Another structure frequently observed in the WZ is a banded or "onion-ring" structure. The bands exhibit a periodic modulation of grain size, phase, crystallographic texture, and second-phase particle size and density, and are related to the speed at which the tool advances laterally per revolution [5,10,27]. In general, banding is found in butt-weld configuration, since the BM alloys butted side-by-side and are stirred together laterally. It is not so distinct in lap-weld configuration where the mixing of the alloys is more localized to the region near the interface. Lap FSWs yield distinct cross-sections in which the interface between the two alloys in the WZ is depressed relative to the interface in the TMAZ, HAZ, and BM, and the formation of "hooks" of the lower work piece material which is drawn up into the upper work piece material on either side of the WZ. These features are produced by the flow of the material down, outward, and up again in a cyclic motion around the pin, as shown in Figure 1. This pattern of material flow also causes some particles from the lower alloy to be stirred into the upper alloy, creating a composite-like structure.

The presence of discrete particles and the banding can both have significant effects on mechanical performance since cracks tend to propagate along particle surfaces and regions of high densities of particles, causing local delamination and reducing the fatigue resistance [5,7,10]. However, failure can also occur in other zones depending on the amount of heat input due to processing parameters and the annealing effects that take place because of it. Work piece thickness will determine the post-weld cooling rate, which can also influence strength [28]. Typically the weaker base metal component in a dissimilar weld will determine the joint

performance [29]. It is important to characterize and study the microstructures produced in these specific zones as well as the interfaces between them to determine and predict the overall performance of the weld.

Defects present at both the macrostructural and microstructural levels can have immense affects upon the mechanical performance as well. It was observed by da Silva et al. through the stop-action technique of leaving the weld tool in the material in order to observe the macroscopic flow of material around the tool, that gaps are created in the material around the threads of the tool pin [12]. Most of the time, these gaps close again once the tool has passed by, however the presence of hard particles can disrupt the material flow and cause the gaps to remain open, leaving large voids. Micro-cracks induced by post-weld cooling and porosity can also be present, although typically to a much lower degree than in fusion welds. The presence of zinc (Zn) from the use of galvanized steels can have varying effects. Jana et al. remarked that a Mg-Zn intermetallic layer would be beneficial to the bonding of Mg-steel dissimilar lap friction stir welds, since Mg and iron (Fe) are not soluble in either their solid or liquid states [25]. However, if the temperature during FSWing is high enough to cause the zinc to melt, it can cause regions of porosity to form [30]. In dissimilar alloy combinations in which solid solubility can be achieved, such as with aluminum-steel welds, it may be beneficial to use alloys which are not zinc-coated.

1.5 Formation of Intermetallic Compounds in Dissimilar-Alloy Welds

When welding dissimilar metals, one concern is the formation of intermetallic compounds (IMCs) at the weld interface and around particle inclusions within the WZ. In the case of FSW aluminum to steel, the structure often seen is one of steel particles dispersed

throughout the aluminum WZ matrix [22]. The IMCs tend to form around the edges of the steel particles where the highly plastic aluminum chemically reacts with the Fe. In some cases, needle- and petal-shaped IMC structures can be broken off and mixed into the weld by the stirring action [22]. The weld temperature, which is related to the tool rotation speed and the lateral welding speed, influences the amount of IMC growth that occurs through temperature-dependent diffusion; faster rotation speeds and slower transverse speeds produce higher temperatures. Increased temperatures will enhance the growth of IMCs [10,20].

In many butt-configuration FSWs, such as the studies done by Kimapong and Watanabe, and Watanabe et el. who used energy dispersive spectroscopy to identify AlFe and Al_3Fe IMC particles formed in the WZ of 5083 Al to 400 stainless steel, more IMC structures can be found near the top of the weld where the tool shoulder creates the most frictional heat [1,31]. In lap welds, IMC growth is dispersed relatively evenly across the interface between alloys and around the particles stirred into the weld zone matrix. The morphology of IMC particles can also vary based on temperature and position within the WZ. Jiang and Kovacevic used XRD to identify $Al_{13}Fe_4$ and Al_5Fe_2 IMC particles formed during the welding of 6061-T6 Al and 1018 steel. They found that the particles were smaller and more sphere-like in shape in the aluminum alloy, while being larger and more needle- and flower petal-shaped nearer to the steel [19]. In the case of galvanized steels, iron-zinc (Fe-Zn) intermetallics are formed in layers on the steel base metal surface which are of importance to the weld microstructure. The addition of zinc to the base metal can lead to the formation of complex Al-Fe-Zn ternary phases during FSW [32]. The Al_4Fe particles identified by Lee et al. in an FSW joint of 304 stainless steel and AA6056 were also rich in chromium, nickel and manganese [33]. Precipitation of second phase particles rich in Cu, Mg, manganese (Mn) and Fe have also been observed in similar-alloy FSW 2024-T3 Al

joints, demonstrating that the heat generated during the welding process can be sufficient to cause segregation within the same alloy [7,9,10]. However this can be controlled or avoided by decreasing the weld temperature.

While the heat input of FSW is considerably lower than that of fusion welding, it can reach sufficient temperatures to cause precipitation issues and accelerated ageing, especially in solution-aged alloys. The HAZ can be particularly susceptible because it experiences heating without any mechanical deformation [29]. Mechanical testing of these types of welds has shown that crack propagation and failure tends to occur along the interface between second phase particles and in the weld matrix especially where IMC layers are present, and it has been concluded that the degree of IMCs in the weld can have a significant influence on mechanical performance [1,20,31,34]. Tanaka et al. stated in their investigation of FSWed mild steel-AA7075-T6 joints that mechanical strength exponentially increased with decreasing IMC layer thickness, which varied with the welding parameters [20].

1.6 Crystallographic Textures of FSW

Due to the stirring action by the weld tool, simple shear is the typical mode of deformation observed in FSW microstructures. For this reason shear texture components are expected in the WZ and TMAZs of FSW samples [6,27,35,36]. Typically the morphology is such that the shear plane is tangential to the surface of the pin with the shear direction (SD) located within that plane, and the shear plane normal (SPN) is aligned with the radial outward direction of the pin surface [27,35,36]. The partial fiber textures shown in Figure 4 were taken from the book by Kocks et al. titled *Texture and Anisotropy: Preferred Orientations in Polycrystals and their Effect on Materials Properties*. The figure displays the partial A- and B-

fiber textures that characterize shear deformation in face-centered cubic (FCC) crystals. Shear in FCC crystals is defined by dislocation glide in the {111} <110> slip system. The A-fiber represents a {111} pole in the shear plane with the in-plane SD component distributed randomly throughout the plane. The B-fiber is given by shear planes randomly distributed about the <110> axis. In Miller index form, these fibers are represented as A: {111} <uvw> and B: {hkl} <110>. The C-fiber component also shown in Figure 4 represents specific components of the B-fiber [36,37]. The {111} PF displayed in Figure 5 shows an ideal shear texture in FCC crystals giving both the partial A- and B-fibers. This ideal shear texture was used by Young et al. to determine the expected ideal shear texture for FSW in HSLA 65 steel in which the weld had taken place in the high-temperature FCC austenite phase and transformed to the low-temperature body-centered cubic (BCC) ferrite and martensite phases upon cooling [6].

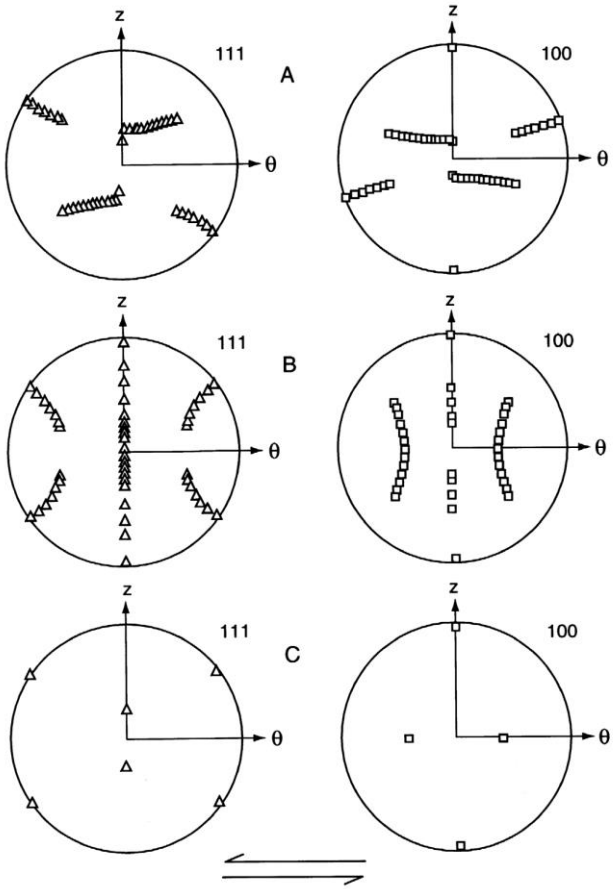

Figure 4 {111} and {100} PFs showing partial A-fiber, B-fiber, and C-fiber for simple shear texture in FCC crystals. θ corresponds to the SD while Z corresponds to SPN [37].

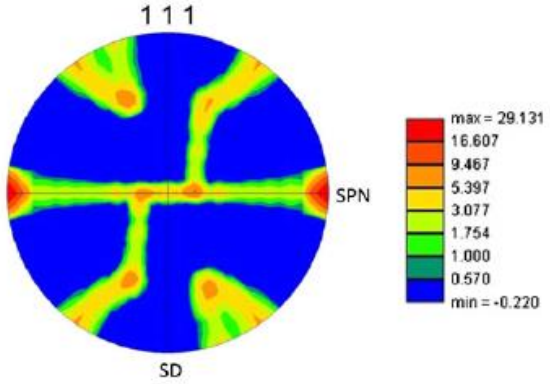

Figure 5 {111} PF showing ideal shear in FCC crystals [6].

Shear in BCC crystals is defined by dislocation glide in the {110} <111> slip system. Shear and torsion textures in BCC materials are less well studied than FCC materials however in many cases the {110} PF for BCC crystals is comparable to the {111} PF for FCC crystal for a given deformation texture. Figure 6 below shows experimental {200} and {110} shear textures for Aramco iron, as shown by Kocks [37]. The {110} PF shows a texture similar to the shear fibers shown in Figure 5, however in this case, the SD and SPN are rotated CW from the horizontal and vertical axes, respectively.

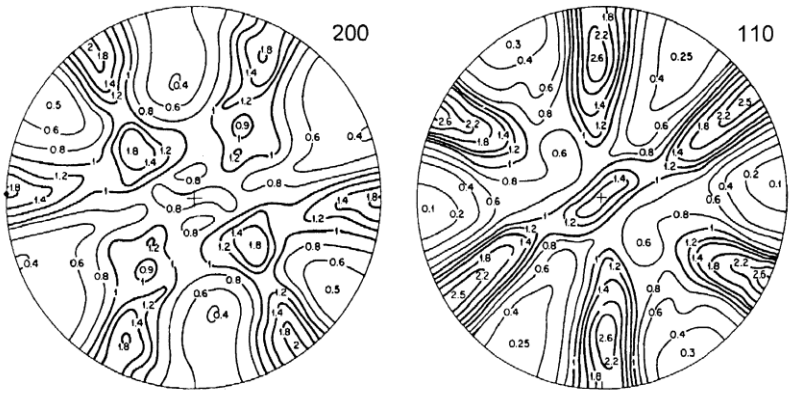

Figure 6 Experimental {200} and {110} PFs for Aramco iron sheared to γ = 2.1 [37].

In many cases of FSW, simple shear deformation is not the only factor influencing texture; the effect of the downward flow of material facilitated by the threads, continuous grain refinement and recrystallization mechanisms, time at-temperature, and subsequent cooling rates must be considered [38,39]. Fonda et al. [35] observed notable vertical displacement of grains around the weld tool. The solid-state phase transformation from FCC to BCC in FSWed steel specimens can induce marked deviations from the expected texture, as was observed by Young et al. and Gourdet et al. [6,40], however this did not occur in the steel alloys of the welds studied

here since a weld temperature high enough to induce a phase transformation would have been sufficient to melt the aluminum alloys.

Fonda et al. also discussed in their paper "Development of Grain Structure During Friction Stir Welding" that grain refinement occurs within a deformation field ahead of the weld tool and the formation of subgrains is dependent upon both the orientation stability of the pre-existing grains with respect to the applied deformation and on the progressive rotation of the subgrain lattice as the weld tool continues to deform the refined structure (continuous dynamic recrystallization (CDRX)) [35]. Rhodes et al. define the difference between regions of non-recrystallized regions of subgrains and regions of recrystallized grains based on the level of deformation evidenced by the grain orientation. By this definition, non-recrystallized subgrains will show similar crystallographic orientation indicating that they originated from a common parent grain via the formation of low angle boundaries (LABs) which eventually develop into high-angle boundaries (HABs) once a critical misorientation angle has been reached [24,40]. Recrystallized structures will have more random orientations [39]. However, in the case of FSWed microstructures, significant deformation can occur after recrystallization has taken place, giving rise to heavily deformed structures that may share similar orientations (CDRX) [40,41]. The character of the refined structure can also vary with the type of alloy undergoing refinement and with the temperature at which deformation takes place [42]. This makes it difficult to identify the specific mode of grain refinement that has taken place in the weld samples used for this study without further investgation. It has been observed in aluminum alloys that recrystallized rolling textures are quite different than the rolled textures prior to the recrystallization while recrystallized shear textures are quite similar to shear deformation textures [36].

1.7 Objective

The scope of this project was outlined by the United States Army Tank Automotive Research, Development, and Engineering Center (TARDEC) in order to develop and assess the quality of methods for weight reduction of armored combat vehicles. By developing a feasible method for joining steel armor plate sections to light-weight aluminum armor plates through FSW, significant weight reduction can be achieved without sacrificing ballistic protection.

Because of the importance of understanding the microstructure and mechanical performance of dissimilar FSWs between aluminum and steel, this study focuses on the characterization of the different zones of the FSW cross sections, how the zones differ from the base metal and from one another, and the identification of intermetallic compounds formed between the aluminum and steel alloys within the weld.

Chapter Two: Experimental Methods

2.1 AA6111-T4/DP Steel Weld

The preliminary weld sample was comprised of 2.2-mm thick 6111-T4 aluminum alloy sheet overlapping 1.5-mm thick dual phase (DP) galvannealed steel sheet. Hereafter, this weld will be referred to as AA6111-T4/DP steel. 6XXX series aluminum is alloyed with Mg and silicon (Si), and the T4 condition of the aluminum alloy refers to a solution heat treatment with natural ageing, but no cold working after heat treatment [43]. The precipitation strengthening particles are mainly Mg_2Si, however Mg_5Si_6 can occasionally be present in peak-aged states [44,45]. The precipitation strengthening particles and phases were not examined in this study. The galvannealing process involves hot-dip galvanization followed by annealing to increase diffusion of the zinc atoms into the steel. Specific compositions of these alloys were not available. The weld direction (WD) was parallel to the transverse direction (TD) of both sheets. The tool, seen in Figure 7, was made of H-13 tool steel. It had a convex scrolled shoulder and a threaded, tapered pin. A tungsten carbide (WC) scribe was attached to the tip of the pin. Schematics with tool dimensions are found in Appendix One: Tool Dimensions for AA6111-T4/DP Steel Weld. Rotation speed was set at 500 revolutions per minute (rpm) and the lateral weld speed was 100 mm/min. Plunge depth was limited such that the scribe could not reach the bottom of the steel plate. The weld was sectioned using a water-cooled diamond abrasive blade and mounted in thermosetting epoxy resin. Two cross-sectional samples were prepared: one for optical microscopy and Vickers micro-hardness indentation and one for scanning-electron microscopy, with the WD coming out of the cross-sectional plane being viewed. The clockwise

rotation of the weld placed the retreating side (RS) of the tool on the left side of the cross section and the advancing side (AS) on the right.

Figure 7 Photograph of FSW tool used for the AA6111-T4/DP steel weld.

2.1 AA6061-T6/Wrought Steel Weld

This weld consisted of applique 6061-T6 aluminum alloy armor plate and wrought homogeneous steel armor plate for use in combat vehicles and ammunition testing. Hereafter, this weld will be referred to as AA6061-T6/wrought steel. Compositions for these alloys are given in Table 1 and Table 2 respectively. Precipitation strengthening phases for the 6061 aluminum are the same as for the 6111 aluminum discussed above [44,45]. The nominal dimensions were 25.4 mm (1 inch) by 101.6 mm (4 in) for the AA6061 plate and 12.7 mm (0.5 in) by 101.6 mm (4 in) for the wrought steel plate. The WD was parallel to the rolling direction (RD) of the aluminum plate and the TD of the steel plate. The AA6061 plate was overlapped on top of the steel plate, making the total cross-section 38.1 mm x 101.6 mm (1.5 in x 4 in). A

cross-sectional sample was obtained via band saw which was then sectioned again into smaller regions to simplify the mechanical polishing technique. Figure 8 shows a schematic of how the regions are divided. Two cross-sectional samples were also prepared from this weld: one for optical microscopy and Vickers micro-hardness indentation and one for electron microscopy.

Table 1 Chemical composition of 6061 aluminum alloy [46]

Element	Weight Percent in 6061 Aluminum Alloy
Silicon	0.40 – 0.80
Iron	0.70
Copper	0.15 – 0.40
Manganese	0.15
Magnesium	0.8 – 1.2
Chromium	0.04 – 0.35
Zinc	0.25
Titanium	0.15
Other, maximum each	0.05
Other, maximum total	0.15
Aluminum	Balance

Table 2 Chemical composition of wrought steel alloy [47]

Element	Max. Limit for Declared Chemistry of Wrought Steel, Weight Percent	Allowable Variation, Weight Percent
Carbon	0.30	±0.05
Manganese	Not Required	±0.20
Phosphorous	0.020	-
Sulfur	0.010	-
Silicon	Not Required	±0.20
Chromium	Not Required	±0.25
Molybdenum	Not Required	±0.25
Vanadium	Not Required	±0.075
Niobium	Not Required	±0.05
Copper	0.25	-
Nitrogen	0.03	-
Titanium	0.10	-

Zirconium	0.10	-
Aluminum	0.10	-
Lead	0.10	-
Tin	0.02	-
Antimony	0.02	-
Arsenic	0.02	-

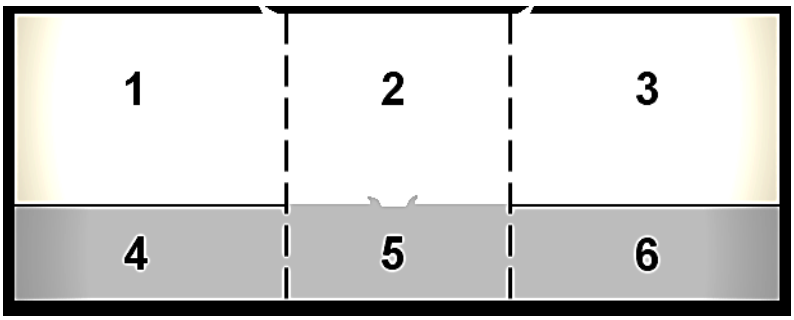

Figure 8 Schematic of sectioned regions of AA6061-T6/wrought steel weld specimen.

The tool rotation speed was set at 300 rpm and the lateral weld speed was 50 mm/min. This tool was also made from H-13 tool steel. The concave scrolled shoulder had a diameter of 43.1 mm (1.70 in). The pin had a height of 25.4 mm (1 in.), a taper angle of 6.1°, and a diameter of 22.2 mm (0.874 in) at the base and 16.8 mm (0.661 in) at the tip. The WC scribe diameter was 3.175 mm (0.125 in.), a height of 1.588 mm (0.0625 in.) off the tip of the pin, and was set at a diameter of 9.53 mm (0.375 in.). Schematics of the tool and the pin are found in Appendix Two: Tool Dimensions for AA6061-T6/Wrought Steel Weld and a photograph of the tool is shown in Figure 9.

Figure 9 Photograph of weld tool used for the AA6061-T6/wrought steel weld.

2.3 Polishing

All cross-sectional specimens were mechanically ground using silicon carbide abrasive disks of 120, 240, 320, 400, 600 and 1200 grit. The fine polishing steps were of particular importance to this study because of the sensitivity of the aluminum to the presence of foreign particles that can cause damage to the specimen surface. Typical challenges when mechanically polishing dissimilar-alloy specimens include embedding of hard particles in the softer alloy, formation of artifacts known as the "comet tail" effect in which hard particles leave deep wakes scratched into the surface behind them, and a significant amount of relief at the interfaces between the harder and softer alloys. Comet tails are caused by inclusions and embedded particles pulling out and leaving scratches behind them during polishing. The effect is magnified by maintaining uni-directionality during polishing [48]. To prevent this, the sample should be rotated around the polishing wheel in the opposite direction of the wheel rotation. Unfortunately, in this case it was necessary to maintain uni-directionality by holding the sample in one

orientation with the aluminum ahead of the steel, otherwise steel particles would be dragged across the aluminum in high concentration, causing scratches too deep to remove with subsequent polishing steps. Maintaining uni-directionality helped to minimize this result however the very presence of steel in the specimen meant that the embedding of small steel particles in the aluminum surface, and thus the presence of some comet tails, were unavoidable.

To prevent formation of relief between the aluminum and steel at the alloy interface and to maintain flatness, it was important to use low/no-nap polishing cloths. Initially, 8-inch nylon cloths were used for the 3-μm, 1-μm, and 0.25-μm steps, however, nylon was found to hold onto the metal particles and cause significant embedding in the aluminum even with a new, previously unused cloth. The 1-μm step proved the most problematic, producing deep scratches that were difficult to remove with the 0.25-μm step and worsened the embedding problems in the aluminum. Consequently, acetasilk was chosen instead because it produced better surface quality and the 1-μm step was removed from the procedure. TexMet C polishing cloth was chosen both for the 0.25-μm diamond step and for vibratory polishing with colloidal silica because it has relatively no nap. This was especially important since the colloidal silica suspension contains a chemical agent that can augment rounding and etching of relief edges. The lack of nap on the cloth helped to counteract the rounding effect.

Polishing was conducted as follows:

- 3 μm diamond paste on 8-inch diameter acetasilk low-nap cloth from South Bay Technology, approximately 2-5 minutes
- 0.25 μm diamond paste and suspension on 12-inch diameter TexMet C low/no-nap cloth from Buehler, until all 3-μm scratch lines are removed

  - AA6111-T4/DP steel samples were mounted in an automatic polisher head and polished at 500 rpm, approximately 30-60 minutes
  - AA6061-T6/wrought steel samples were polished by hand at 350 rpm, approximately 10-20 minutes
- 0.05 μm colloidal silica suspension on 12-inch diameter TexMet C low/no-nap cloth from Buehler on a Buehler Vibromet-2 vibratory polisher, 30 minutes at a time until EBSD patterns were clear
- Diamond polishing was lubricated with BlueLube alcohol/oil-based lubricant from MetLab Corp, and samples were washed ultrasonically with anhydrous alcohol between each polishing step.

2.4 Methods of analysis

2.4.1 Optical Microscopy and Scanning Electron Microscopy

Cross sectional specimens from both welds were chemically etched with a two percent nitol solution to reveal the steel grains in optical microscopy (OM), which was performed with a Leica DM 750M equipped with a digital camera and Leica Application Suite digital imaging software. Optical micrographs were taken of the microstructure under polarized light. All scanning electron microscopy (SEM) was performed in an FEI XL30 Sirion 200 field emission scanning electron microscope (FE-SEM) at 20 KeV accelerating voltage.

Optical and SEM micrographs were taken of the weld cross sections near the interfaces at various magnifications to identify and qualitatively assess the level of IMCs, voids, porosity, or micro-cracks present in the welds. SEM micrographs of the weld cross sections were also obtained at 500x magnification for the AA6111-T4/DP steel sample and at 100x magnification

for the AA6061-T6/wrought steel sample to measure the volume fractions of steel particles within the aluminum WZs. ImageJ software was used to perform this measurement, utilizing a stereological point-count method by overlaying a square grid on the micrographs. By the principle of DeLesse, the point-per-point (P_P) measurement is equivalent to the volume fraction (V_{Fe}) [49].

2.4.2 Energy Dispersive Spectroscopy

Energy dispersive spectroscopy (EDS), or energy dispersive x-ray spectroscopy (EDXS), is a method by which chemical identification and mapping can be performed in an SEM. When the incident electron beam has sufficient energy, the primary electrons will knock inner shell electrons from the sample atoms, leaving electron vacancies and the atom in an increased energy state. To relax the atom, an electron falls from one of the higher energy states to fill that vacancy, and energy is released in the form of an x-ray characteristic to the atom and energy state from which it came, thus allowing the elements present to be identified [50].

To analyze the x-rays, they must be harvested via a silicon semiconductor detector. When the x-rays contact the detector, they excite electrons into the silicon's conduction band, creating the same number of positively charged holes. The energy of the detected x-ray is proportional to the number of electron-hole pairs created [50]. The outer surface of the detector is protected by a thin window, which, in the case of the detector on the scanning electron microscope used in this experiment, was made from an ultrathin polymer film. The thinness of this window allows low energy x-rays to be detected, down to those from the inner shells of boron. However, if a traditional beryllium window is used, a large portion of the low-energy x-rays are absorbed in the window, so the energy of x-rays that are able to pass through the

window is limited to about 1 KeV, eliminating detection of all elements lighter than sodium. Upon detection, an energy spectrum, measured in KeV, is recorded and plotted as intensity versus energy.

Two common problems with analyzing the data are the presence of "sum peaks" and "escape peaks." Sum peaks occur when two x-rays are read by the detector at the same time, thus resulting in an intensity peak at exactly twice the energy value of what it should be. An escape peak results from an x-ray being emitted from the detector itself, and will consistently appear as an intensity peak at 1.74 keV. This can occur when there is either a high amount of dead time or a large number of counts per second for the x-ray detection.

For this study, EDS was performed in the same FE-SEM as mentioned above, at an accelerating voltage of 20 KeV, spot size 5, and working distance of 4-5 mm at various magnifications using EDAX Genesis software. These settings were chosen to maintain 10,000-80,000 counts per second (CPS) and down time of approximately 30%. Both chemical mapping and point analyses were performed to identify the IMCs present.

2.4.3 Electron Backscatter Diffraction

Electron backscatter diffraction (EBSD) is performed in an SEM using relatively high accelerating voltages and spot sizes. Typical values are 20-25 KeV accelerating voltage and a spot size of 5 or 6. Larger spot sizes can decrease the spatial resolution however it also increases the beam current. A high amount of signal is necessary for performing EBSD, and it also helps to smooth the secondary electron (SE) image which is useful for obtaining a good focus [51]. EBSD uses Bragg diffraction and electron channeling to obtain crystallographic information from the Kikuchi diffraction patterns of a given structure [50]. When the incident beam of the

SEM hits the sample, the electrons are scattered in a cone, the entirety of which satisfies the correct angle from the beam for Bragg diffraction. The sample must be tilted to an angle of approximately 70° so that the diffracted cones can be directed toward a phosphor screen. Where the electrons cause the phosphor screen to fluoresce and are turned into photons, the Kikuchi diffraction patterns become visible, as in Figure 10 (A). A charge coupled device (CCD) camera located behind the phosphor screen records images of the bands that appear on the screen [50,52]. The incident electron beam is scanned across a designated region of the sample, collecting diffraction patterns for each point within the scan. By compiling the data from individual points over the entire scanned region, crystallographic data such as phase, orientation, texture, grain boundary character, etc., can be measured for large sample areas.

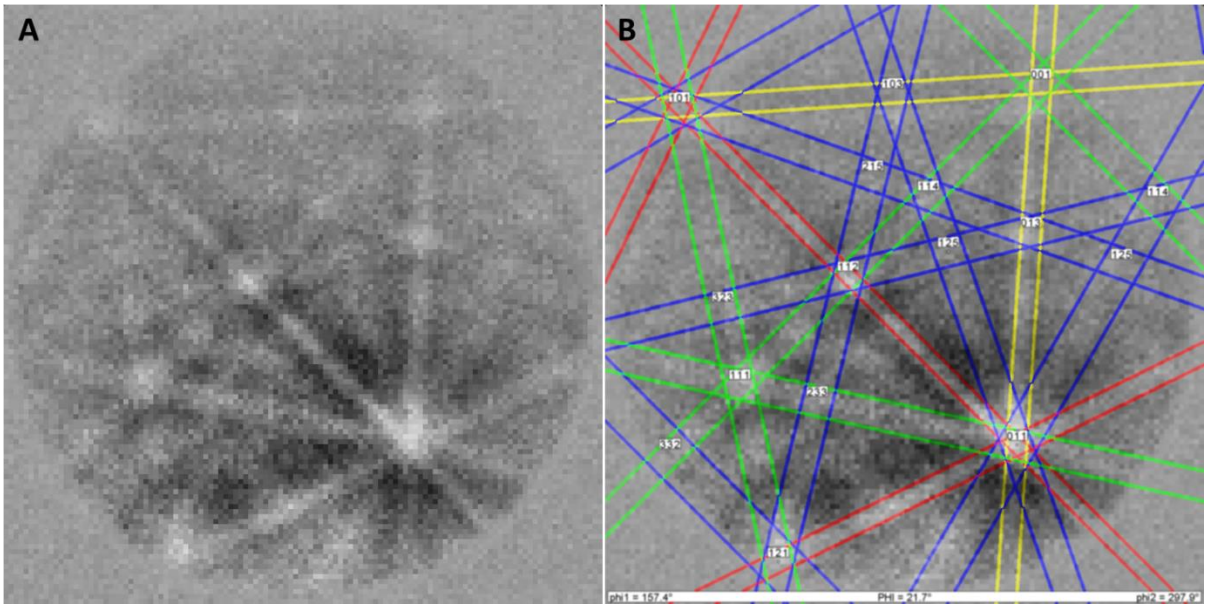

Figure 10 (A) Kikuchi diffraction pattern on phosphor screen, (B) index pattern overlay.

To identify phases present in the sample based on the crystallographic structure, the software indexes the diffraction pattern by running calculations that determine the confidence index (CI), which is based on the number of "votes" for each possible solution. Three Kikuchi bands detected from the crystal gives one or more votes towards deciding the correct solution. The equation used to calculate CI is given by:

$$CI = \frac{(V_1 - V_2)}{V_{Ideal}} \quad (1)$$

where V_1 is the number of votes for the first solution, V_2 is the number of votes for the second solution, and V_{Ideal} is the maximum number of votes possible for a given crystal structure. For cubic structures, seven Kikuchi bands are typically selected for detection, giving 35 maximum possible votes. The three conditions necessary for obtaining a correct solution are:

1. The specimen-beam interaction position (working distance) must be properly identified
2. The crystal structure must be known
3. The Kikuchi bands must be properly indexed

A CI value greater than 0.1 gives 95% accuracy in obtaining the correct orientation measurement for the patterns.

In the case of this experiment, the weld samples were analyzed using an accelerating voltage of 20 KeV and spot size 6, which corresponds to a beam current of ~10 nA [6]. OIM Analysis 6.1 was used to measure orientation, texture, and grain size (area) for the different zones of the weld cross sections. The OIM software uses generalized spherical harmonic

expansion in a Fourier series to measure orientation in S^3 space, and texture by way of pole figures (PFs) in S^2 space. The functions governing these calculations are as follows [53]:

- Orientation (body harmonic):

$$f(g) = k \sum_{l=0}^{\infty} \sum_{m=-l}^{l} \sum_{n=-l}^{l} C_l^{mn} T_l^{mn}(g),\ g = g(\varphi_1, \Phi, \varphi_2) \quad (2)$$

where $\varphi_1, \Phi, and\ \varphi_2$ are Euler angles: $0 \leq \varphi_1 < 2\pi,\ 0 \leq \Phi < \pi,\ 0 \leq \varphi_2 < 2\pi$

- Texture (surface harmonic):

$$P_{hkl}(\alpha, \beta) = k \sum_{r=0}^{\infty} \sum_{s=-r}^{r} C_{rs} K_{rs}(\alpha, \beta) \quad (3)$$

T_l^{mn} and K_{rs} are the body and surface spherical harmonic functions, respectively. C_l^{mn} and C_{rs} are series expansion coefficients [53]. All EBSD scans of the cross sections were done with the reference direction parallel to the WD, however the data was rotated prior to analysis such that the reference direction was aligned with the normal direction (ND) of the weld sample. This enabled the textures to be examined in terms of the SD and SPN in relation to the tangent and radial outward directions of the weld tool.

2.4.4 Micro-Hardness Indentation

A material's resistance to localized plastic deformation is characterized by hardness. There are several different scales of hardness measurement, including the Rockwell, Brinell, Knoop, Vickers and Mohs scales. The Mohs scale was developed as an early way to quantify hardness based on one material's ability to scratch another. This scale ranged from talc being the softest at level one, to diamond being the hardest at level 10. More modern measurements involve pressing indenter tips of specific sizes and shapes into the material with controlled loads and loading rates. The hardness number is then based on the size of the indentation left in the material when the indenter tip is removed. However, because each scale uses a different indenter

tip at varying loads, the hardness numbers are somewhat arbitrary and it is difficult to compare one scale to another [54,55].

The Vickers scale has been formerly called the diamond pyramid hardness test due to the fact that the indenter used is a square pyramid shape. The hardness number is given by the equation

$$VHN = \frac{1.854P}{L^2} \quad (4)$$

where P is the load applied and L is the measured length of the diagonal on the indentation left in the material. Loads can range from 500 g up to 120 Kg. The Vickers scale is referred to as micro-indentation because of the size of the indenter [54,55]. A Leco Vickers micro-hardness indenter was used in this study to build hardness profiles at 0.5-mm intervals across the weld cross sections using a 500 g load and a hold time of 10 seconds. By doing so, and correlating the data to the difference zones of the weld observed with EBSD, microstructural characteristics can be linked to mechanical performance.

Chapter Three: Characterization of AA6111-T4/DP Steel Welds

3.1 Physical Features of the Microstructure

3.1.1 Qualitative Assessment of Weld Microstructure

The cross-sectional sample etched with nitol solution for optical microscopy, found in Figure 11, revealed the presence of very large steel particles within the aluminum WZ matrix near the interface, surrounded by several large voids and a highly turbulent structure. The voids may have been the result of a disruption in the plastic flow of the aluminum caused by the presence of the large particles. Also, when a threaded pin is used, gaps can form in the material around the threads [12]. Most of the time these gaps close up again as the tool passes, but a disruption in the flow of the material may have prevented them from doing so, leaving voids. Several smaller steel particles were also scattered unevenly throughout the WZ, especially near the interface. Many of the large particles had distinct layers of intermetallic compounds formed between them and the aluminum, as seen in Figure 12. There were also turbulent gaps filled with what appeared to be IMCs and voids that began near the tips of the hooks, and followed the interface between the aluminum and steel alloys from the TMAZs outward to the BM, shown in Figure 13.

Figure 11 Composite of optical micrographs at 10x magnification revealing AA6111-T4/DP steel weld microstructure.

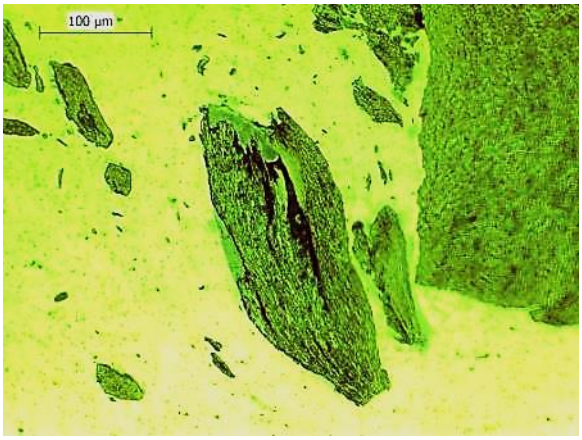

Figure 12 Optical micrograph at 50x magnification showing medium-sized steel particle and surrounding IMC layer.

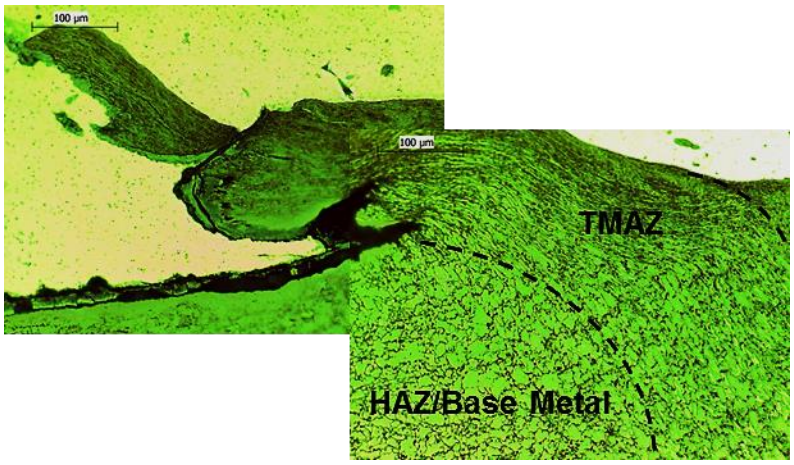

Figure 13 Composite of optical micrographs at 50x magnification showing turbulent interfacial layer outside the WZ.

This interfacial layer outside the WZ may have been the result of zinc-rich layers due to the galvanizing process and other oxides and impurities present on the surfaces of the work pieces prior to welding. SEM micrographs, like those in Figure 14 and Figure 15, revealed several porous, bubbly regions within the WZ that gave evidence to the flow of the material. These porous regions were particularly distinct in the regions where the volume fraction of steel particles was highest. It is suspected that Zn-rich layers on the steel melted during welding, and the Zn from the IMCs went into solid solution upon cooling, leaving pores where IMC particles had been.

Figure 14 Composite of SEM micrographs at 100x magnification, showing weld cross section and turbulent WZ structures.

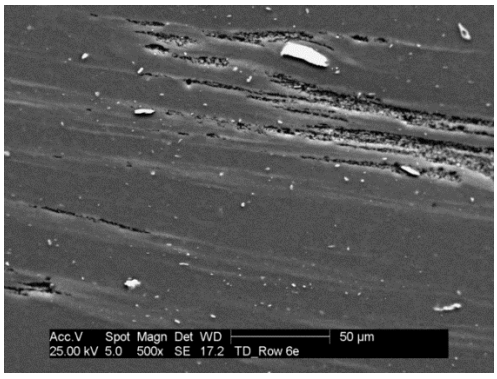

Figure 15 SEM micrograph of porous regions left by melted zinc.

3.1.2 Steel Particle Volume Fraction and Grain Size

The volume fraction of steel particles (V_{Fe}) in the aluminum WZ matrix was quantified by point counts. The results of these measurements are shown in Figure 16. V_{Fe} was much higher on the RS, low in the WZ near the interface. As the weld tool rotated, it pulled material from the AS across the center line and extruded it behind the tool as it moved ahead, leaving the steel particles in the WZ matrix. However, at a depth mid-way between the top of the weld and the interface, V_{Fe} was much lower on the RS and spiked slightly on the AS near the hook where a few large steel particles were present. The presence of these particles at mid-depth likely are related to the pattern of material flow discussed in Section 1.4 Microstructure and Mechanical Performance.

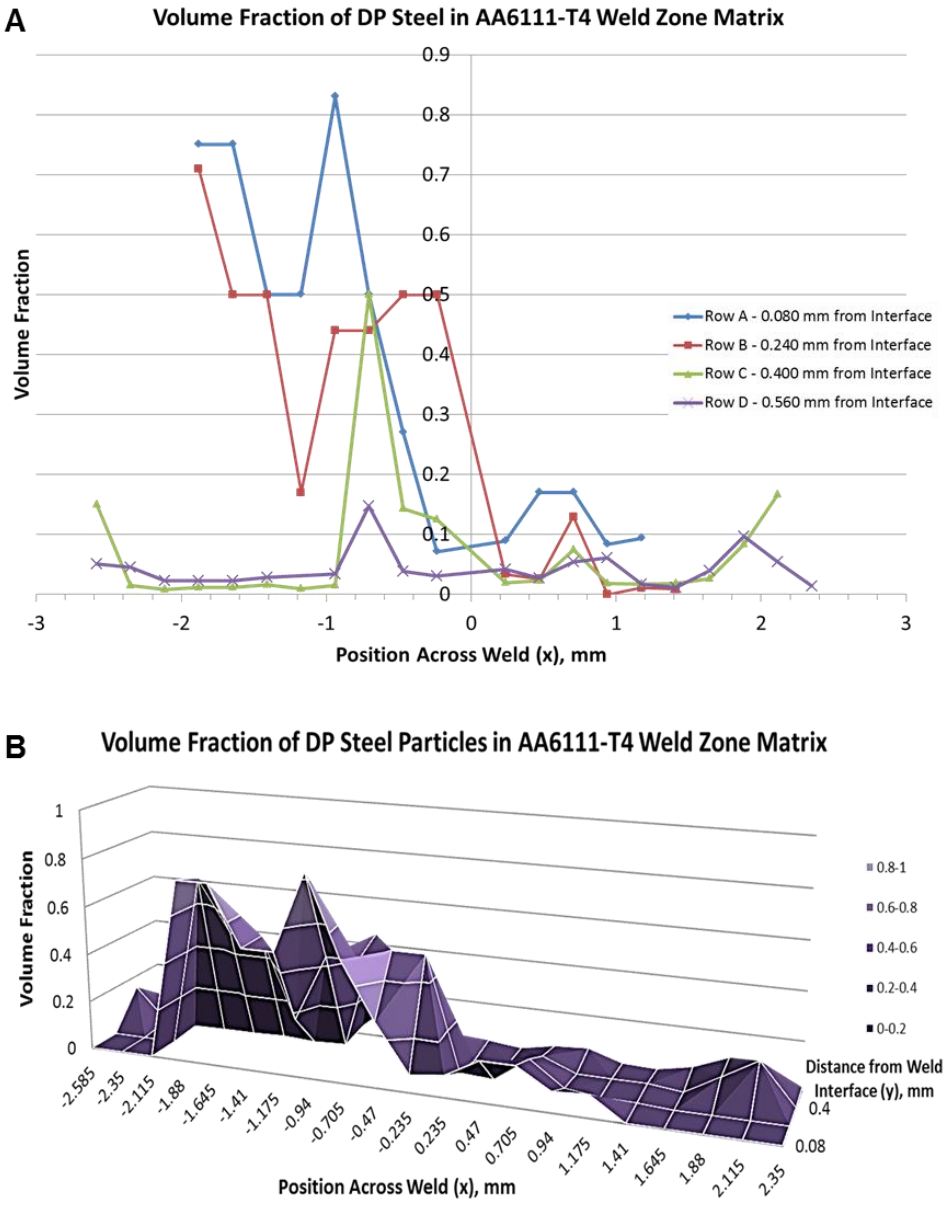

Figure 16 Volume fraction of steel particles in AA6111-T4 WZ matrix across the weld as (A) scatter plot and (B) 3D surface plot.

While grain size can also be calculated from a stereological lineal intercept measurement, in this case the grain size (area) was measured from EBSD data for the sake of simplicity. The BM grain size for the AA6111-T4 was approximately 670 μm^2. The TMAZ grain size was

between 300 and 500 μm^2 in the region of grains that showed significant lattice deformation but no elongation in shape; the grain size in the region of elongated grains decreased dramatically to 10-30 μm^2. The AA6111 WZ showed two different grain size ranges: the region between the hooks stirred by the scribe and pin tip, and the region at mid-depth above the level of the hooks where only the outside surface of the pin caused deformation. Grain sizes for these two regions were 2-4 μm^2 and 6-8 μm^2, respectively, indicating that the mid-depth grains may have experienced less-severe deformation in the absence of the scribe, and being closer to the tool's shoulder, may have experience greater heat input, causing the grains to grow slightly. The significant grain refinement in the WZ indicates recrystallization. The DP steel WZ was not measured, however the grain size decreased from 24 μm^2 in the BM to 7-10 μm^2 in the TMAZ. These measurements are summarized in Figure 17 and Figure 18.

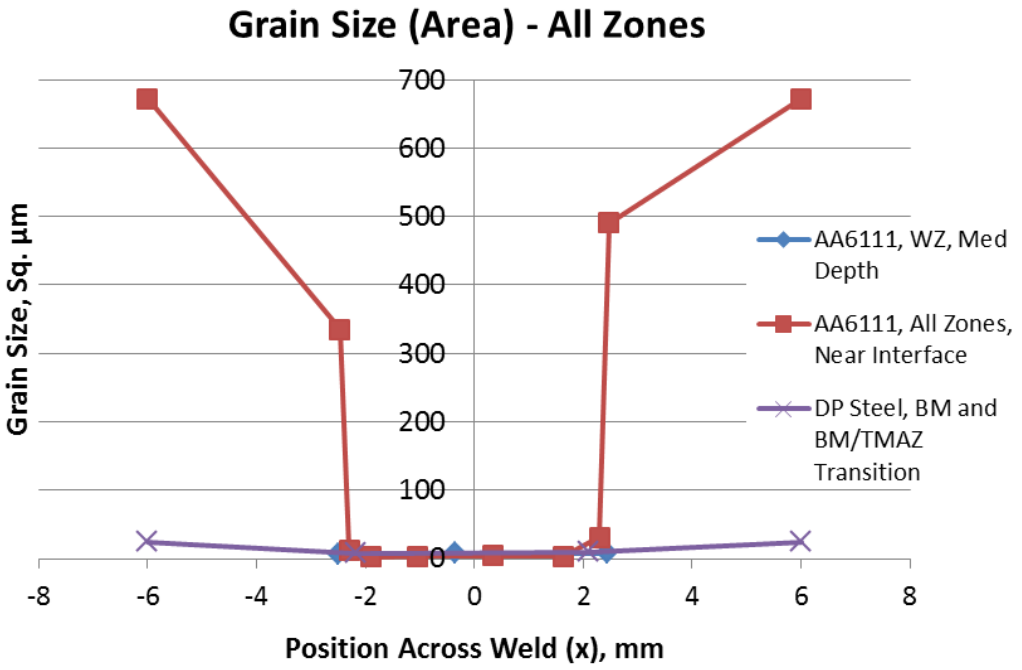

Figure 17 Grain size across weld cross section for all zones of AA6111-T4 and DP steel.

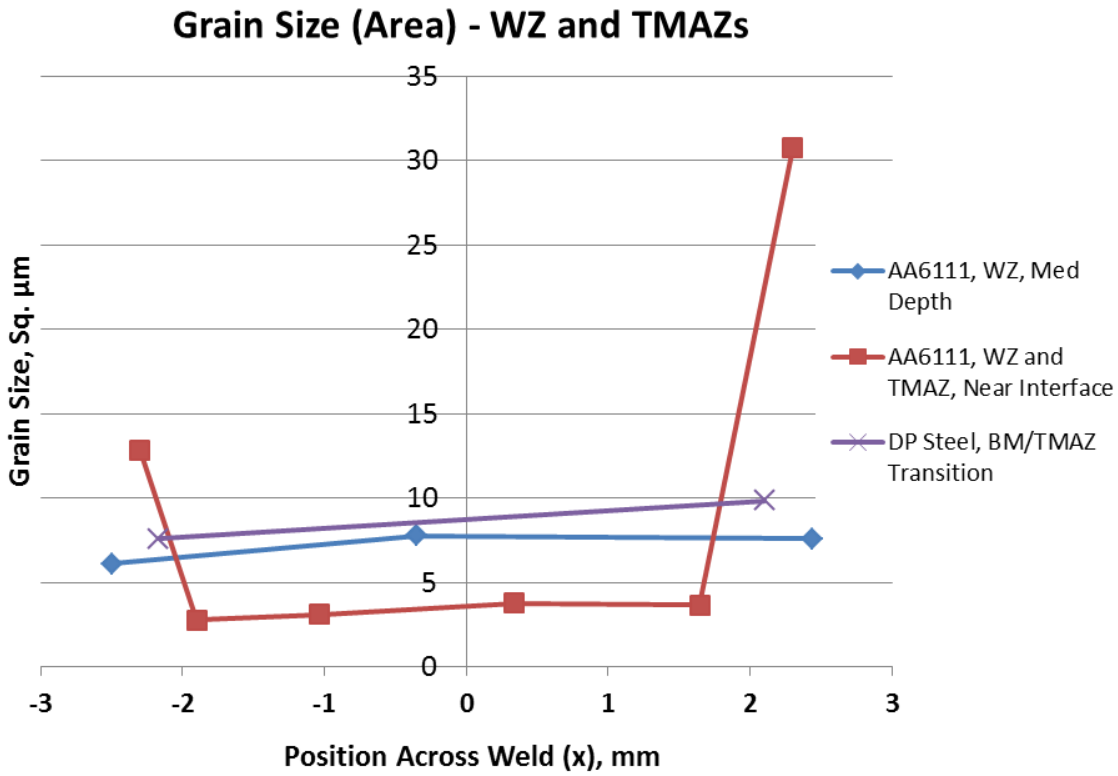

Figure 18 Grain size across weld cross section for WZ and TMAZs in AA6111-T4 and DP steel.

3.2 Micro-Hardness

Micro-hardness profiles were taken at 0.5-mm intervals across the weld cross section at 0.5 mm and 1 mm above the weld interface in the AA6111 and 0.25 mm and 0.5 mm below the weld interface in the DP steel. The AA6111 profiles are shown in Figure 19 and the DP steel profiles are shown in Figure 20. The WZ region between the hooks extends to ±2.5 mm from center on either side. Hardness in the aluminum decreased in the HAZs and TMAZs relative to the BM, while the hardness in the WZ increased to approximately the same level as the BM. The softening was attributed to the over-aging and solutionizing of the precipitation hardening particles. The subsequent increase in hardness in the WZ could either have been due to grain

refinement or re-precipitation of strengthening particles, or a combination of both. Further investigation would be needed to verify this. Peaks above 55 VHN corresponded to the presence of steel particles stirred into the WZ. The DP steel WZ had the highest hardness of the weld cross section, but stayed relatively constant in the TMAZs, HAZs and BM. The WZ hardness increased closer to the weld interface where the degree of deformation was more severe and the grain size was finer.

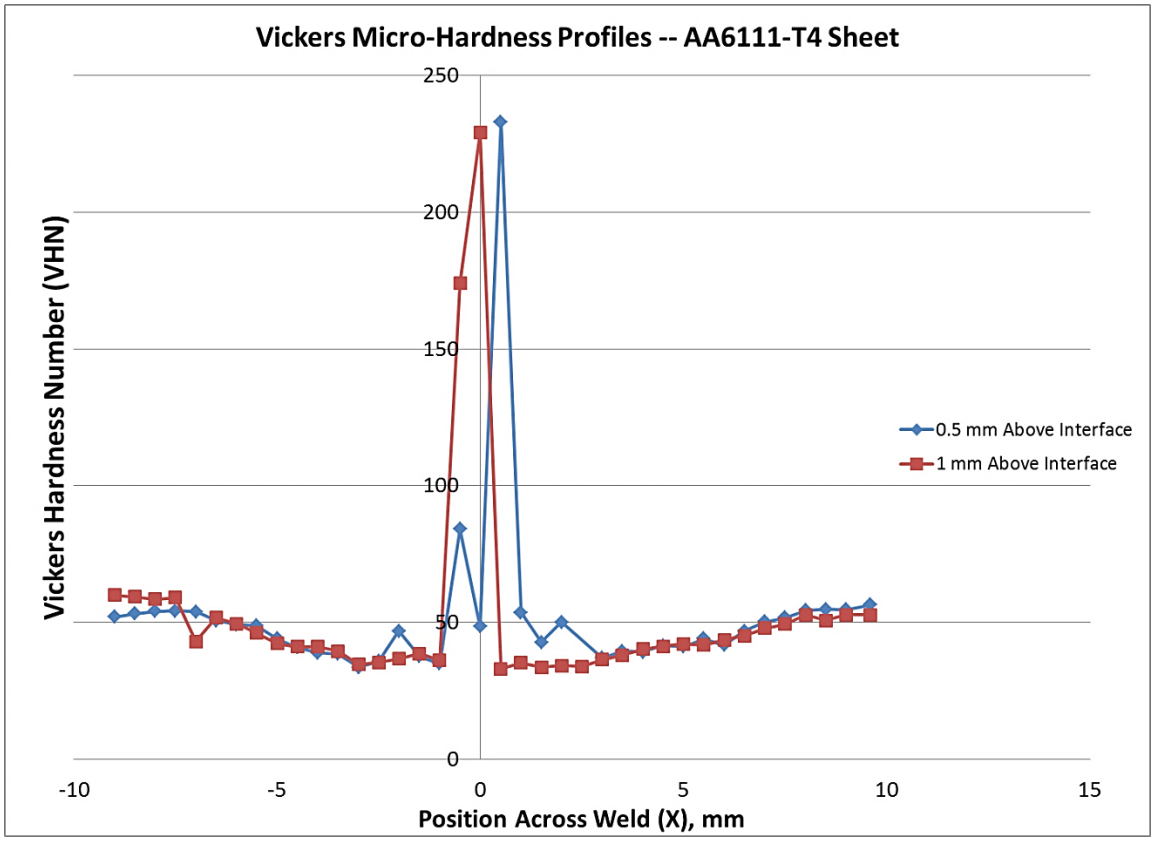

Figure 19 Vickers micro-hardness profiles for AA6111-T4 taken at 0.5-mm increments across the weld. WZ hardness is comparable to BM, while peaks correspond to presence of steel particles.

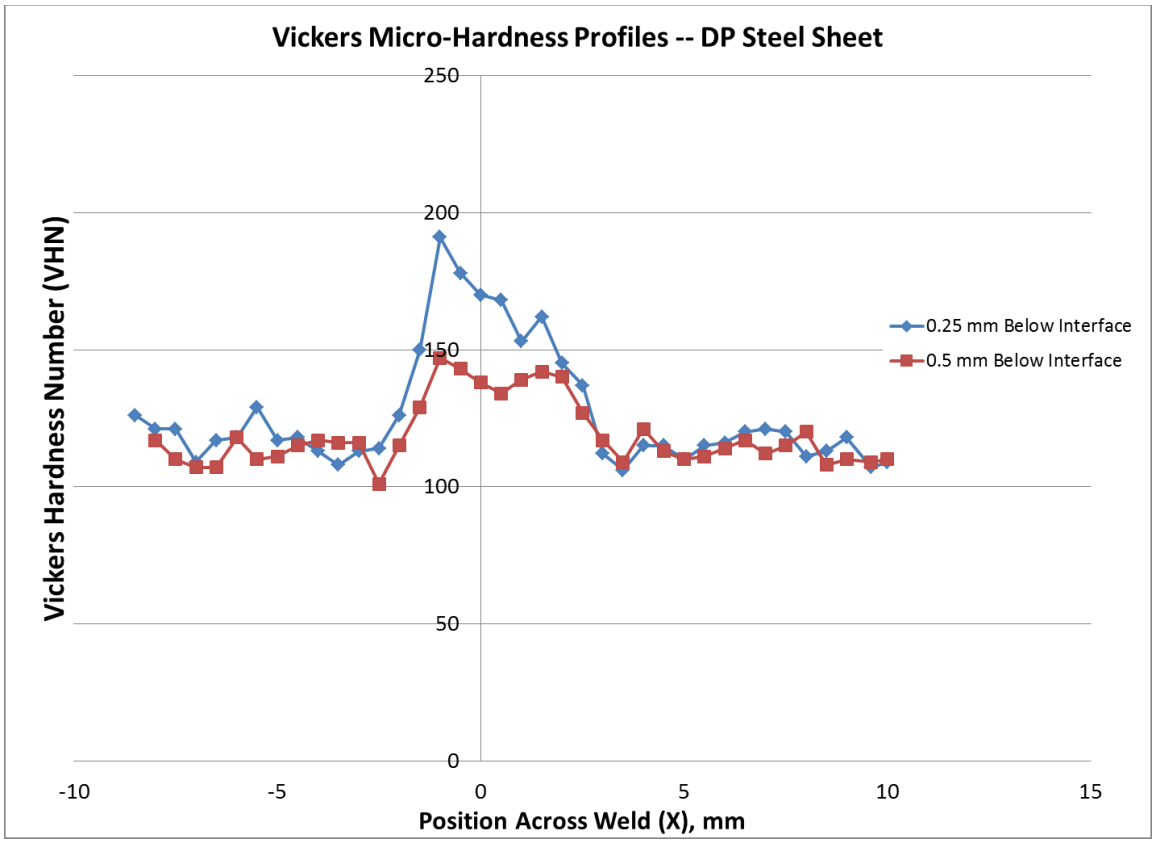

Figure 20 Vickers micro-hardness profiles of DP steel taken at 0.5-mm increments across weld. WZ shows highest hardness.

3.3 Chemical Analysis and Intermetallic Compound Identification

Because the DP steel used here was galvannealed, Zn-containing IMCs were present in the weld microstructure. Most hot-dip galvanizing takes place at 450°C, allowing consecutive layers of Fe-Zn IMCs to form on the surface of the steel. Based on the binary Fe-Zn phase diagram in Figure 21 and literature sources, these layers are comprised of:

- α-Fe = Fe-rich solid solution, BCC
- Γ = 18-31% Fe – Fe_3Zn_{10}, BCC
- Γ_1 = 19-24% Fe – Fe_5Zn_{21}, FCC

- δ_0 = 10-15% Fe – $FeZn_7$, hexagonal
- δ_1 = 7-13% Fe – $FeZn_{10}$, hexagonal
- ζ = 6-7% Fe – $FeZn_{13}$, monoclinic
- η = Zn-rich solid solution, ~0.04% Fe, hexagonal close-packed (HCP)

As the layers grow outward from the steel substrate, the Zn composition increases and the crystal structure changes [56-58].

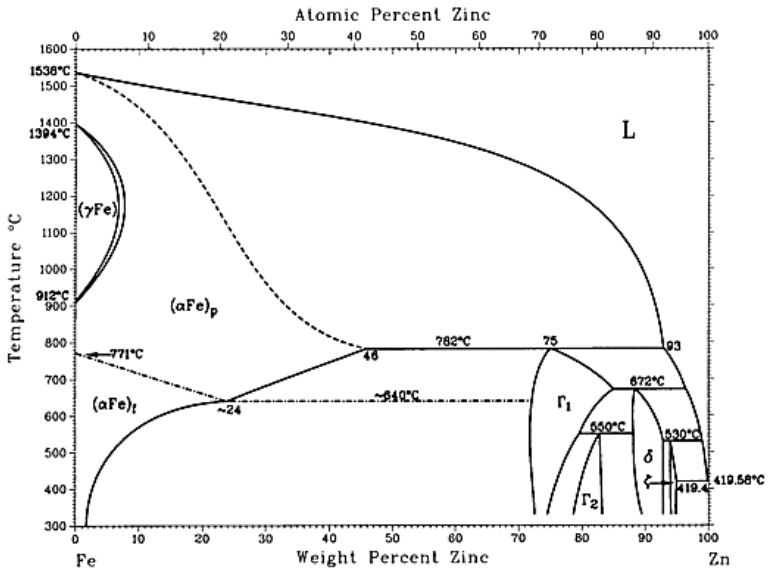

Figure 21 Iron-zinc binary phase diagram [59].

There are also several Al-Fe binary IMCs that can possibly form. Although weld temperature was not measured, it was assumed that the weld temperature was approximately 500°C, since there was evidence of zinc melting which takes place at ~420°C, but not of any aluminum melting which takes place at ~660°C. Based on that assumption and several studies in literature [1,19,22,31], as well as the binary phase diagram given in Figure 22, the Al-Fe IMCs that could be possibly have formed in the FSW are:

- AlFe – BCC
- $AlFe_3$ – FCC
- Al_2Fe – triclinic
- Al_3Fe – monoclinic
- Al_5Fe_2 – orthorhombic
- $Al_{13}Fe_4$ – trigonal

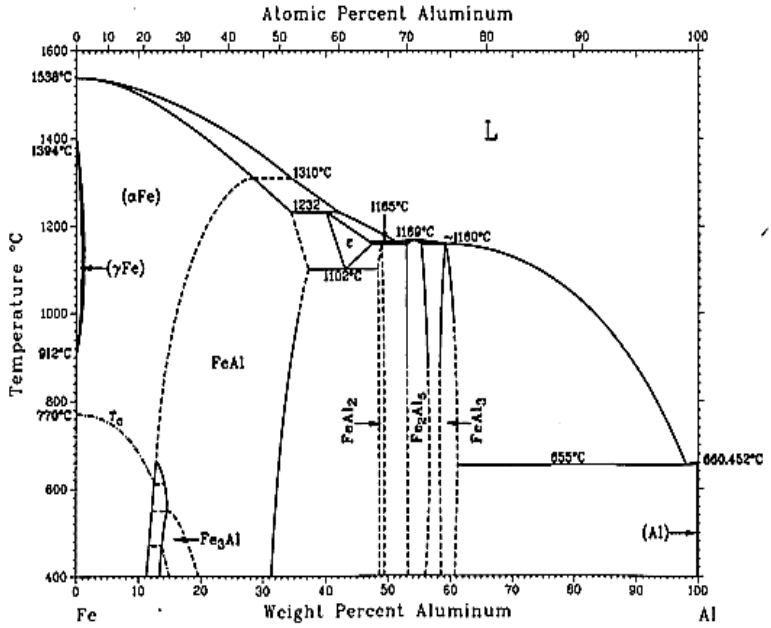

Figure 22 Al-Fe binary phase diagram [59].

Chemical mapping using EDS revealed Al-Fe, Al-Zn, and Al-Fe-Zn combinations present in various locations throughout the weld. Specific IMC phases were not identified in this weld sample. The regions that were analyzed as Al-Zn were most likely Al-rich solid solutions, based on the Al-Zn phase diagram in Figure 23 (A). There was a layer of ternary Al-Fe-Zn IMC at the aluminum-steel interface on the outside edges of the hooks, as shown by the chemical mapping

of the AS hook in Figure 24. The thickness of this layer was measured at approximately 10 μm. Although there was some zinc still present on the inside of the hook in the WZ, it appeared to exist in solid solution, as there was no distinct IMC layer visible in the SEM micrographs. Figure 25 shows compositions for point chemical analyses done on the IMC layers around the AS hook tip and a steel particle within the WZ.

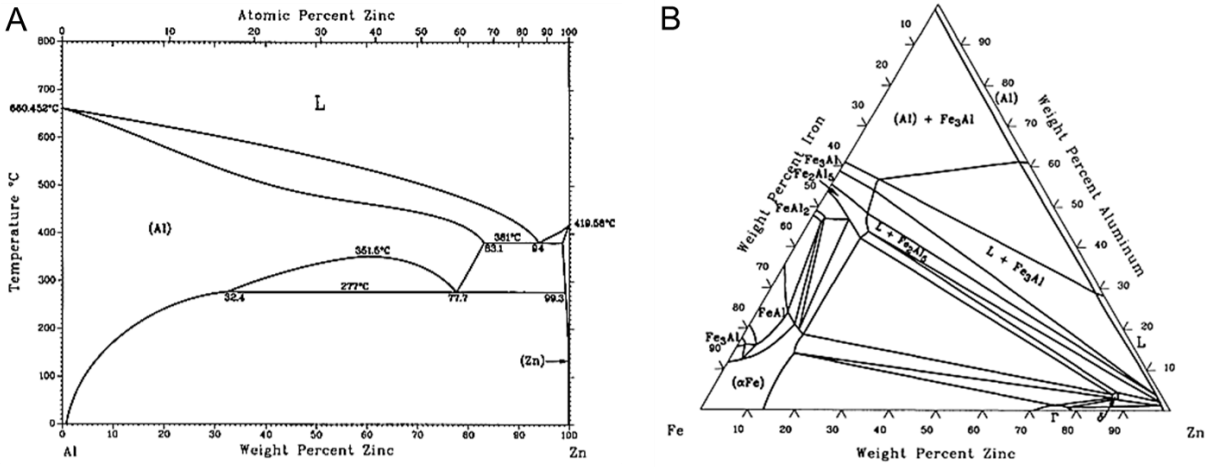

Figure 23 (A) Al-Zn binary phase diagram, (B) Al-Fe-Zn ternary phase diagram at 500°C isotherm [59].

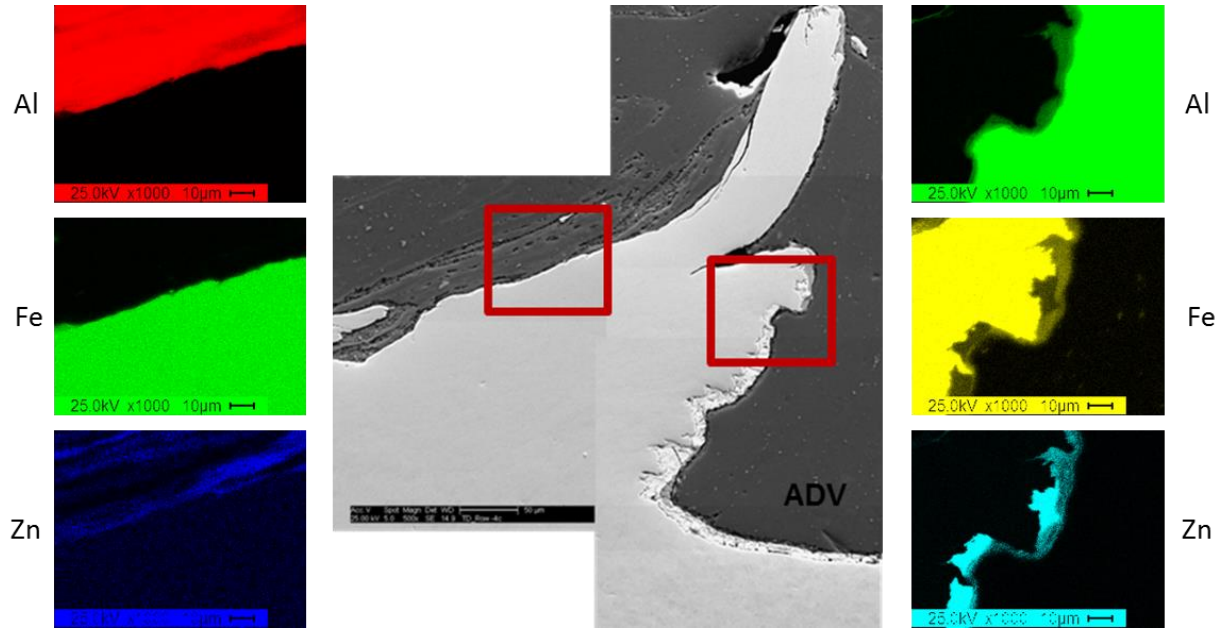

Figure 24 EDS chemical maps of Al, Fe, and Zn presence on inside and outside interfaces of the AS hook.

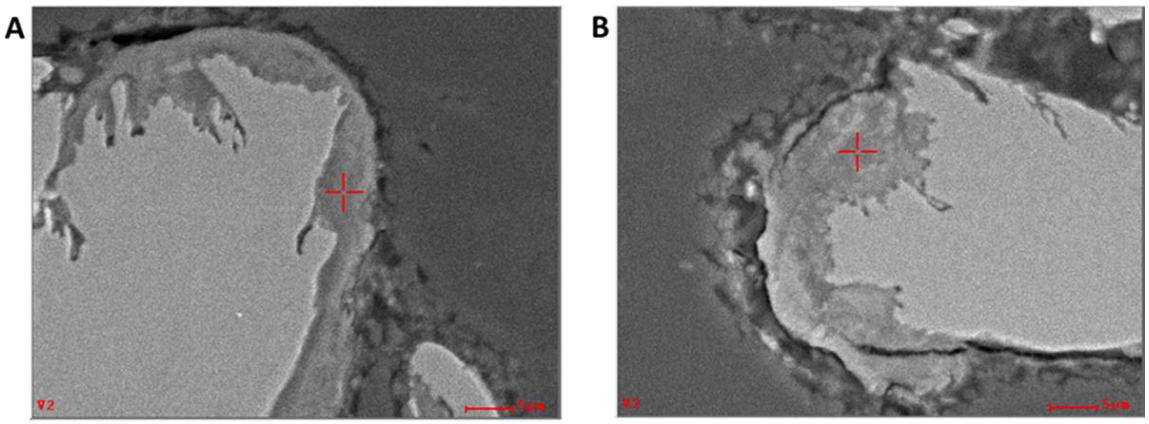

Element	Wt %	At %
AlK	57.76	75.18
FeK	23.21	14.59
ZnK	19.03	10.22

Element	Wt %	At %
AlK	48.44	68.32
FeK	16.78	11.43
ZnK	34.78	20.25

Figure 25 Point chemical analysis of IMC layer around (A) AS DP steel hook tip and (B) DP steel particle in AA6111-T4 WZ.

3.4 EBSD Crystallographic Analysis

3.4.1 AA6111-T4

The AA6111-T6 BM orientation map and pole figures in Figure 26 show a texture similar to that of an FCC rolling texture [37]. The degradation from what the ideal rolling texture would be may have been caused by solution aging heat treatment after the rolling. The turbulent structures caused by the large steel particles, intermetallic layers, and voids prevented clear diffraction patterns from being obtained, and thus EBSD mapping was not accomplished near the WZ interface. The WZ directly above the level of the large particles was mapped, however, in the regions between the upper parts of the hooks, as well as at mid-depth between the top of the weld and the interface. See Figure 27 and Figure 28 for these regions respectively. Figure 27 shows striations in the grain orientations, and the {111} PFs show shear fiber components, indicating recrystallized shear textures, rotated to various degrees depending upon the location relative to the weld center line. There was also a 90° rotation from (A) on the RS to (D) on the AS. The grains in the orientation maps in Figure 28 were more homogeneously mixed and lacked the striations in orientation that were present in Figure 27 however the textures were very similar. A 90° rotation in texture from RS to AS can also be observed here. Textures is in the TMAZs, shown in Figure 29, vary greatly from RS to AS and shear deformation texture components were difficult to identify.

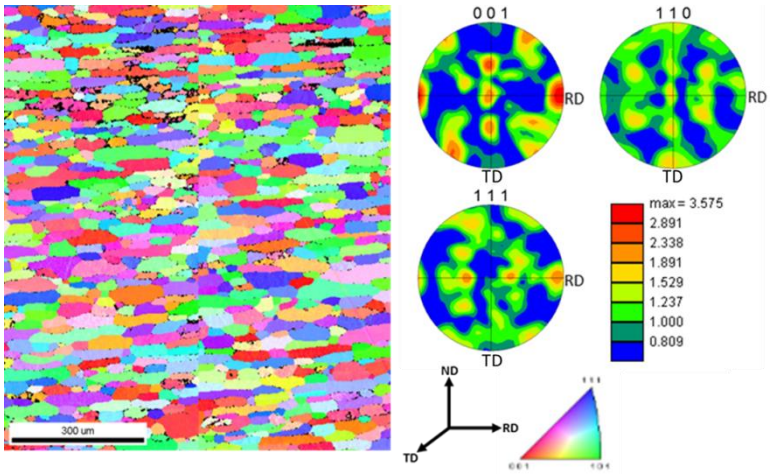

Figure 26 AA6111-T4 base metal. {111} PFs resembles FCC rolling texture.

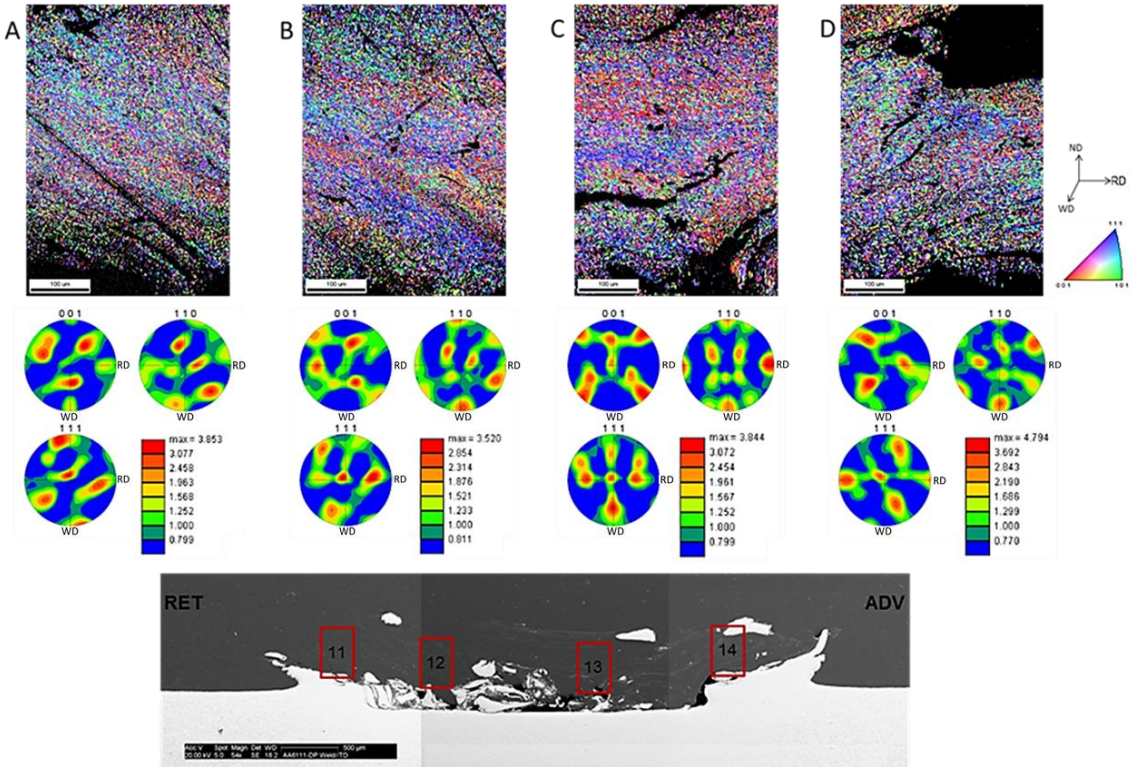

Figure 27 Orientation maps and PFs showing texture of AA6111-T4 grains in the WZ.

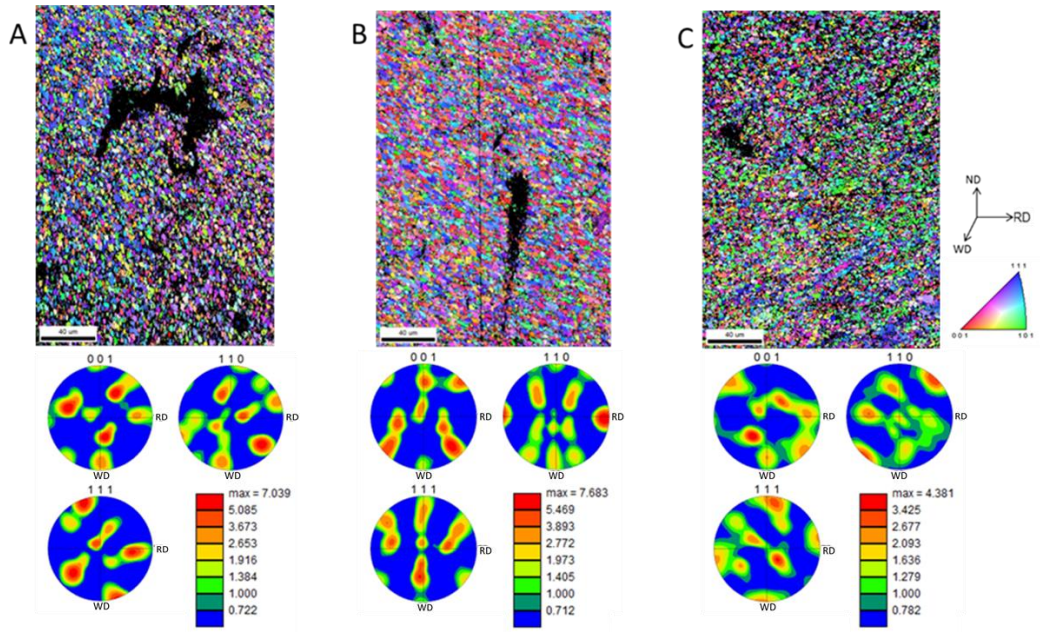

Figure 28 Orientation maps and PFs for mid-depth WZ microstructure. Texture shows a 90° rotation from RS (A) to AS (C).

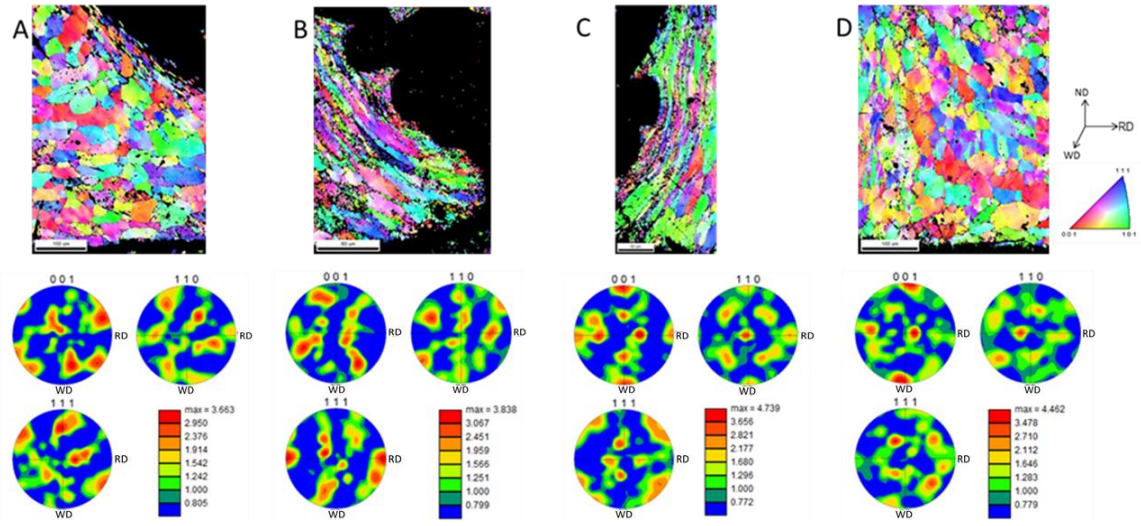

Figure 29 Orientation maps and PFs showing texture in the AA6111-T4 TMAZs.

3.4.2 DP Steel

The DP steel BM microstructure consisted of martensite grains within a ferrite matrix and a BCC rolling texture [37], seen in Figure 30. EBSD data for the BM-TMAZ transition regions are shown in Figure 31. The rolling texture was degraded slightly, indicating an increase in deformation however the TMAZ independent of any BM grains and WZ regions for the steel showed very low CI and were not properly indexed. Frequently, the TMAZ texture in FSWs just shows a rotation of the BM texture, as there is minimal effect on the crystallographic texture by bending of the crystals around the outside of the weld tool [36]. The texture here is rotated 90° relative to the BM texture shown in Figure 30 since the WD is parallel to the work piece RD.

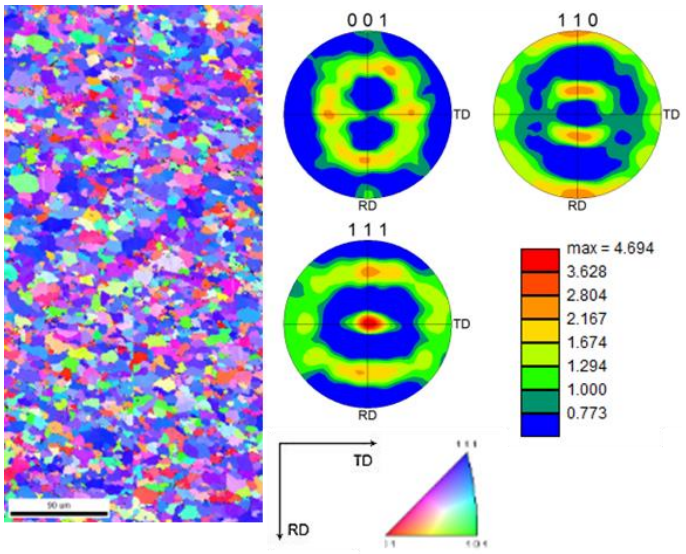

Figure 30 EBSD characterization of DP steel showing BCC rolling texture.

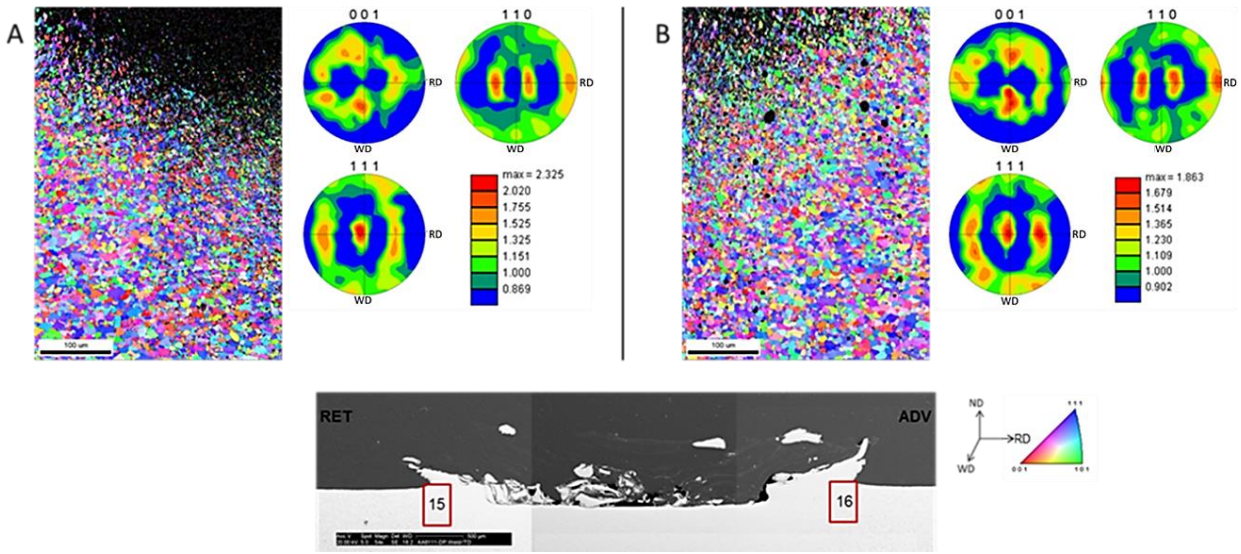

Figure 31 Orientation and texture of BM-TMAZ region showing near-BCC rolling texture. Rolling direction is normal to weld direction.

Chapter Four: Characterization of AA6061-T6/Wrought Steel Welds

4.1 Physical Features of the Microstructure

4.1.1 Qualitative Assessment of Weld Microstructure

The cross sections in the optical and SEM micrographs in Figure 32 and Figure 33 revealed that this weld was not nearly as turbulent as the AA6111-T4/DP steel weld, with very few medium-to-large wrought steel particles present in the AA6061 WZ matrix near the interface. The large steel particles were more isolated to the regions around and above the hooks, and voids and porosity did not appear to be present. There was, however, an IMC layer present at the interface between the aluminum and steel throughout the entire weld, as seen in Figure 34; the layer thickness was measured at approximately 2 μm and remained fairly constant across the weld interface. The IMC layers surrounding the randomly-shaped steel particles in the WZ varied more dramatically in thickness, especially where the shapes of the particles were most turbulent. Figure 35 shows a long crack which started under the AS hook tip and traveled through the IMC layer around the hook to the inside corner of the WZ where the AS hook starts. The presence of this crack gives evidence to the detrimental effects that IMCs can have on mechanical performance.

Figure 32 Composite of optical micrographs at 10x magnification showing weld cross section.

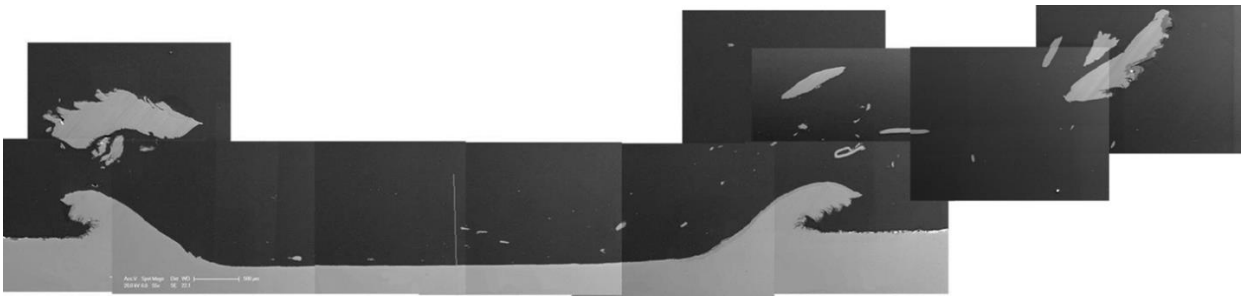

Figure 33 SEM micrograph at 55x magnification showing weld cross section.

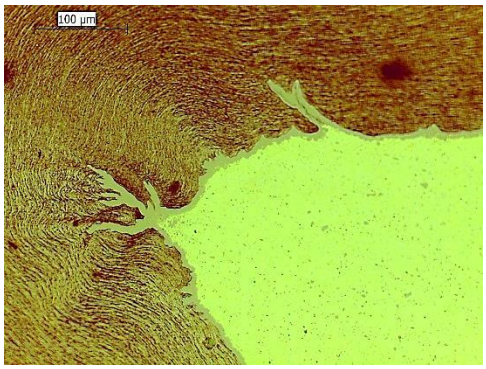

Figure 34 Optical micrograph at 20x magnification showing intermetallic compound layer between aluminum and steel.

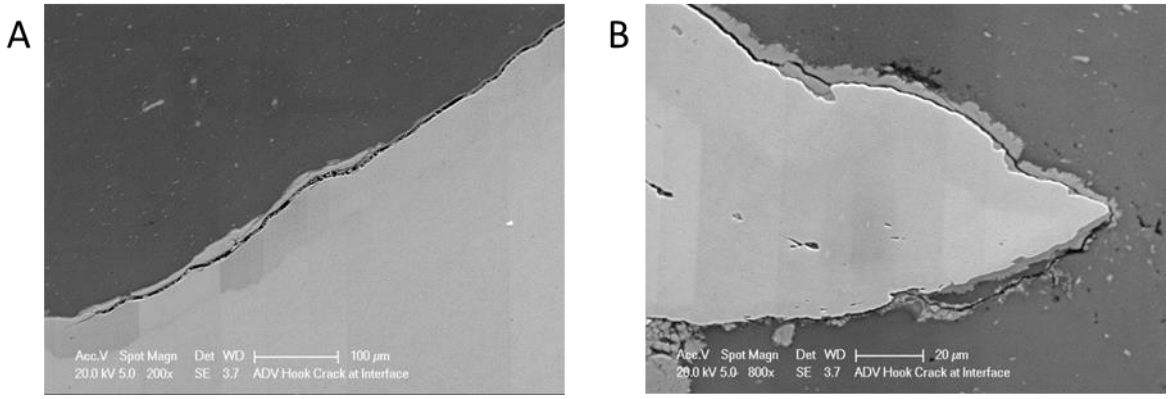

Figure 35 SEM micrographs of (A) end of crack at inside corner of the WZ, (B) start of micro-crack at the tip of the AS hook.

4.1.2 Steel Particle Volume Fraction and Grain Size

The volume fraction of wrought steel particles in the AA6061 WZ matrix was again measured using a point count. Figure 36 is a three-dimensional surface plot of V_{Fe} as a function of position across the weld (x) and distance from the weld interface (y). The tall peaks correspond to the large steel particles present above the RS and AS hooks. V_{Fe} remains small within the center of the WZ. Keeping the amount of particles stirred into the aluminum low will benefit the overall weld performance since it will reduce the amount of surface area on which IMC layers can precipitate.

The average grain size in the BM aluminum was 5540 μm^2 for the RS and 6950 μm^2 for the AS. These decreased slightly in the HAZ, but dropped by an order of magnitude in the TMAZs and again in the WZ where it was an average of approximately 100 μm^2. In fusion welding, the HAZ is often predicated by a noticeable increase in grain size and second-phase particles relative to the BM, however here, because the weld temperature is kept significantly

lower than what would occur in a fusion weld, coupled with the presence of severe plastic deformation, the HAZ grain size increase was not seen [60]. The wrought steel BM grain size was three orders of magnitude smaller than the aluminum BM grains size, at 3.5-4.0 μm^2. Grain size in the steel TMAZs ranged from 0.67-2.3 μm^2, with the smaller grains closest to the WZ. In the WZ, significant refinement occurred through recrystallization. This resulted in a grain size of 0.060 μm^2 in a region approximately 10 μm deep just below the weld interface. A distinct HAZ was not observed in the wrought steel. Figure 37 summarizes this data.

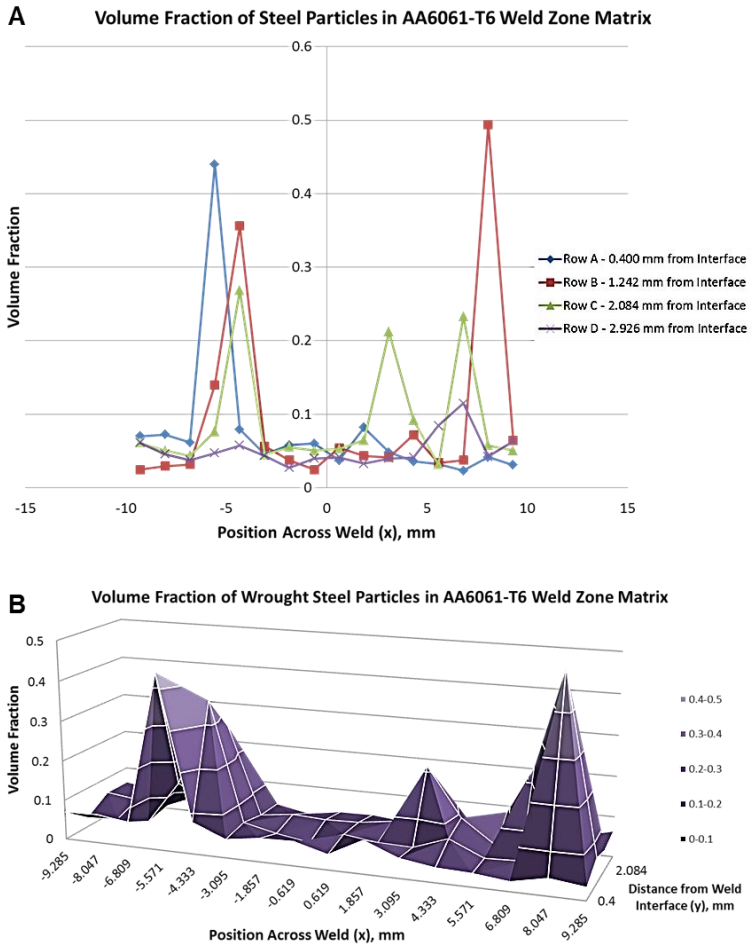

Figure 36 Volume fraction of steel particles in AA6061-T6 WZ matrix across the weld as (A) scatter plot and (B) 3D surface plot.

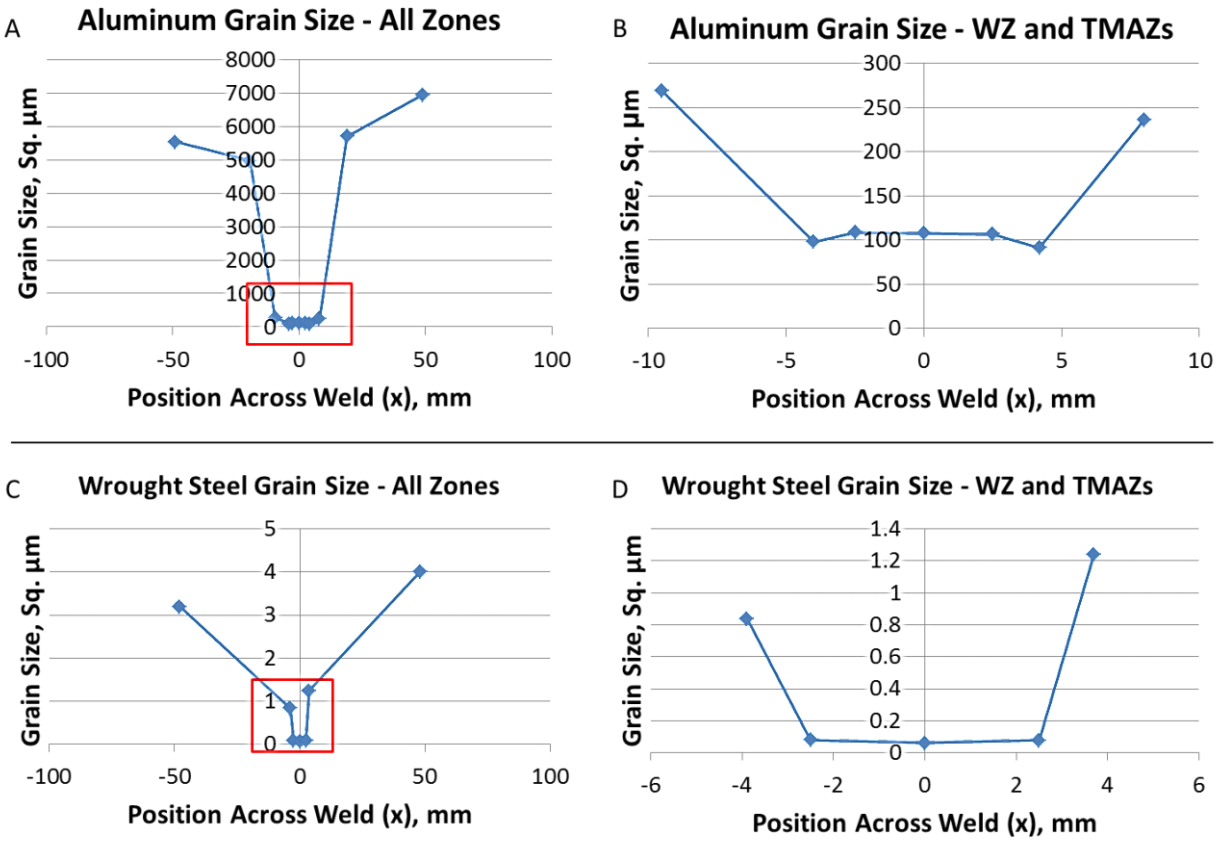

Figure 37 Grain size (area) plotted for (A) all zones of AA6061-T6, (B) WZ and TMAZ only of AA6061-T6, (C) all zones of wrought steel, (D) WZ and TMAZ of wrought steel.

4.2 Micro-Hardness

Vickers micro-hardness tests were performed in the aluminum at 0.5 mm, 1 mm, and 6 mm above the weld interface and plotted in Figure 38. Significant softening occurred in the WZ. Since the BM was a T6-temper alloy with Mg_2Si precipitation strengthening particles, it is most likely that the precipitates were re-solutionized when heated during the FSW process [44]. The peaks in hardness in the WZ nearer to the weld interface were assumed to be the result of very small steel and IMC particles being present, however these peaks do not compare with the hardness values measured in the steel. The maximum hardness was achieved in the TMAZs,

where deformation without recrystallization introduced lattice strain. The hardness dropped again in the HAZs, and steadily increased with distance from the weld out to the far edges of the BM, where there was no effect from the elevated temperature of the welding process.

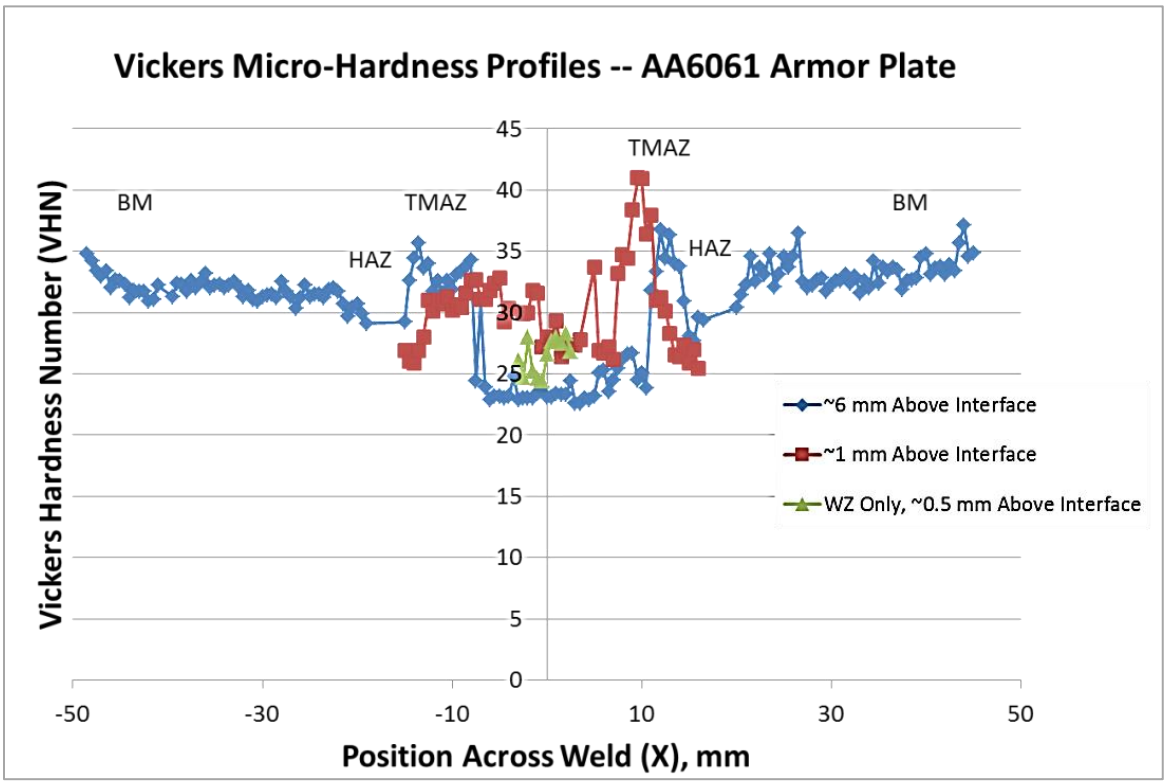

Figure 38 Micro-hardness profiles of AA6061-T6 across weld.

The hardness profiles in Figure 39 were obtained from the wrought steel at 0.5 mm below the weld interface to ensure that all the zones of the weld were measured. The drastic peaks and valleys in the BM were likely influenced by the presence and morphology of the martensite, which can exist in either a BCC or metastable body-centered tetragonal (BCT) structure [6]. The decrease in hardness in the WZ is even more significant than that of the aluminum WZ. Although the WZ grain size was very small, which would usually serve to increase strength, it is

reasonable to conclude that the heat input from the weld process relieved much of the lattice strain that maintained the hardness in the base metal. Any carbide present in the BM way have been re-solutionized as well [61]. The TMAZ and HAZ were not distinct in the hardness profile as they were in the aluminum profiles.

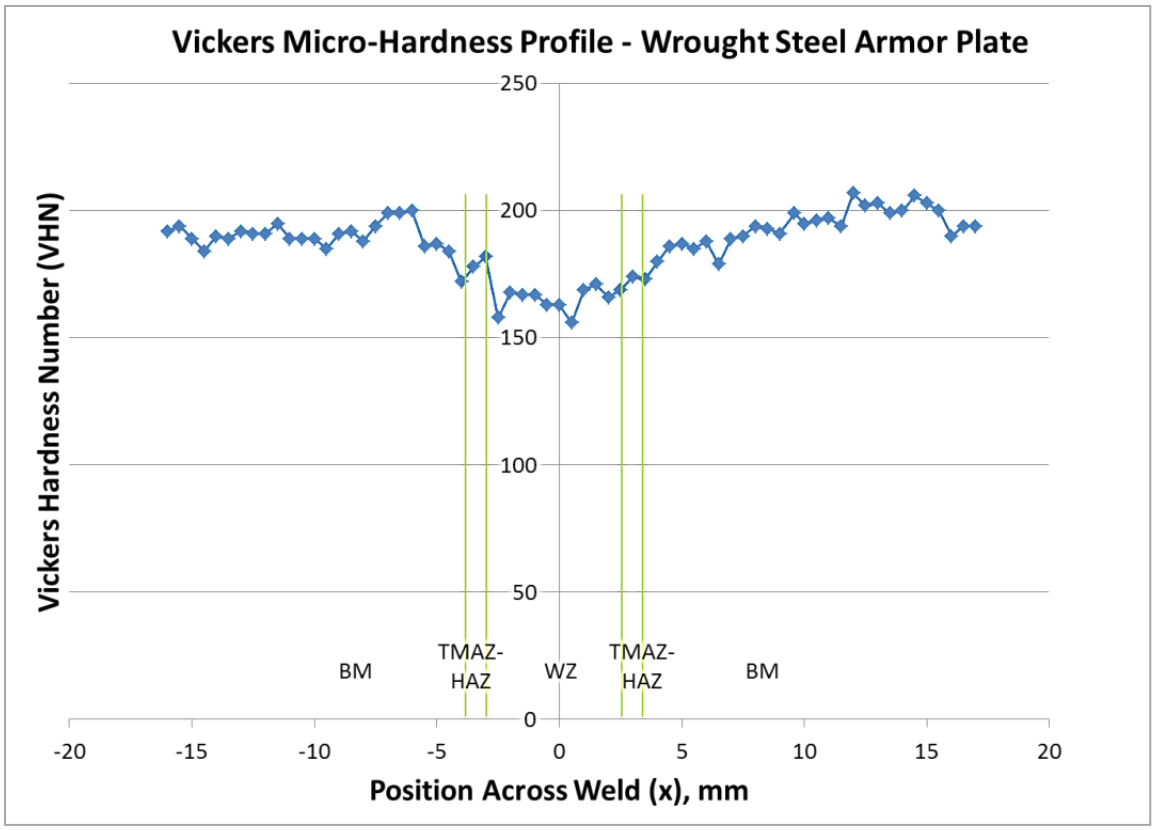

Figure 39 Micro-hardness profile of wrought steel across weld, 0.5 mm below weld interface.

4.3 Chemical Analysis and Intermetallic Compound Identification

The chemical maps in Figure 40 and Figure 41 show the overlap of aluminum atoms and iron atoms in the IMC layers and particles. Due to the thickness of the armor plates used in this

weld and a large volume of material being plasticized, it is likely that this weld was much slower to cool than the AA6111-T4/DP steel weld. The slower post-weld cooling rate would have encouraged temperature-dependent diffusion, allowing the IMC layer to grow over a longer period of time. It may be for this reason that the weld interface IMC layer was present in this weld and not in the AA6111-T4/DP steel weld. The chemistry collected from a point analysis shown in Figure 41 was compared to the Al-Fe binary phase diagram in Figure 22, and the IMC layer was identified as Al_3Fe, which has a monoclinic crystal structure. Incoherence between the monoclinic IMC layer and the cubic structures of the aluminum and steel likely added to its propensity for cracking. Additional chemical analysis data can be found in Appendix Six: EDS Chemical Analysis Data. Unfortunately, the IMC phase and crystal structure were not able to be verified using EBSD. As can be seen in Figure 42, the IMC regions in the EBSD orientation map were not indexed. Kikuchi diffraction patterns were not visible for the IMC layers throughout the weld cross section.

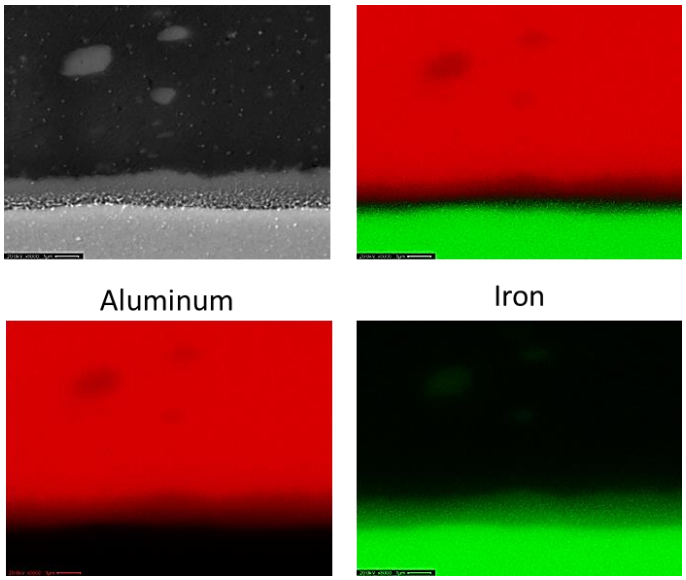

Figure 40 Chemical maps of Al and Fe overlap in IMC layer and the weld interface in the center of WZ.

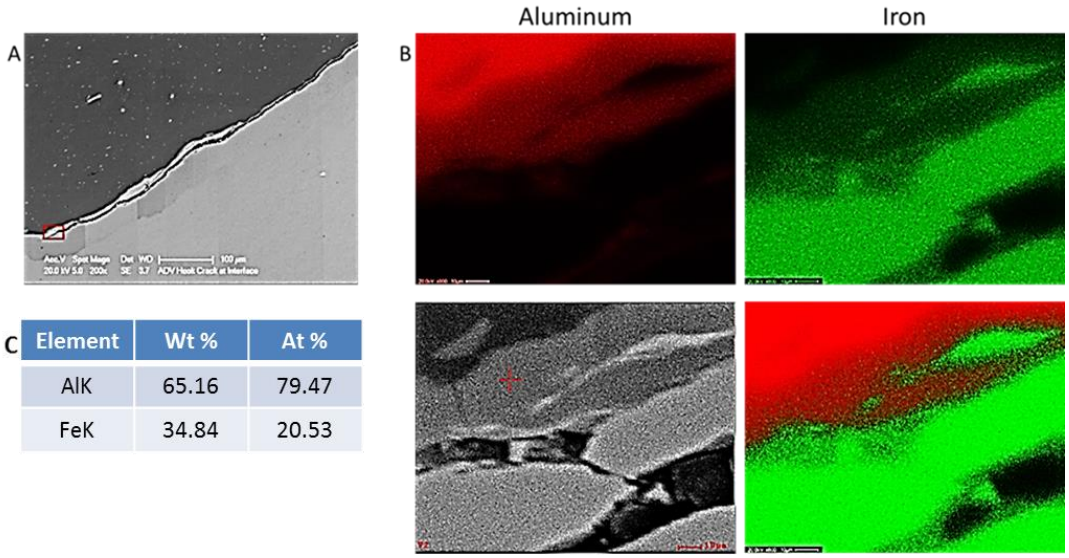

Element	Wt %	At %
AlK	65.16	79.47
FeK	34.84	20.53

Figure 41 Chemical maps of the end of the micro-crack that runs along the AS hook. Point analysis identifies this IMC as monoclinic Al_3Fe.

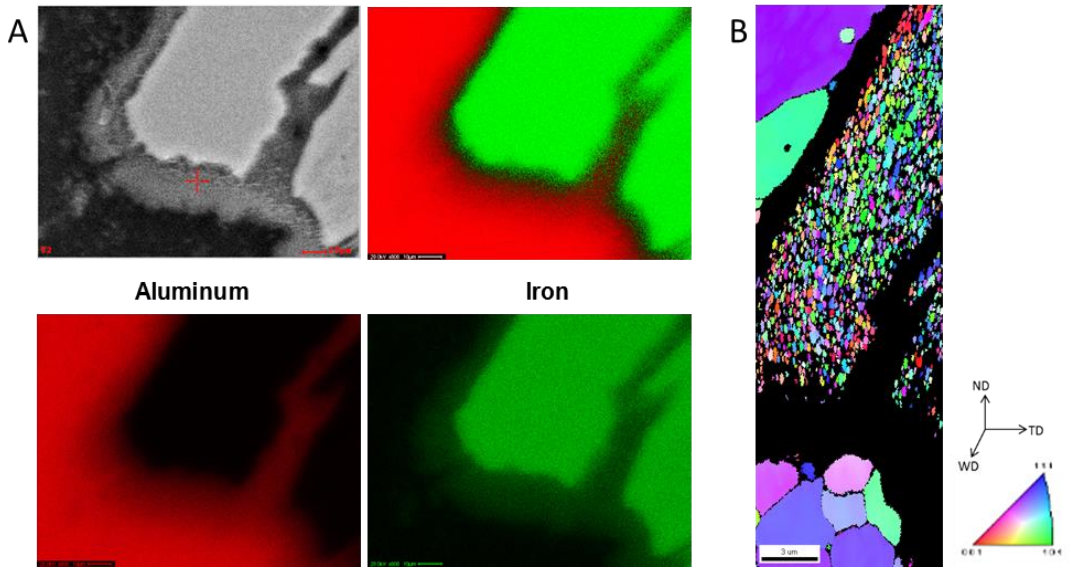

Figure 42 (A) SEM micrograph and chemical maps showing Al and Fe overlap in IMC layer around the edge of a steel particle, (B) EBSD orientation map showing grain structure of AA6061-T6 and wrought steel, but not IMC layer.

4.4 EBSD Crystallographic Analysis

4.4.1 AA6061-T6

Orientation maps and PFs for the AA6061-T6 BM and RS HAZ are shown in Figure 43 and Figure 44, respectively. The aluminum BM exhibited an FCC {111} rolling texture [37] with the RD parallel to the WD, as expected. Some degradation from the ideal rolling texture was observed and, like the AA6111-T4 BM, may have been the result of the solution aging heat treatment. Due to the overall size of the cross-sectional weld sample, it was difficult to locate the HAZ solely with EBSD. Instead the location of the HAZ region relative to the weld center was first identified by a noticeable decrease in micro-hardness from the profiles measured across the sample, shown above in Figure 38. The texture in the HAZ was very similar to that of the

BM, but the grain size was slightly smaller, as was discussed in Section 4.1.2 Steel Particle Volume Fraction and Grain Size.

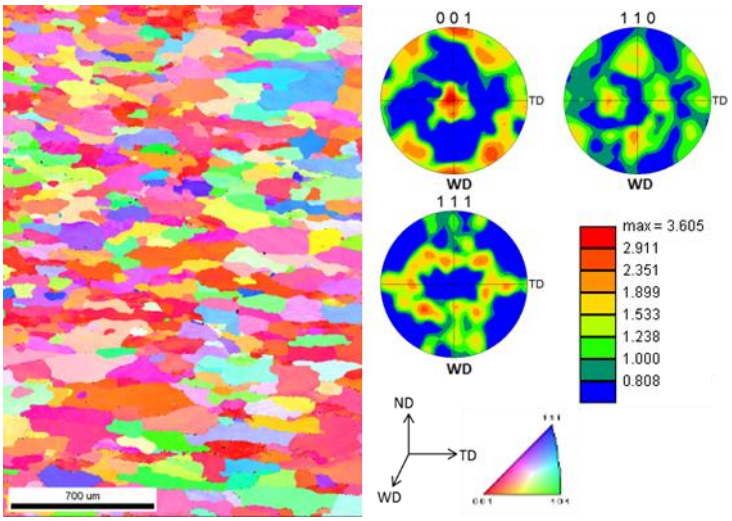

Figure 43 AA6061-T6 RS BM grain orientation maps and PFs showing FCC rolling texture.

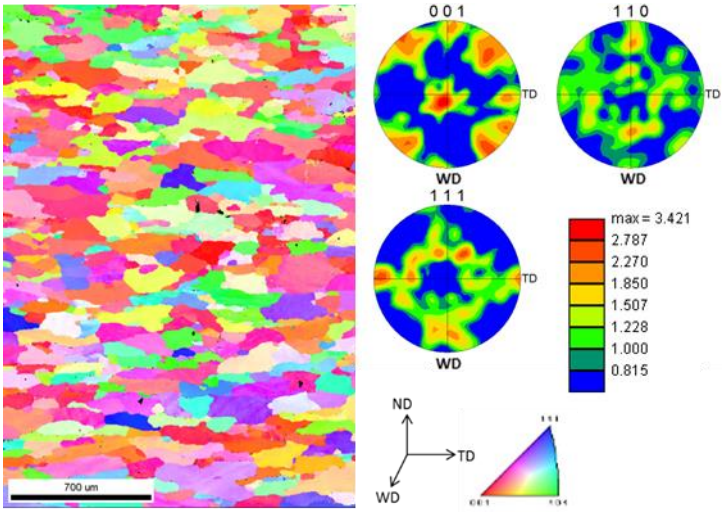

Figure 44 AA6061-T6 RS HAZ: grain orientation and PFs showing texture similar to FCC rolling texture.

The composite of multiple EBSD orientation maps in Figure 45 shows striated regions of texture through the WZ in the region between the hooks. It is likely that these striations were the product of the morphology of the threaded pin used to make the weld and the resulting flow of material around it. Figure 46 shows three distinct layers of texture in the PFs in (A) – (C). According to Rhodes et al., the material directly below the tip of the pin experiences both shearing and compression deformation [39]. This, coupled with the termination of the pin's scrolls at the pin tip and, more significantly, the presence of the scribe, create a microstructure at the interface that is much more complex and variable than would be expected for FSWs in similar alloys that do not necessitate the use of such complex tool geometry. These factors the likely cause of such distinct layering of the texture. The {111} PFs show recrystallized shear textures with varying levels of rotation between the layers. The intensity of the peaks in the PF in (A) is more than double the intensity in (C). This may have been influenced by proximity to the tool shoulder; the temperature during welding increases nearer to the shoulder which

undoubtedly has an effect on the crystallographic texture as well as other aspects of the weld microstructure, such as grain size.

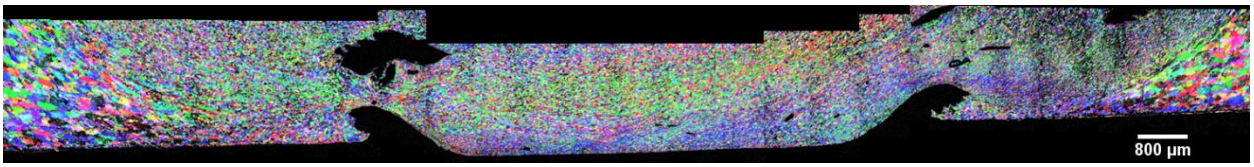

Figure 45 Composite of orientation maps across weld at interface showing striation in WZ texture and transition into TMAZ.

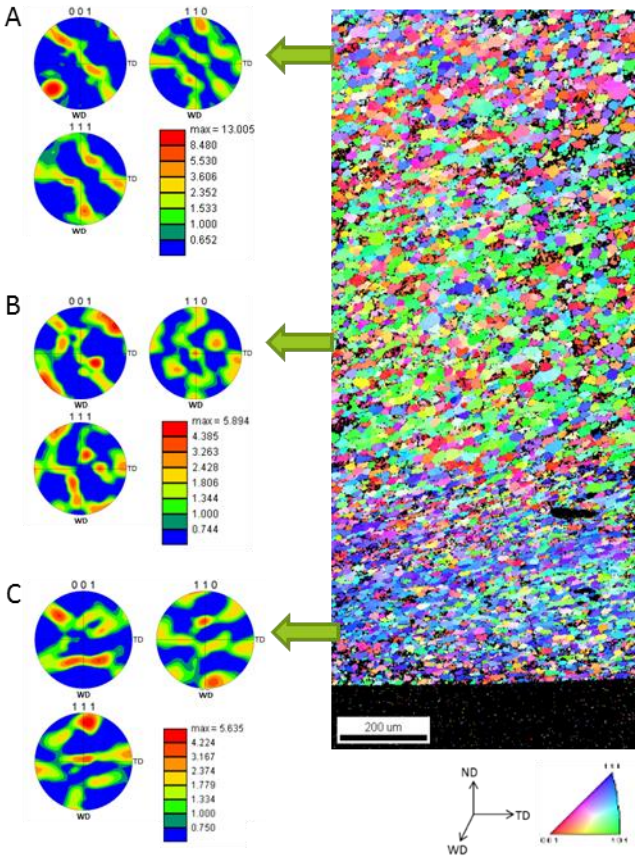

Figure 46 AA6061-T6 WZ center showing layers of differing textures (A-C). {111} PF in (C) shows partial B-fiber with the SD rotated slightly CCW from parallel to WD.

Figure 47 (A-E) displays the textures across the weld interface from the RS hook to the AS hook. The Al WZ extended outside the hooks, but this was due solely to the rotation of the pin and not the scribe in those regions. These regions also experienced shear deformation but are not shown here. The {111} PFs show shear fiber components with the SD and SPN rotated to varying degrees based on distance from the weld center. The textures in the regions above the RS and AS hooks showed the SD aligned with the WD, while the textures in the regions between the hooks were rotated with the SPN more closely oriented along the WD. This was consistent with shear texture orientations found in the literature [36,37]. The recrystallized shear textures showed varying degrees of degradation from an ideal simple shear texture (see Figure 4 and Figure 5) but this can generally be explained by the complexity and severity of the deformation. The forward travel of the tool past the point at which the textures are examined here would have caused the shear plane to be tangent the back surface of the tool. This accounts for the rotation of the SD and SPN seen here.

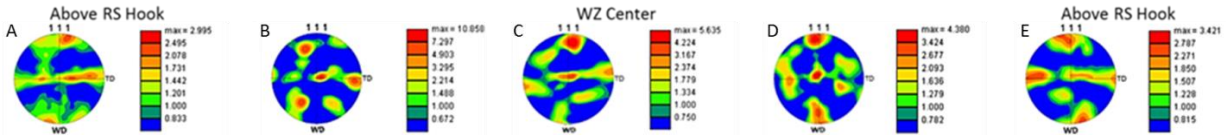

Figure 47 PFs showing texture across WZ interface from RS hook in (A) to AS hook in (E). {111} PFs show partial B-fibers with SD aligned closed to WD and SPN aligned close to TD.

The RS {111} texture in TMAZ shown in Figure 48 (A) resembles that of the {111} texture for the region of refined grains adjacent to the weld tool on the RS of the FSW studied by Fonda et al. [35] which shows <111> aligned with the sample ND. The SD is aligned with the sample WD and the SPN aligned with TD as expected. The texture studied here only includes a

small region of refined grains, which may account for the differences between it and that examined by Fonda et al. It is not unexpected that the TMAZ textures would be different from the RS to the AS, since the character of the deformation is also different on the two sides. The RS TMAZ was wider and blends more gradually into the equiaxed grains of the WZ where the material is extruded behind the tool as it passes. The region of elongate grains next to the WZ on the AS tends to terminate more sharply since the material is swept forward and around the front of the tool [27,35]. More texture data can be found in Appendix Seven: EBSD Data.

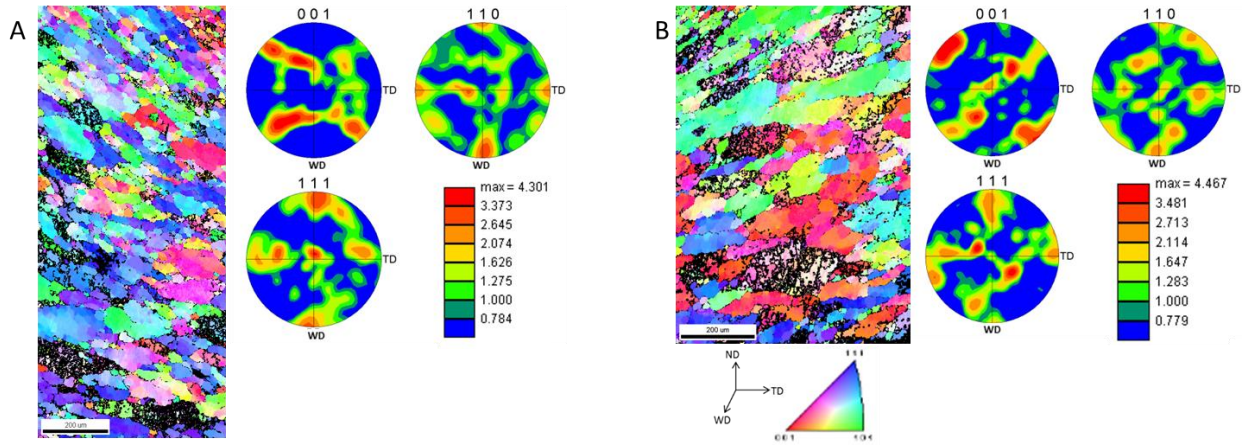

Figure 48 AA6061-T6 TMAZ (A) RS and (B) AS.

4.4.2 Wrought Steel

The wrought steel armor plate used here underwent a quench and temper heat treatment after rolling and prior to the welding process, which produced a BCC martensitic structure [37]. The PFs in Figure 49 show a BCC rolling texture with the rolling direction normal to the weld direction. The textures in the RS and AS TMAZs in Figure 50 were very similar to the BM, but with rotations in opposite direction on either side caused by the deformation of the grains around

the outside of the tool. Like the WZ in the aluminum, the steel WZ also showed layers of different textures accompanied by changes in grain shape, as can be seen in the orientation map and PFs in Figure 51 (A-C). The {110} PF in (A) shows a recrystallized shear texture, with the SD aligned with TD and SPN aligned with WD. As distance from the weld interface increased, the shear texture components became less identifiable.

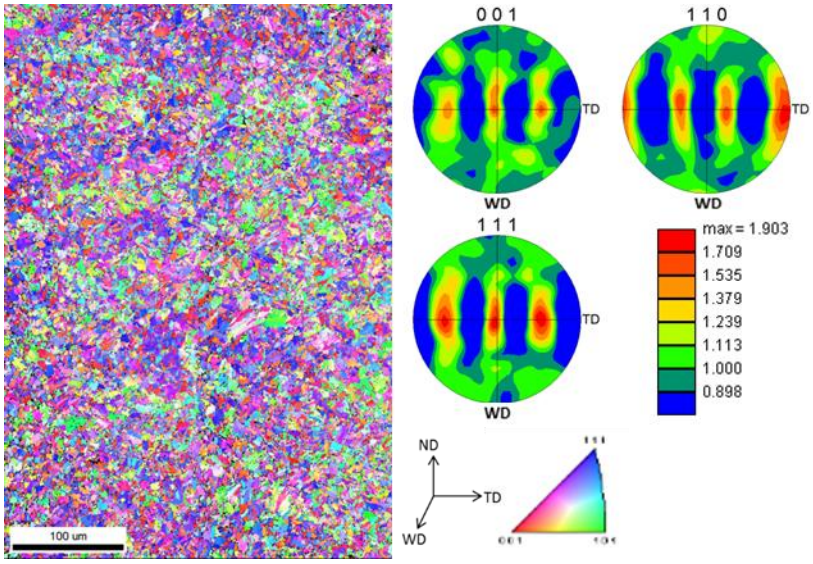

Figure 49 Wrought steel AS BM: BCC rolling texture, with RD of the steel plate normal to WD.

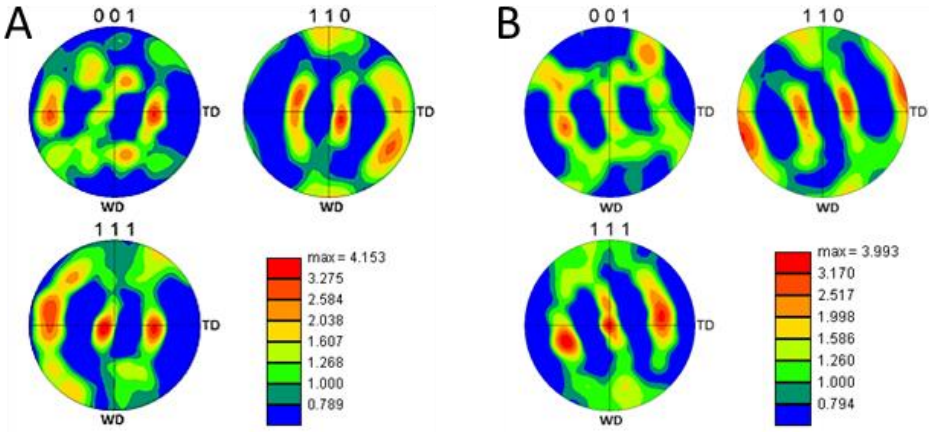

Figure 50 Texture in wrought steel TMAZ with close similarities to BM texture but with slight rotation. (A) RS and (B) AS.

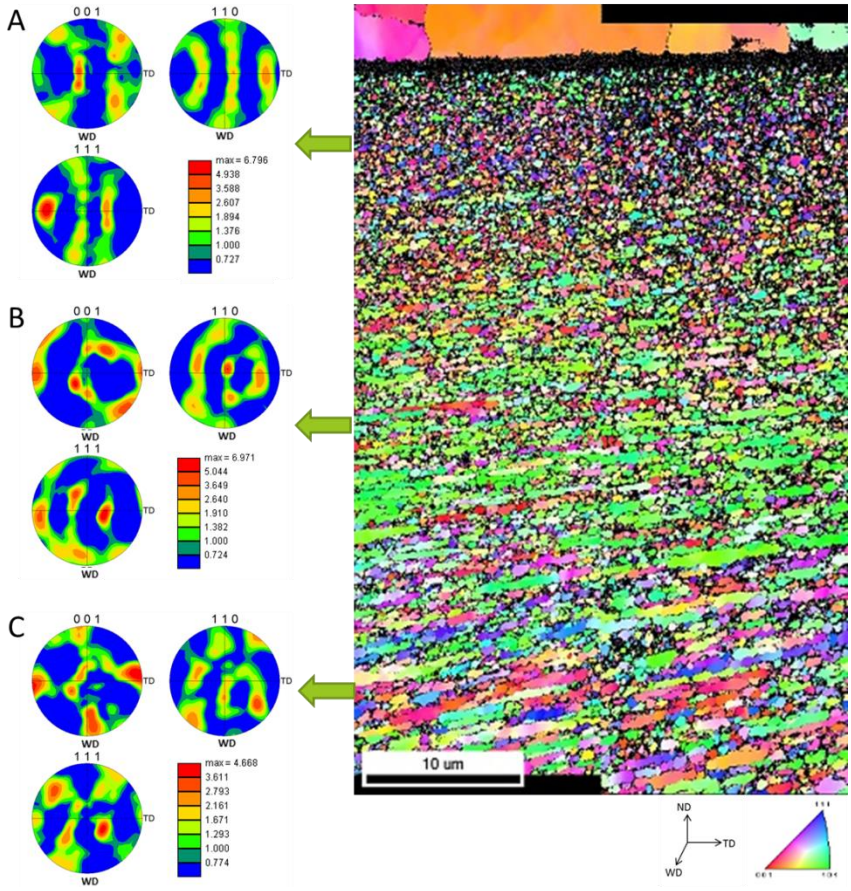

Figure 51 Striated layers of texture and grain size in wrought steel WZ center at 5000x magnification.

Chapter 5: Conclusions

In this study, the microstructures of two aluminum-steel dissimilar lap friction stir welds were characterized in order to assess their quality and aid in the prediction of mechanical performance. The specific features examined were grain size, volume fraction of steel particles in the aluminum weld zone matrices, qualitative assessment of the presence of defects, Vickers micro-hardness, chemical analysis, and crystallographic orientation and texture.

In the AA6111-T4/DP steel weld, very large steel particles were present within the aluminum WZ matrix near the interface, surrounded by several large voids and a highly turbulent structure. Voids may have been the result of a disruption in the plastic flow of the aluminum caused by the presence of the large particles which were the result of milling of the steel surface by the WC scribe. Porous regions are present in the aluminum where the zinc coating from the galvannealed DP steel melted and went into solid solution. The steel particles stirred into the aluminum near the interface were more concentrated on the RS where the material was extruded behind the weld tool. The presence of wrought armor steel particles dispersed throughout the AA6061 WZ matrix was significantly lower. No voids or porosity were observed in the AA6061/wrought steel welds either, however there was a long crack that traveled from the inside corner of the WZ at the AS hook to the outside of the hook tip through an intermetallic compound layer located at the WZ interface. Both welds showed substantial grain refinement within the WZs and TMAZs through recrystallization and plastic deformation respectively. Softening of the alloys in the WZs was concluded to be the result of re-solutionizing of second-phase strengthening particles and relaxation of lattice strain due to the heat input of the weld process.

Both welds achieved mechanical and chemical bonds through the formation of the steel hooks at the weld interfaces and temperature-dependent diffusion of Al and Fe at the interface boundaries. Binary and ternary Al-Fe, Al-Zn, Fe-Zn, and Al-Fe-Zn combinations present within the AA6111/DP steel weld, and while compositions were measured through EDS point chemical analysis at various locations, specific IMC phases were not identified. In some cases, distinct IMC layers were not discernible and it was concluded that the elements, specifically zinc, existed there in solid solution. In the AA6061/wrought steel welds, distinct IMC layers were present between the aluminum and steel throughout the entire WZ. The layer across the interface was measured at approximately 2 μm thick, but around the surfaces of steel particles mixed into the WZ the thickness varied substantially. Point chemical analysis from EDS identified these IMC layers as monoclinic Al_3Fe. The low level of symmetry in the monoclinic structure and the incoherence with the cubic aluminum and steel alloys may have encouraged cracking.

The BM for the aluminum and steel alloys showed FCC and BCC rolling textures, respectively. IMC layers were not indexed with EBSD since diffraction patterns were not detectable in those regions. Shear texture components were observed in the aluminum and steel WZs as well as the TMAZs in both aluminum alloys, with varying degrees of rotation based on location relative to the weld center. The TMAZs in the steel exhibited rotated rolling textures. Divergence from ideal simple shear and changes in rotation of the SD and SPN in relation to the TD and WD were attributed to the severity of deformation induced by the FSW process and the complex weld tool geometry.

Chapter 6: Future Work

Because of the complexity of the microstructure induced by FSW, there are several points of interest that could not be addressed in this study. Future work on characterizing these welds should focus on:

- Assessing how the weld parameters could be changed to influence the microstructure. Ideally, the parameters should be selected such that the weld temperature is kept as low as possible while still achieving a satisfactory bond. Decreasing the weld temperature can be accomplished by decreasing the rotational speed of the tool and increasing the lateral weld speed, allowing the work piece material to cool more quickly. Keeping the weld temperature low would decrease the effect of temperature-dependent diffusion which results in IMC precipitation and growth. While the IMC layers found in the welds studied here were fairly thin by comparison to those found in other studies in the literature, their presence should be studied in-depth and minimized as much as possible to maintain the integrity of the weld joints.
- EBSD characterization of IMCs. This should be used to verify the identification of the monoclinic Al_3Fe IMC in the AA6061-T6/wrought steel weld. The identification of this IMC was based solely on the equilibrium phase diagram, which cannot give information on the degree of crystallinity or other data such as grain size which would be influenced by the amount of time at-temperature and the cooling rate.
- Obtaining crystallographic and grain size data from regions of the AA6061-T6/wrought steel weld not examined here, i.e. mid-depth for aluminum WZ and top of WZ near the shoulder. Texture intensity and grain growth increases with proximity to the tool

shoulder where the temperature is higher compared with the regions nearer the weld interface.

- Measuring the width of the WZ, TMAZ and HAZ relative to position on the vertical axis (ND) of the weld. When a tapered pin is used, the weld region (including the WZ, TMAZ and HAZ) can be idealized as a cone shape, since the weld is significantly wider near the top of the weld. This could be done with EBSD characterization or through Vickers micro-hardness indentation at several depths and would give a better indication of weld performance.
- Studying more in-depth the recrystallization mechanism taking place within the weld zones of the aluminum and steel alloys.
- Identifying and characterizing the precipitation hardening particles in BM aluminum and steel alloys, and how they change through the zones of the weld cross section. This would aid in predicting mechanical performance. The size of these particles is frequently on the order of tens of nanometers, so it may be necessary to used transmission electron microscopy to measure them.

References

1. K. Kimapong, T. Watanabe. “Friction Stir Welding of Aluminum Alloy to Steel” *Weld J* (2004) 277-282.

2. R. Johnson and P.L. Threadgill. “Progress in friction stir welding of aluminum and steel for marine applications.” TWI: Published Papers. October, 2013. http://www.twi.co.uk/technical-knowledge/published-papers/progress-in-friction-stir-welding-of-aluminium-and-steel-for-marine-applications-october-2003/ Accessed May 21, 2013.

3. H. Uzun, C.D. Donne, A. Argagnotto, T. Ghidini, C. Gambaro. “Friction stir welding of dissimilar Al 6013-T4 to X_5CrNi_{18}-10 stainless steel.” *Mater Design* 26 (2005) 41-46.

4. R.M. Leal, A. Loureiro. “Effect of overlapping friction stir welding passes in the quality of welds of aluminum alloys.” *Mater Design* 29 (2008) 982-991.

5. S. Xu, X. Deng. “A study of texture patterns in friction stir welds.” *Acta Mater* 56 (2008) 1326-1341.

6. J. Young, D. Field, T. Nelson. “Material flow during friction stir welding of HSLA 65 steel.” *Metall Mater Trans A* 44, 7 (2013) 3167-3175.

7. M.A. Sutton, B. Yang, A.P. Reynolds, R. Taylor. “Microstructural studies of friction stir welds in 2024-T3 aluminum.” *Mater Sci Eng A* 323 (2002) 160-166.

8. D.A. Wang, S.C. Lee. “Microstructure and failure mechanisms of friction stir spot welds of aluminum 6061-T6 sheets.” *J Mater Process Tech* 186 (2007) 291-297.

9. S.J. Kalita. “Microstructure and corrosion properties of diode laser melted friction stir weld of aluminum alloy 2024 T351.” *Appl Surf Sci* 257 (2011) 3985-3997.

10. M.A. Sutton, A.P. Reynolds, B. Yang, R. Taylor. “Mode I fracture and microstructure for 2024-T3 friction stir welds.” *Mater Sci Eng A* 354 (2003) 6-16.

11. D.A. Wang, C.H. Chen. “Fatigue lives of friction stir spot welds in aluminum 6061-T6 sheets.” *J Mater Process Tech* 209 (2009) 367-375.

12. A.A.M. da Silva, E. Arruti, G. Janeiro, E. Aldanondo, P. Alvarez, A. Echeverria. “Material flow and mechanical behaviour of dissimilar AA2024-T3 and AA7075-T6 aluminium alloys friction stir welds.” *Mater Design* 32 (2011) 2021-2027.

13. M.B. Prime, T. Gnäupel-Herold, J.A. Baumann, R.J.Lederich, D.M. Bowden, R.J. Sebring. “Residual stress measurements in a thick, dissimilar aluminum alloy friction stir weld.” *Acta Mater* 54 (2006) 4013-4021.

14. V-X. Tran, J. Pan. “Fatigue behavior of dissimilar spot friction welds in lap-shear and cross-tension specimens of aluminum and steel sheets.” *Int J Fatigue* 32 (2010) 1167-1179.

15. M. Boz, A. Kurt. “The influence of stirrer geometry on bonding and mechanical properties in friction stir welding process.” *Mater Design* 25 (004) 343-347.

16. W.F. Xu, J.H. Liu, D.L. Chen. “Material flow and core/multi-shell structures in a friction stir welded aluminum alloy with embedded copper markers.” *J Alloy Compd* 509 (2011) 8449-8454.

17. V-X. Tran, J. Pan, T. Pan. “Fatigue behavior of spot friction welds in lap-shear and cross-tension specimens of dissimilar aluminum sheets.” *Int J Fatigue* 32 (2010) 1022-1041.

18. TWI FAQs: Can friction stir welding be used to make lap joints?. TWI Ltd. 2012. http://www.twi.co.uk/technical-knowledge/faqs/process-faqs/faq-can-friction-stir-welding-be-used-to-make-lap-joints/. Accessed July 11, 2012.

19. W.H. Jiang, R. Kovacevic. “Feasibility study of friction stir welding of 6061-T6 aluminium alloy with AISI 1018 steel.” *Proc Instn Mech Engrs Vol 218 Part B: J. Eng Manu.*

20. T. Tanaka, T. Morishige, T. Hirata. “Comprehensive analysis of joint strength for dissimilar friction stir welds of mild steel to aluminum alloys.” *Scripta Mater* 61 (2009) 756-759.

21. S. Jana, Y. Hovanski. “Fatigue behaviour of magnesium to steel dissimilar friction stir lap joints.” *Sci Technol Weld Joi* 17 (2012) 141-145.

22. C.M. Chen, R. Kovacevic. “Joining of Al 6061 alloy to AISI 1018 steel by combined effects of fusion and solid state welding.” *Int J Mach Tool Manu* 44 (2004) 1205-1214.

23. Y. Hovanski, M.L. Santella, G.J. Grant. “Friction stir spot welding of hot-stamped boron steel.” *Scripta Mater* 57 (2007) 873-876.

24. H.-H. Cho, S.H. Kang, S.-H. Kim, K.H. Oh, H.J. Kim, W.-S. Chang, H.N. Han. “Microstructural evolution ahead in friction stir welding of high-strength linepipe steel.” *Mater Design* 34 (2012) 258-267.

25. S. Jana, Y. Hovanski, G.J. Grant. “Friction stir lap welding of magnesium alloy to steel: A preliminary investigation.” *Metall Mater Trans A* 41A (2010) 3173-3182.

26. S. Jana, Y. Hovanski, G.J. Grant, K. Mattlin. “Effect of tool feature on the joint strength of dissimilar friction stir lap welds.” TMS International Conference Proceedings. 2011.

27. R.W. Fonda, J.F. Bingert. “Texture variations in an aluminum friction stir weld.” *Scripta Mater* 57 (2007) 1052-1055.

28. C.B. Fuller, M.W. Mahoney, M. Calabrese, L. Micona. “Evolution of microstructure and mechanical properties in naturally aged 7050 and 7075 Al friction stir welds.” *Mater Sci Eng A* 527 (2010) 2233-2240.

29. S.T. Amancio-Filho, S. Sheikhi, J.F. dos Santos, C. Bolfarini. “Preliminary study on the microstructure and mechanical properties of dissimilar friction stir welds in aircraft aluminum alloys 2024-T351 and 6056-T4.” *J Mater Process Tech* 206 (2008) 132-142.

30. H. Dong, W. Hu, Y. Duan, X. Wang, C. Dong. “Dissimilar metal joining of aluminum alloy to galvanized steel with Al-Si, Al-Cu, Al-Si-Cu and Zn-Al filler wires.” *J Mater Process Tech* 212 (2012) 458-464.

31. T. Watanabe, H. Takayama, A. Yanagisawa. “Joining of aluminum alloy to steel by friction stir welding.” *J Mater Process Tech* 178 (2006) 342-349.

32. Syahbuddin, P.R, Munroe, B. Gleeson. “The develovment of Fe-An intermetallic compounds in solid Fe/Zn and Fe/Zn-Al diffusion couples during short-term annealing at 400°C.” *Mater Sci Eng A* 264 (1999) 201-209.

33. W-B Lee, M. Schmuecker, U.A. Mercardo, G. Biallas, S-B Jung. “Interfacial reaction in steel-aluminum joints made by friction stir welding.” *Scripta Mater* 55 (2006) 355-358.

34. M. Movahedi, A.H. Kokabi, S.M. Seyed Reihani, W.J. Cheng, C.J. Wang. “Effect of annealing treatment on joint strength of aluminum/steel friction stir lap weld.” *Mater Design* (2012), doi: http://dx.doi.org/10.1016/j.matdes.2012.08.028

35. R.W. Fonda, J.F. Bingert, K.J. Colligan. “Development of grain structure during friction stir welding.” *Scripta Mater* 51 (2004) 243-248.

36. D.P. Field, T.W. Nelson, Y. Hovanski, K.V. Jata. “Heterogeneity of crystallographic texture in friction stir welds of aluminum.” *Metall Mater Trans A* 32 (2001) 2869-2867.

37. U.F. Kocks, C.N. Tomé, H.-R. Wenk. *Texture and Anisotropy: Preferred Orientations in Polycrystals and their Effect on Materials Properties*. Cambridge: Cambridge University Press. 2000.

38. Z.Y. Ma, R.S. Mishra, M.W. Mahoney. “Superplastic deformation behavior of friction stir processed 7075 Al alloy.” *Acta Mater* 50 (2002) 4419-4430.

39. C.G. Rhodes, M.W. Mahoney, W.H. Bingel, M. Calabrese. “Fine-grain evolution in friction stir processed 7050 aluminum.” *Scripta Mater* 48 (2003) 1451-1455.

40. S. Gourdet, F. Montheillet. "A model of continuous dynamic recrystallization." *Acta Mater* 51 (2003) 2685-2699.

41. Y.S. Sato, T.W. Nelson, C.J. Sterling, R.J. Steel, C.-O. Pettersson. "Microstructure and mechanical properties of friction stir welded SAF 2507 super duplex stainless steel." *Mater Sci Eng A* 397 (2005) 376-384.

42. H.G. Salem, A.P. Reynolds, J.S. Lyons. "Microstructure and retention of superplasticity of friction stir welded superplastic 2095 sheet." *Scripta Mater* 46 (2002) 337-342.

43. "Aluminum Tempers, Specifications and Designations." Engineers Edge: Solutions by Design. http://www.engineersedge.com/aluminum_tempers.htm. Copy Right 2000-2013 by Engineers Edge, LLC. Accessed April 8, 2013.

44. Y.-C. Chen, D. Bakavos, A. Gholinia, P.B. Pragnell. "HAZ development and accelerated post-weld natural ageing in ultrasonic spot welding aluminium 6111-T4 automotive sheet." *Acta Mater* 60 (2012) 2816-2828.

45. S. Pogatscher, H. Antrekowitsch, H. Leitner, T. Ebner, P.J. Uggowitzer. "Mechanisms controlling the artificial aging of Al-Mg-Si alloys." *Acta Mater* 59 (2011) 3352-3363.

46. Detail Specification: Armor Plate, Aluminum Alloy, Unweldable Applique 6061. MIL-DTL-32262 (MR). 31 July 2007.

47. Detail Specification: Armor plate, steel, wrought, homogeneous (for use in combat-vehicles and for ammunition testing). MIL-DTL-1560J (MR). 24 July 2009.

48. A.O. Benscoter, B.L. Bramfitt. "Metallography and microstructures of low-carbon and coated steels." *ASM Handbook, Vol 9: Metallography and Microstructures*. 2004.

49. J.C. Russ. *Practical Stereology* 2nd ed. New York: Plenum Press. 1999.

50. P. J. Goodhew, J. Humphreys, and R. Beanland. *Electron Microscopy and Analysis*. 3rd ed. London and New York: Taylor & Francis. 2001.

51. SEM Q&A Book. JEOL Ltd. http://www.medicine.mcgill.ca/femr/SEM%20Sample%20Prep%20JEOL.pdf Accessed June 24, 2013.

52. D. S. MacKenzie and G. E. Totten. *Analytical Characterization of Aluminum, Steel, and Superalloys.* CRC Press, Boca Raton, Fl. 2006.

53. O. Engler, V. Randle. *Introduction to Texture Analysis: Macrotexture, Microtexture, and Orientation Mapping* 2nd ed. Boca Raton, London and New York: CRC Press. 2010.

54. W. D. Callister, Jr., *Materials Science and Engineering: An Introduction.* 7th ed. New York: Wiley. 2007.

55. S. Kalpakjian, S.R Schmid, *Manufacturing Processes for Engineering Materials*. 5th ed. Upper Saddle River: Prentice. 2008.

56. A.R.B Verma, W.J. van Ooij. "High-temperature batch hot-dip galvanizing, Part 1. General description of coatings formed at 560°C." *Surface and Coatings Technology* 89 (1997) 132-142.

57. J.D. Culcasi, P.R. Seré, C.I. Elsner, A.R. Di Sarli. "Control of the growth of zinc-iron phases in the hot-dip galvanizing process." *Surf Coat Tech* 122 (1994) 21-23.

58. A.R. Marder. "The metallurgy of zinc-coated steel." *Prog Mater Sci* 45 (2000) 191-271.

59. ASM Metals Handbook Online, Vol. 3: Alloy Phase Diagrams. http://products.asminternational.org/hbk/index.jsp

60. B.V. Gunaraj, N. Murugan. "Prediction of heat-affected zone characteristics in submerged arc welding of structural steel pipes." *Weld J* (2002). http://aws.org/wj/supplement/Gunaraj2-02.pdf. Accessed June 24, 2013.

61. J. Unfried S., C.M. Garzón, J.E. Giraldo. "Numerical and experimental analysis of microstructure evolution during arc welding in armor plate steels." *J Mater Process Tech* 209 (2009) 1688-1700.

Appendices

Appendix One: Tool Dimensions for AA6111-T4/DP Steel Weld

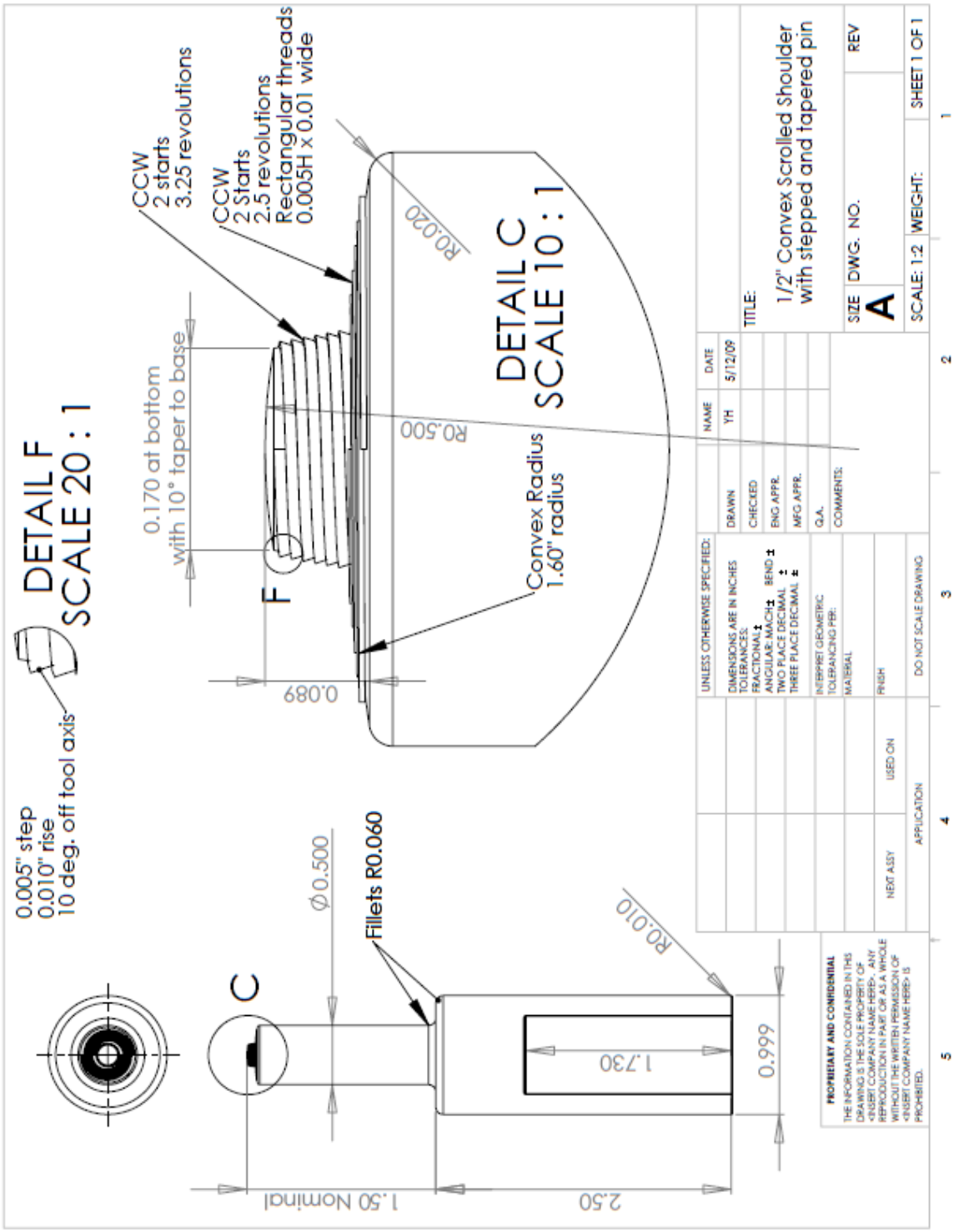
DETAIL F
SCALE 20 : 1
0.005" step
0.010" rise
10 deg. off tool axis
DETAIL C
SCALE 10 : 1
CCW
2 starts
3.25 revolutions
CCW
2 Starts
2.5 revolutions
Rectangular threads
0.005H x 0.01 wide
0.170 at bottom
with 10° taper to base
F
R0.020
R0.500
Convex Radius
1.60" radius
0.089
C
Ø0.500
Fillets R0.060
R0.010
1.730
0.999
1.50 Nominal
2.50
UNLESS OTHERWISE SPECIFIED:
DIMENSIONS ARE IN INCHES
TOLERANCES:
FRACTIONAL ±
ANGULAR: MACH ± BEND ±
TWO PLACE DECIMAL ±
THREE PLACE DECIMAL ±
INTERPRET GEOMETRIC
TOLERANCING PER:
MATERIAL
FINISH
DO NOT SCALE DRAWING
NAME
DATE
DRAWN
YH
5/12/09
CHECKED
ENG APPR.
MFG APPR.
Q.A.
COMMENTS:
TITLE:
1/2" Convex Scrolled Shoulder
with stepped and tapered pin
SIZE
A
DWG. NO.
REV
SCALE: 1:2
WEIGHT:
SHEET 1 OF 1
PROPRIETARY AND CONFIDENTIAL
THE INFORMATION CONTAINED IN THIS
DRAWING IS THE SOLE PROPERTY OF
<INSERT COMPANY NAME HERE>. ANY
REPRODUCTION IN PART OR AS A WHOLE
WITHOUT THE WRITTEN PERMISSION OF
<INSERT COMPANY NAME HERE> IS
PROHIBITED.
NEXT ASSY
USED ON
APPLICATION

Appendix Two: Tool Dimensions for AA6061-T6/Wrought Steel Weld

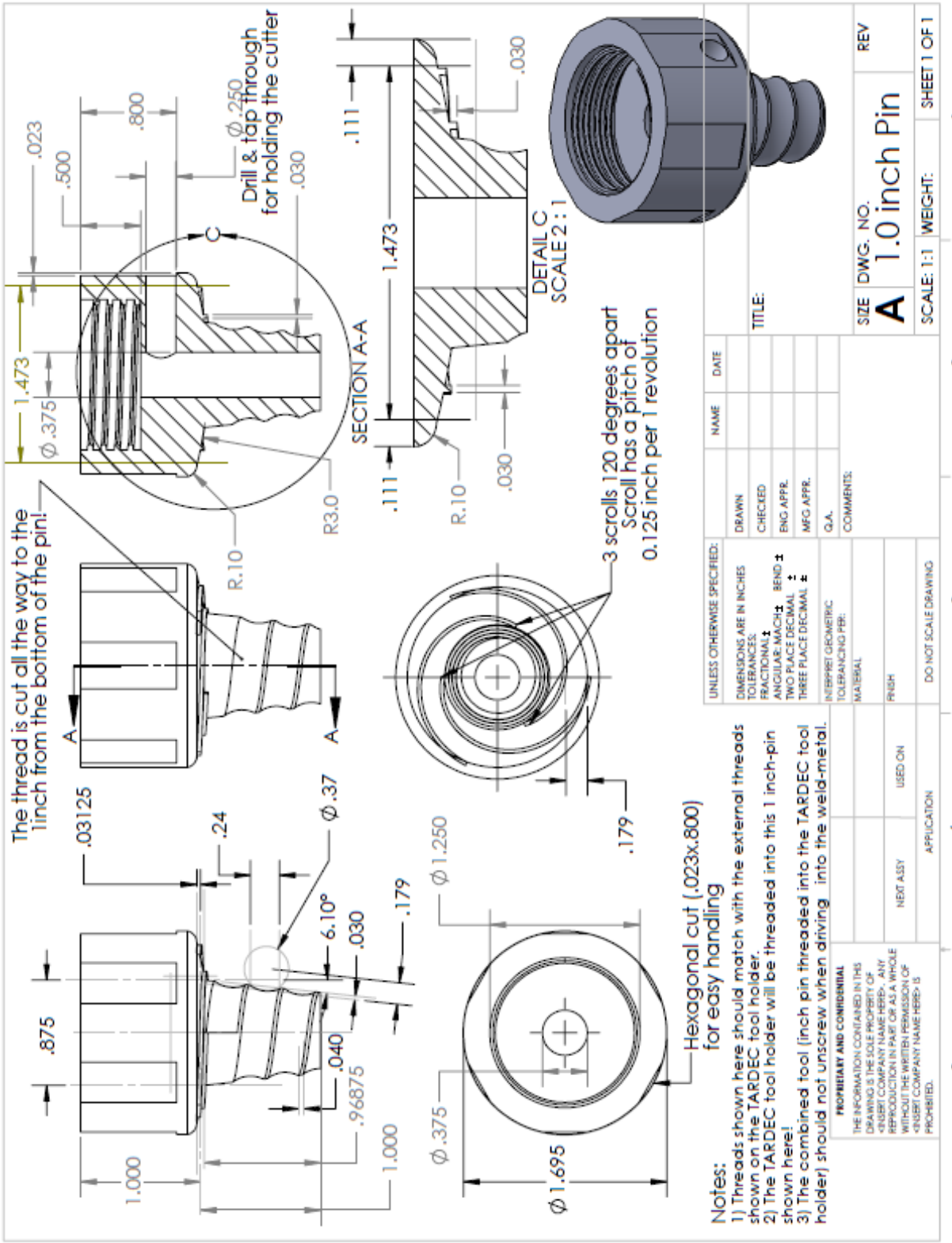
The thread is cut all the way to the 1inch from the bottom of the pin!
.03125
.24
Ø .37
6.10°
.030
.179
.875
.040
.96875
1.000
1.000
Ø 1.250
Ø .375
Ø 1.695
Hexagonal cut (.023x.800) for easy handling
3 scrolls 120 degrees apart
Scroll has a pitch of
0.125 inch per 1 revolution
.179
R.10
R3.0
Ø .375
1.473
.023
.500
.800
Ø .250
Drill & tap through for holding the cutter
.030
C
SECTION A-A
.111
1.473
.111
R.10
.030
.030
DETAIL C
SCALE 2 : 1
Notes:
1) Threads shown here should match with the external threads shown on the TARDEC tool holder.
2) The TARDEC tool holder will be threaded into this 1 inch-pin shown here!
3) The combined tool (inch pin threaded into the TARDEC tool holder) should not unscrew when driving into the weld-metal.
PROPRIETARY AND CONFIDENTIAL
THE INFORMATION CONTAINED IN THIS DRAWING IS THE SOLE PROPERTY OF <INSERT COMPANY NAME HERE>. ANY REPRODUCTION IN PART OR AS A WHOLE WITHOUT THE WRITTEN PERMISSION OF <INSERT COMPANY NAME HERE> IS PROHIBITED.
NEXT ASSY
USED ON
APPLICATION
FINISH
DO NOT SCALE DRAWING
MATERIAL
INTERPRET GEOMETRIC TOLERANCING PER:
UNLESS OTHERWISE SPECIFIED:
DIMENSIONS ARE IN INCHES
TOLERANCES:
FRACTIONAL ±
ANGULAR: MACH ± BEND ±
TWO PLACE DECIMAL ±
THREE PLACE DECIMAL ±
NAME
DATE
DRAWN
CHECKED
ENG APPR.
MFG APPR.
Q.A.
COMMENTS:
TITLE:
SIZE
DWG. NO.
A
1.0 inch Pin
REV
SCALE: 1:1
WEIGHT:
SHEET 1 OF 1

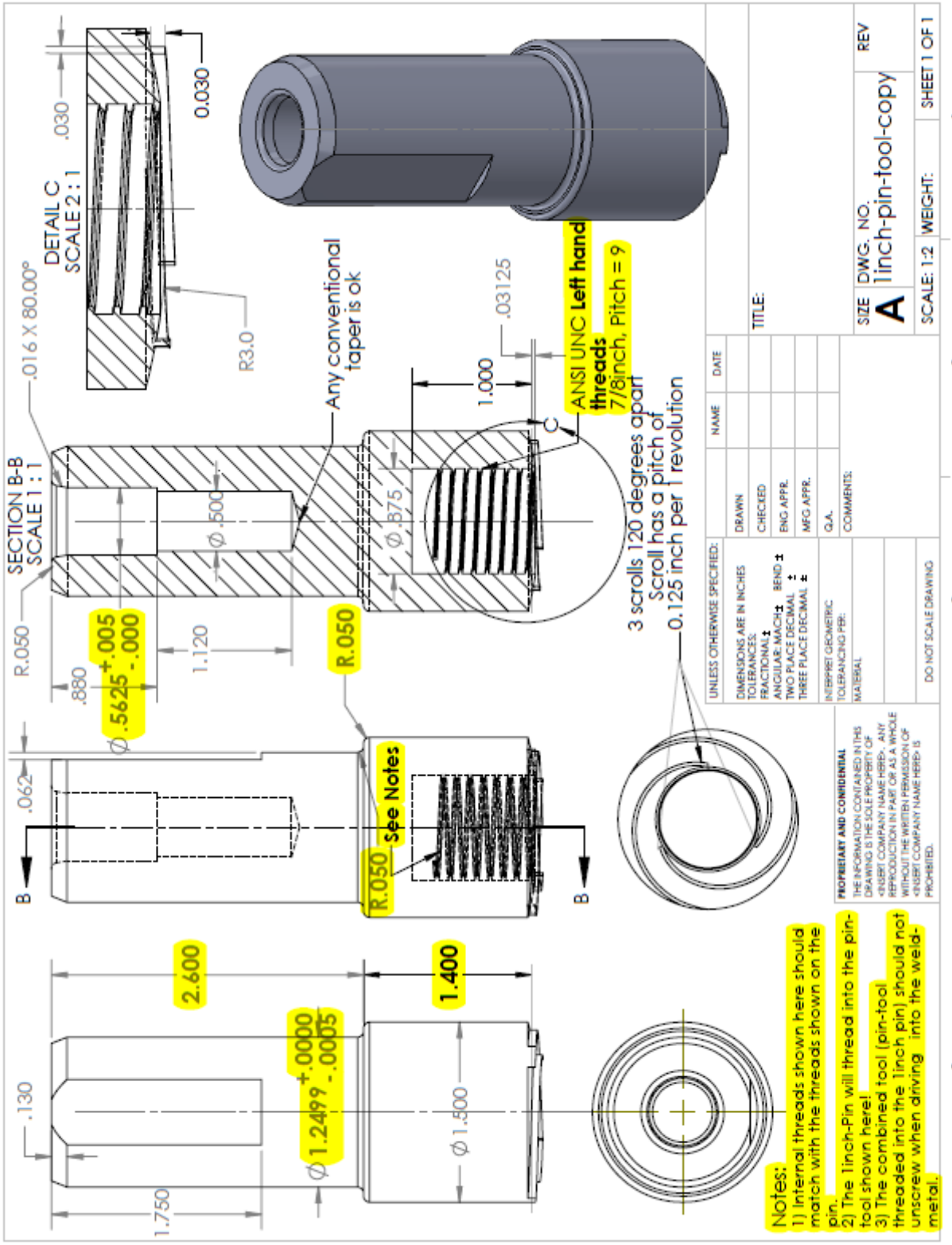
DETAIL C
SCALE 2 : 1
.030
0.030
R3.0
.016 X 80.00°
SECTION B-B
SCALE 1 : 1
R.050
.880
.062
Ø .5625 +.005 -.000
1.120
Ø .500
Any conventional taper is ok
Ø .875
1.000
.03125
C
ANSI UNC Left hand threads 7/8inch, Pitch = 9
3 scrolls 120 degrees apart
Scroll has a pitch of
0.125 inch per 1 revolution
R.050
R.050
See Notes
B
B
2.600
1.400
.130
1.750
Ø 1.2499 +.0000 -.0005
Ø 1.500
Notes:
1) Internal threads shown here should match with the threads shown on the pin.
2) The 1inch-Pin will thread into the pin-tool shown here!
3) The combined tool (pin-tool threaded into the 1inch pin) should not unscrew when driving into the weld-metal.
UNLESS OTHERWISE SPECIFIED:
DIMENSIONS ARE IN INCHES
TOLERANCES:
FRACTIONAL ±
ANGULAR: MACH ± BEND ±
TWO PLACE DECIMAL ±
THREE PLACE DECIMAL ±
INTERPRET GEOMETRIC TOLERANCING PER:
MATERIAL
NAME
DATE
DRAWN
CHECKED
ENG APPR.
MFG APPR.
Q.A.
COMMENTS:
TITLE:
SIZE A
DWG. NO. 1inch-pin-tool-copy
REV
SCALE: 1:2
WEIGHT:
SHEET 1 OF 1
PROPRIETARY AND CONFIDENTIAL
THE INFORMATION CONTAINED IN THIS DRAWING IS THE SOLE PROPERTY OF <INSERT COMPANY NAME HERE>. ANY REPRODUCTION IN PART OR AS A WHOLE WITHOUT THE WRITTEN PERMISSION OF <INSERT COMPANY NAME HERE> IS PROHIBITED.
DO NOT SCALE DRAWING

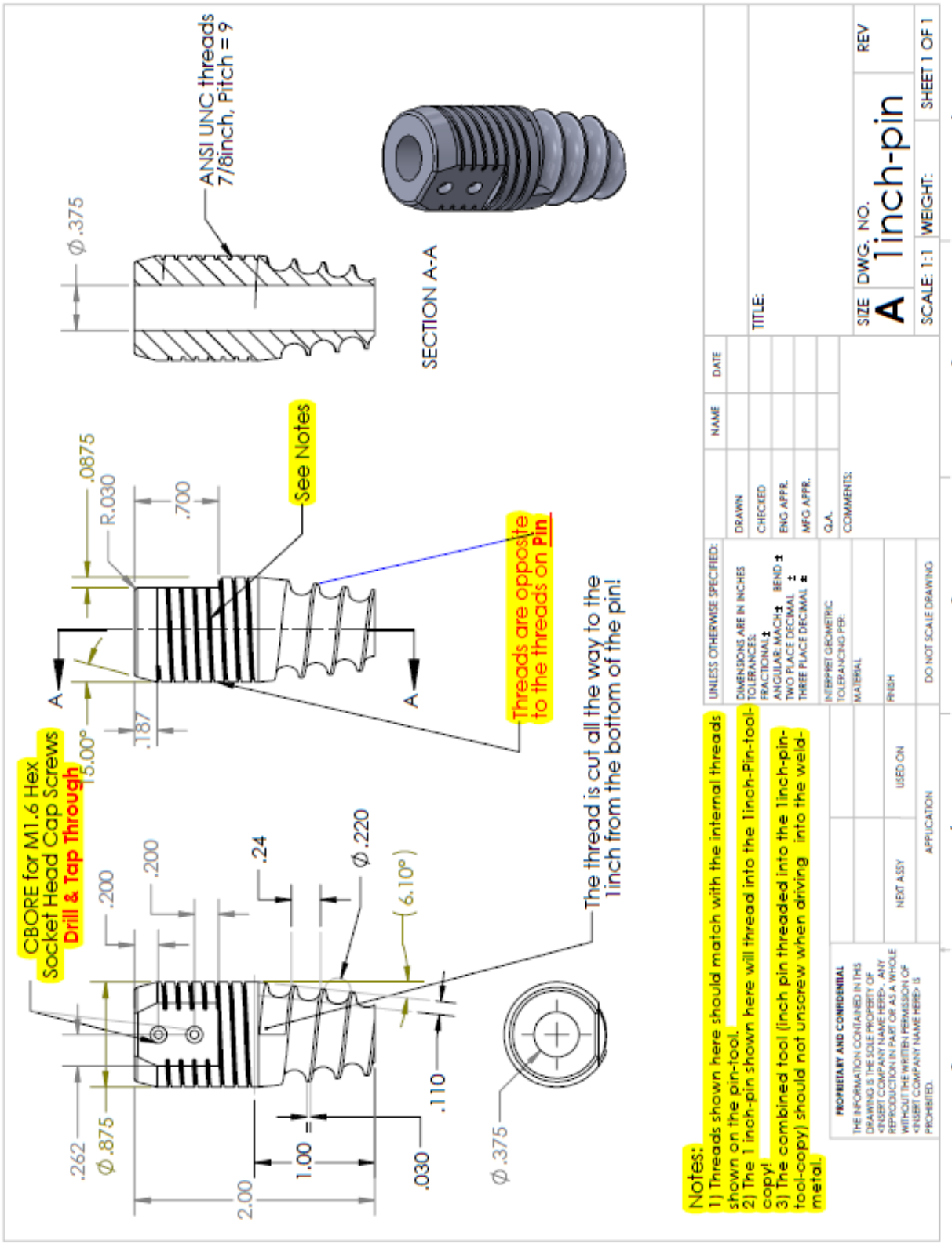
ANSI UNC threads
7/8inch, Pitch = 9
Ø.375
SECTION A-A
CBORE for M1.6 Hex
Socket Head Cap Screws
Drill & Tap Through
.0875
R.030
.700
See Notes
5.00°
.187
A
A
Threads are opposite
to the threads on Pin
The thread is cut all the way to the
1inch from the bottom of the pin!
.200
.200
.24
Ø.220
(6.10°)
.262
Ø.875
2.00
1.00
.030
.110
Ø.375
Notes:
1) Threads shown here should match with the internal threads shown on the pin-tool.
2) The 1 inch-pin shown here will thread into the 1inch-Pin-tool-copy!
3) The combined tool (inch pin threaded into the 1inch-pin-tool-copy) should not unscrew when driving into the weld-metal.
PROPRIETARY AND CONFIDENTIAL
THE INFORMATION CONTAINED IN THIS DRAWING IS THE SOLE PROPERTY OF <INSERT COMPANY NAME HERE>. ANY REPRODUCTION IN PART OR AS A WHOLE WITHOUT THE WRITTEN PERMISSION OF <INSERT COMPANY NAME HERE> IS PROHIBITED.
NEXT ASSY
USED ON
APPLICATION
FINISH
DO NOT SCALE DRAWING
UNLESS OTHERWISE SPECIFIED:
DIMENSIONS ARE IN INCHES
TOLERANCES:
FRACTIONAL ±
ANGULAR: MACH ± BEND ±
TWO PLACE DECIMAL ±
THREE PLACE DECIMAL ±
INTERPRET GEOMETRIC TOLERANCING PER:
MATERIAL
NAME
DATE
DRAWN
CHECKED
ENG APPR.
MFG APPR.
Q.A.
COMMENTS:
TITLE:
SIZE
DWG. NO.
REV
A
1inch-pin
SCALE: 1:1
WEIGHT:
SHEET 1 OF 1

Appendix Three: Grain Size Data

Table 3 Grain size data for 6111 aluminum in AA6111-T4/DP steel weld, measured in OIM Analysis.

6111 Aluminum	Position	Grain Size
Region	mm	sq. µm
RS BM	-6	672.3
RS TMAZ - Equiaxed	-2.5	334.6
RS TMAZ - Elongated	-2.3	12.8
WZ - RS	-1.9	2.78
WZ - RS Center	-1	3.11
WZ - AS Center	0.33	3.78
WZ - AS	1.6	3.67
AS TMAZ - elongated	2.3	30.8
AS TMAZ - equiaxed	2.5	490.6
AS BM	6	672.3

Table 4 Grain size data for 6111 aluminum at mid-depth in AA6111-T4/DP steel weld, measured in OIM Analysis.

6111-T4 Aluminum	Position	Grain Size
Region	mm	sq. µm
RS WZ - Above Hook	-2.5	6.1
WZ Center	-0.3507	7.77
AS WZ - Above Hook	2.44	7.59

Table 5 Grain size data for dual phase steel in AA6111-T4/DP steel weld, measured in OIM Analysis.

DP Steel	Position	Grain Size
Region	mm	sq. µm
RS BM	-6	24.4
RS BM-TMAZ trans	-2.169	7.59
AS BM-TMAZ trans	2.103	9.85
AS BM	6	24.4

Table 6 Grain size data for 6061 aluminum in AA6061-T6/wrought steel weld, measured in OIM Analysis.

6061 Aluminum	Position	Grain Size
Region	**mm**	**sq. µm**
RS BM	-48	5542.5
RS HAZ	-19.5	4980.4
RS TMAZ	-9.5	269.1
WZ - RS Hook	-4	98.4
WZ - RS	-2.5	108.9
WZ - Center	0	107.9
WZ - AS	2.5	106.7
WZ - AS Hook	4.2	91.5
AS TMAZ	8	236.3
AS HAZ	19	5702.8
AS BM	48	6949.1

Table 7 Grain size data for wrought steel in AA6061-T6/wrought steel weld, measured in OIM Analysis.

Wrought Steel	Position	Grain Size
Region	**mm**	**sq. µm**
RS BM	-48	3.2
RS TMAZ	-3.9	0.84
WZ - RS	-2.5	0.079
WZ - Center	0	0.06
WZ - AS	2.5	0.078
AS TMAZ	3.7	1.24
AS BM	48	4

Appendix Four: Steel Particle Volume Fraction Data

Table 8 Volume fraction data for dual phase steel particles in 6111 aluminum WZ.

Row:	A	B	C	D
Y Position:	0.08	0.24	0.4	0.56
X Position	Steel Particle Volume Fraction			
-2.585	-	-	0.1500	0.0511
-2.35	-	-	0.0148	0.0455
-2.115	-	-	0.0084	0.0227
-1.88	0.7500	0.7143	0.0112	0.0227
-1.645	0.7500	0.5000	0.0119	0.0227
-1.41	0.5000	0.5000	0.0164	0.0284
-1.175	0.5000	0.1667	0.0089	-
-0.94	0.8333	0.4444	0.0154	0.0341
-0.705	0.5000	0.4444	0.5000	0.1477
-0.47	0.2667	0.5000	0.1429	0.0385
-0.235	0.0714	0.5000	0.1250	0.0308
0.235	0.0889	0.0345	0.0193	0.0423
0.47	0.1667	0.0260	0.0224	0.0269
0.705	0.1667	0.1270	0.0741	0.0538
0.94	0.0833	0.0281	0.0186	0.0615
1.175	0.0926	0.0109	0.0175	0.0170
1.41	-	0.0085	0.0184	0.0114
1.645	-	-	0.0024	0.0398
1.88	-	-	0.0833	0.0966
2.115	-	-	0.1667	0.0538
2.35	-	-	-	0.0133

Table 9 Volume fraction data for wrought steel particles in 6061 aluminum WZ.

Row:	A	B	C	D
Y Position:	0.4	1.242	2.084	2.926
X Position	Steel Particle Volume Fraction			
-9.285	0.0703	0.0247	0.0612	0.0612
-8.047	0.0722	0.0294	0.0506	0.0459
-6.809	0.0615	0.0318	0.0435	0.0376
-5.571	0.4400	0.1400	0.0765	0.0471

-4.333	0.0793	0.3560	0.2680	0.0576
-3.095	0.0456	0.0565	0.0447	0.0435
-1.857	0.0578	0.0376	0.0553	0.0271
-0.619	0.0601	0.0247	0.0506	0.0400
0.619	0.0374	0.0541	0.0529	0.0412
1.857	0.0820	0.0435	0.0647	0.0329
3.095	0.0482	0.0412	0.2120	0.0400
4.333	0.0356	0.0721	0.0918	0.0412
5.571	0.0323	0.0341	0.0318	0.0847
6.809	0.0232	0.0376	0.2330	0.1150
8.047	0.0415	0.4940	0.0576	0.0424
9.285	0.0310	0.0647	0.0506	0.0635

Appendix Five: Vickers Micro-hardness Data

Table 10 Vickers micro-hardness data from AA6111-T4/DP steel weld.

	Vickers Hardness Number				
	Aluminum			Steel	
X Position	Dist. Above Interface			Dist. Below Interface	
mm	0.5 mm	1.0 mm		0.5 mm	0.25 mm
-9	52	59.9		-	-
-8.5	53.2	59.3		-	126
-8	54	58.4		117	121
-7.5	54.2	59		110	121
-7	53.8	43		107	109
-6.5	50.7	51.6		107	117
-6	49.1	49.4		118	118
-5.5	48.7	46.1		110	129
-5	44	42.2		111	117
-4.5	40.7	41.1		115	118
-4	38.9	41.1		117	113
-3.5	38.4	39.4		116	108
-3	33.6	34.5		116	113
-2.5	35.7	35.3		101	114
-2	46.8	36.6		115	126
-1.5	37.5	38.5		129	150
-1	34.9	36		147	191
-0.5	84.1	174		143	178
0	48.4	229		138	170
0.5	233	32.9		134	168
1	53.6	35.1		139	153
1.5	42.7	33.6		142	162
2	50	34.1		140	145
2.5	-	33.8		127	137
3	36.9	36.4		117	112
3.5	39.4	38		109	106
4	39.2	40.2		121	115
4.5	41.5	41.2		113	115
5	41.1	42.1		110	110
5.5	44	41.6		111	115
6	41.6	43.6		114	116
6.5	46.8	45.1		117	120
7	50.2	47.8		112	121

7.5	51.7	49.3		115	120
8	54.3	52.7		120	111
8.5	54.7	50.7		108	113
9	54.6	52.7		110	118
9.6	56.4	52.7		109	107
10	-	-		110	109

Table 11 Vickers micro-hardness data from AA6061-T6/wrought steel weld.

	Vickers Hardness Number				
	Aluminum				**Steel**
X Position	**Dist. Above Interface**				**Dist. Below Interface**
mm	**0.5 mm**	**1.0 mm**	**6.0 mm**		**0.5 mm**
-48.5	-	-	34.8		-
-48	-	-	34.2		-
-47.5	-	-	33.4		-
-47	-	-	33		-
-46.5	-	-	33.4		-
-46	-	-	32		-
-45.5	-	-	32.7		-
-45	-	-	32.6		-
-44.5	-	-	32.3		-
-44	-	-	31.2		-
-43.5	-	-	31.8		-
-43	-	-	31.7		-
-42.5	-	-	31.7		-
-42	-	-	30.9		-
-41.5	-	-	31.1		-
-41	-	-	32.2		-
-39.5	-	-	31.3		-
-39	-	-	32.4		-
-38.5	-	-	32.3		-
-38	-	-	31.7		-
-37.5	-	-	32.6		-
-37	-	-	32		-
-36.5	-	-	32.5		-
-36	-	-	33.2		-
-35.5	-	-	32		-
-35	-	-	32.2		-
-34.5	-	-	32.3		-

-34	-	-	32		-
-33.5	-	-	32.2		-
-33	-	-	32.5		-
-32.5	-	-	32.1		-
-32	-	-	31.3		-
-31.5	-	-	31.8		-
-31	-	-	31.1		-
-30.5	-	-	30.9		-
-30	-	-	31.3		-
-29.5	-	-	31.4		-
-29	-	-	31.5		-
-28.5	-	-	31.2		-
-28	-	-	32.5		-
-27.5	-	-	31.7		-
-27	-	-	31.3		-
-26.5	-	-	30.3		-
-26	-	-	31.2		-
-25.5	-	-	32.2		-
-25	-	-	31.3		-
-24.5	-	-	31.5		-
-24	-	-	31.5		-
-23.5	-	-	31.2		-
-23	-	-	31.9		-
-22.5	-	-	32		-
-22	-	-	31.7		-
-21.5	-	-	30.7		-
-21	-	-	29.7		-
-20.5	-	-	30.4		-
-20	-	-	30.7		-
-19.5	-	-	29.9		-
-19	-	-	29.1		-
-18.5	-	-	-		-
-18	-	-	-		-
-17.5	-	-	-		-
-17	-	-	-		-
-16.5	-	-	-		-
-16	-	-	-		192
-15.5	-	-	-		194
-15	-	26.9	29.2		189
-14.5	-	26	32.6		184

-14	-	25.9	34.4		190
-13.5	-	26.9	35.7		189
-13	-	28	33.6		192
-12.5	-	31	34		191
-12	-	30.1	31.7		191
-11.5	-	31	32.6		195
-11	-	30.7	31.6		189
-10.5	-	31.3	32.6		189
-10	-	30.2	31.9		189
-9.5	-	30.6	33.1		185
-9	-	30.4	33.3		191
-8.5	-	31.6	33.8		192
-8	-	32.6	34.3		188
-7.5	-	32.7	24.4		194
-7	-	31.1	31.1		199
-6.5	-	31.1	23.9		199
-6	-	31.8	22.9		200
-5.5	-	32.4	23.2		186
-5	-	32.8	23.2		187
-4.5	-	29.2	23		184
-4	-	30.3	23.2		172
-3.5	-	-	24.8		178
-3	26.1	-	22.9		182
-2.5	24.7	29.9	23		158
-2	28	30	23		168
-1.5	25.2	31.8	23		167
-1	24.6	31.6	23.4		167
-0.5	24.4	27.2	23.9		163
0	26.6	28	23.1		163
0.5	27.6	28	23.1		156
1	27.9	29.3	23.4		169
1.5	27.5	26.4	23.3		171
2	28.3	26.9	23.3		166
2.5	26.8	27.3	24.4		169
3	-	27.3	22.6		174
3.5	-	27.8	22.6		173
4	-	-	23		180
4.5	-	-	22.9		186
5	-	33.7	23.2		187
5.5	-	26.9	25.1		185

6	-	26.7	25.3		188
6.5	-	27.2	23.5		179
7	-	26.2	24.5		189
7.5	-	33.2	25.4		190
8	-	34.7	26.2		194
8.5	-	34.4	26.6		193
9	-	38.4	26.7		191
9.6	-	41	24.5		199
10	-	40.9	25.1		195
10.5	-	36.4	23.8		196
11	-	37.9	31.8		197
11.5	-	31	33.3		194
12	-	31.2	36.8		207
12.5	-	30.1	34.4		202
13	-	28.3	36.3		203
13.5	-	26.5	34		199
14	-	26.4	33.8		200
14.5	-	27.3	30.9		206
15	-	25.9	28.1		203
15.5	-	27	27.7		200
16	-	25.4	29.6		190
16.5	-	-	29.4		194
17	-	-	-		194
17.5	-	-	-		-
18	-	-	-		-
18.5	-	-	-		-
19	-	-	-		-
19.5	-	-	-		-
20	-	-	30.4		-
20.5	-	-	31.4		-
21	-	-	32.2		-
21.5	-	-	34.6		-
22	-	-	32.5		-
22.5	-	-	33.7		-
23	-	-	33.1		-
23.5	-	-	34.8		-
24	-	-	32.1		-
24.5	-	-	33.1		-
25	-	-	34.6		-
25.5	-	-	33.7		-

26	-	-	34.6		-
26.5	-	-	36.5		-
27	-	-	32.5		-
27.5	-	-	32		-
28	-	-	32.2		-
28.5	-	-	32.7		-
29	-	-	32.8		-
29.5	-	-	31.7		-
30	-	-	32.2		-
30.5	-	-	32.6		-
31	-	-	32.6		-
31.5	-	-	33.1		-
32	-	-	32.4		-
32.5	-	-	33		-
33	-	-	31.6		-
33.5	-	-	32.6		-
34	-	-	32		-
34.5	-	-	34.2		-
35	-	-	32.4		-
35.5	-	-	33.7		-
36	-	-	33.3		-
36.5	-	-	33.7		-
37	-	-	33.5		-
37.5	-	-	31.9		-
38	-	-	32.6		-
38.5	-	-	32.7		-
39	-	-	32.8		-
39.5	-	-	34.5		-
40	-	-	34.8		-
40.5	-	-	33.1		-
41	-	-	33.6		-
41.5	-	-	33.8		-
42	-	-	33.1		-
42.5	-	-	33.9		-
43	-	-	33.4		-
43.5	-	-	35.7		-
44	-	-	37.1		-
44.5	-	-	34.6		-
45	-	-	34.9		-

Appendix Six: EDS Chemical Analysis Data

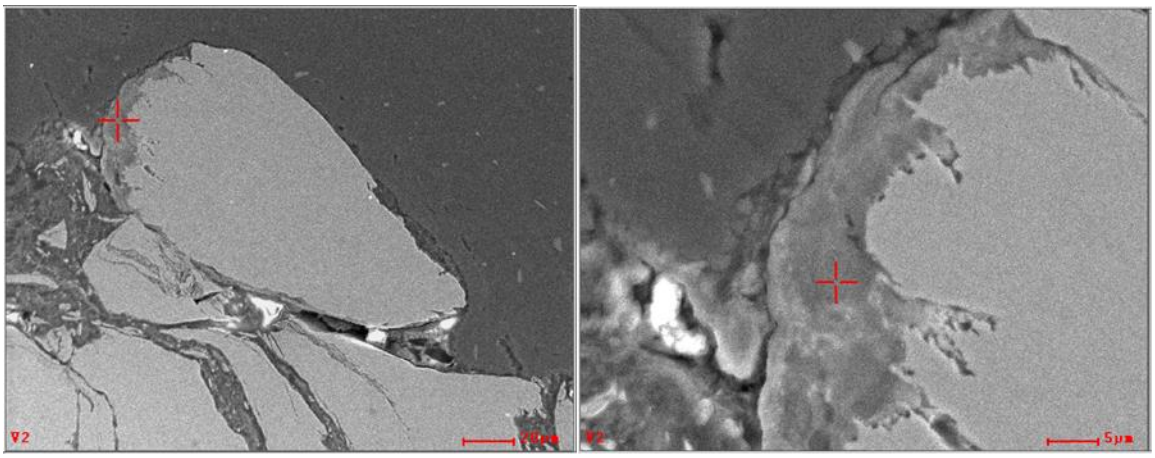

Element	Wt %	At %
AlK	56.00	73.85
FeK	23.78	15.15
ZnK	20.21	11.00

Figure 52 Particle inside RS hook, WZ, AA6111-T4/DP steel weld, 2000x (right).

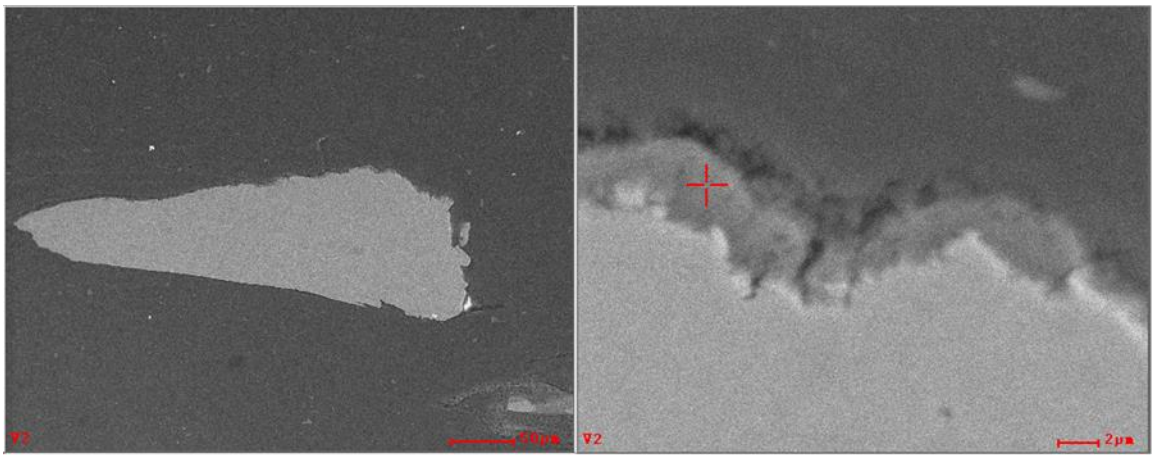

Element	Wt %	At %
AlK	62.26	78.46
FeK	21.49	13.08
ZnL	16.26	8.46

Figure 53 Particle in WZ, AA6111-T4/DP steel weld, 4000x (right).

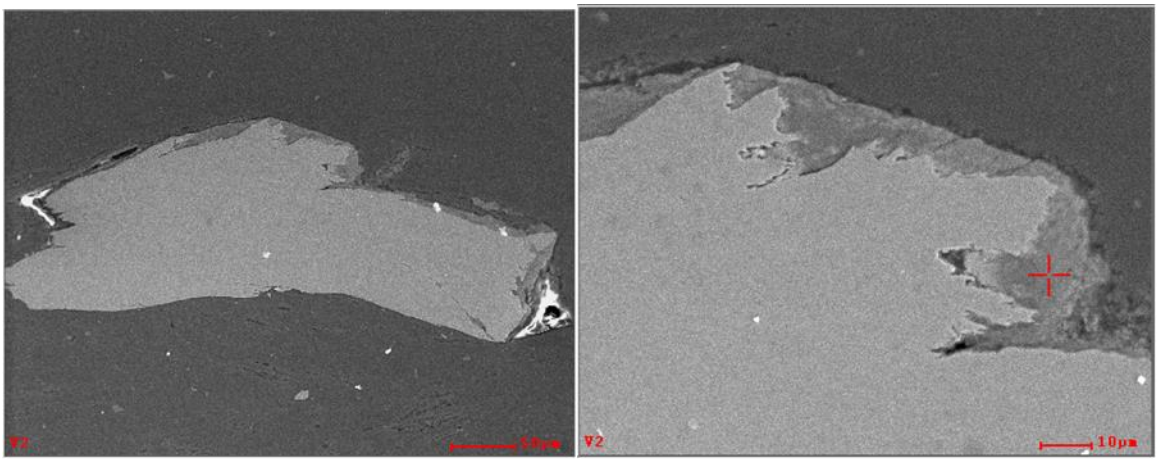

Element	Wt %	At %
AlK	54.35	72.42
FeK	26.44	17.02
ZnK	19.21	10.56

Figure 54 Particle above AS hook, WZ, AA6111-T4/DP steel weld, 1000x (right).

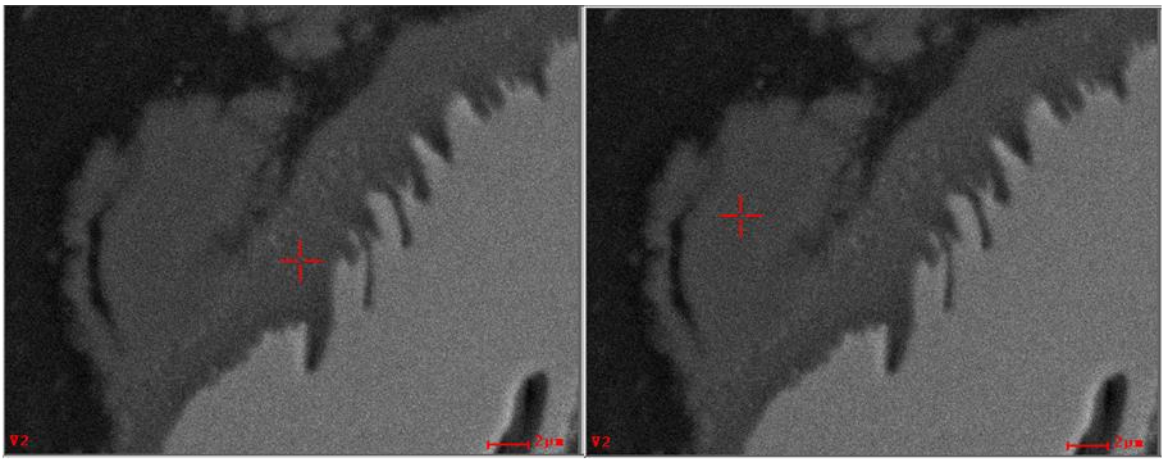

Element	Wt %	At %
AlK	63.00	77.90
FeK	37.00	22.10

Element	Wt %	At %
AlK	67.78	81.33
FeK	32.22	18.67

Figure 55 Particle on AS of WZ, AA6061-T6/wrought steel weld, 4000x.

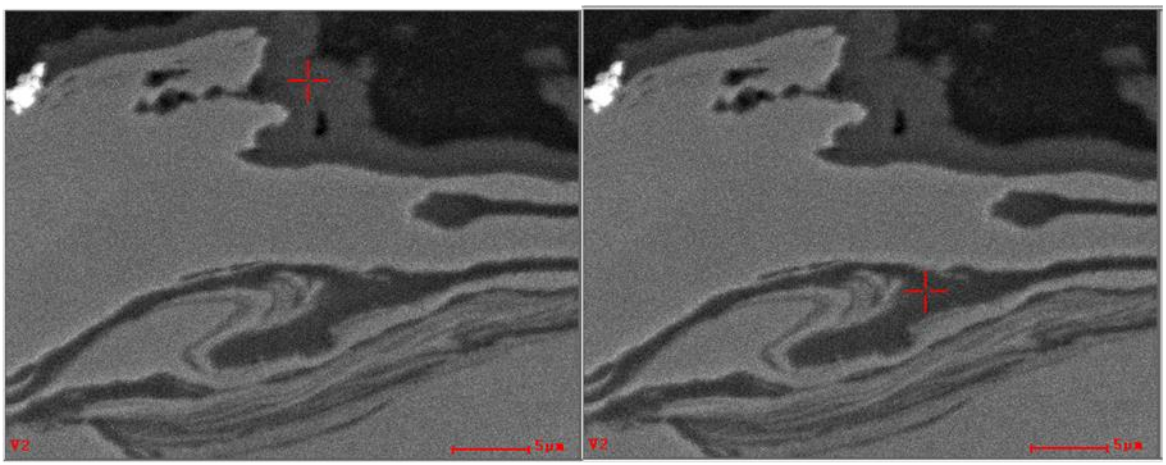

Element	Wt %	At %
AlK	69.46	82.48
FeK	30.54	17.52

Element	Wt %	At %
AlK	60.74	76.20
FeK	39.26	23.80

Figure 56 Weld interface, inner corner of AS hook, AA6061-T6/wrought steel weld, 3000x.

Appendix Seven: EBSD Data

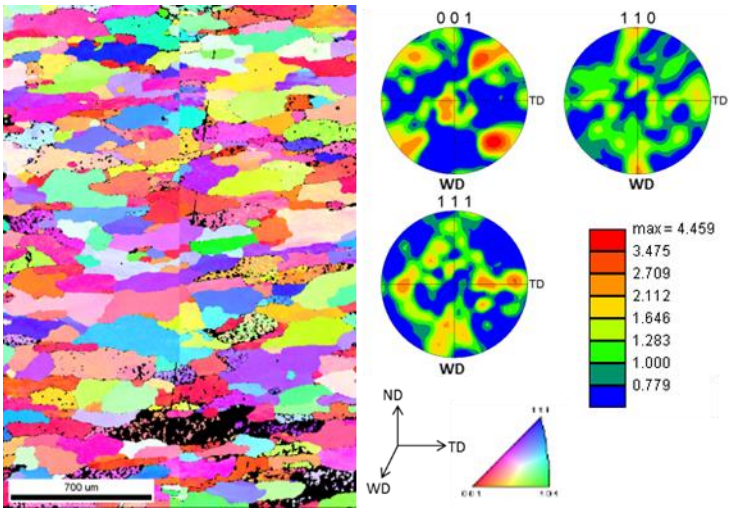

Figure 57 AA6061-T6 AS BM grain orientation maps and PFs showing FCC rolling texture.

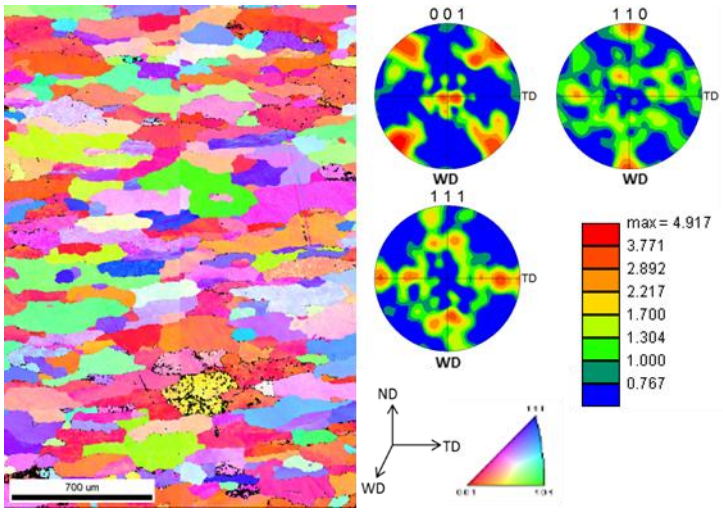

Figure 58 AA6061-T6 AS HAZ: grain orientation and PFs showing texture similar to FCC rolling texture.

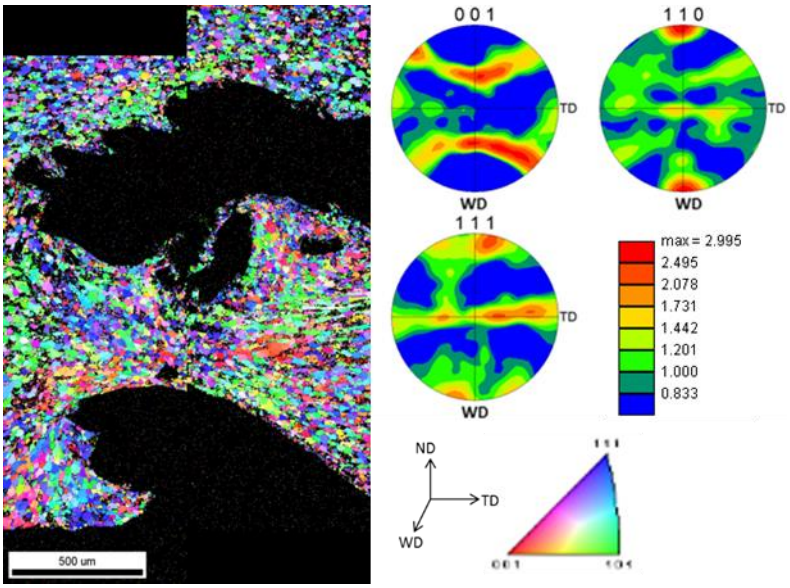

Figure 59 AA6061-T6 WZ around RS hook. {111} PF in (C) shows partial B-fiber with the SPN rotated slightly CCW from being aligned with TD.

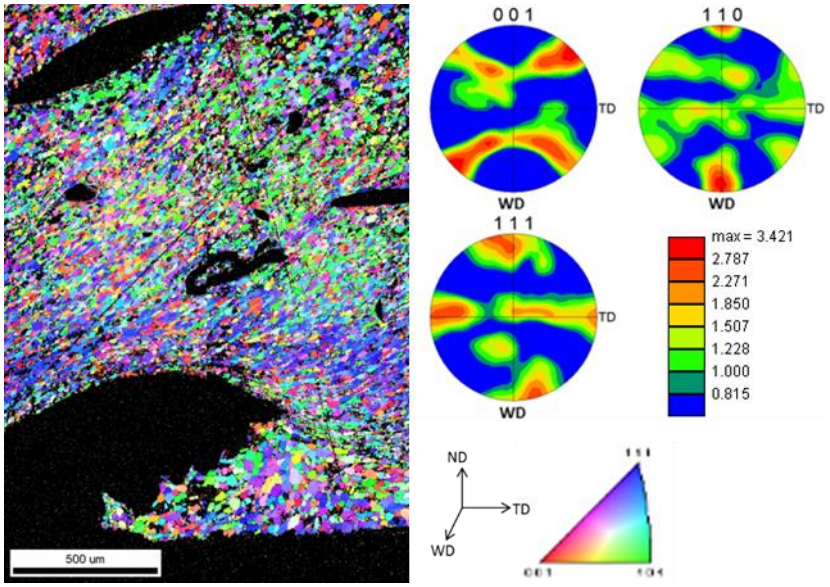

Figure 60 AA6061-T6 WZ around AS hook. {111} PF in (C) shows partial B-fiber with the SPN aligned with TD.

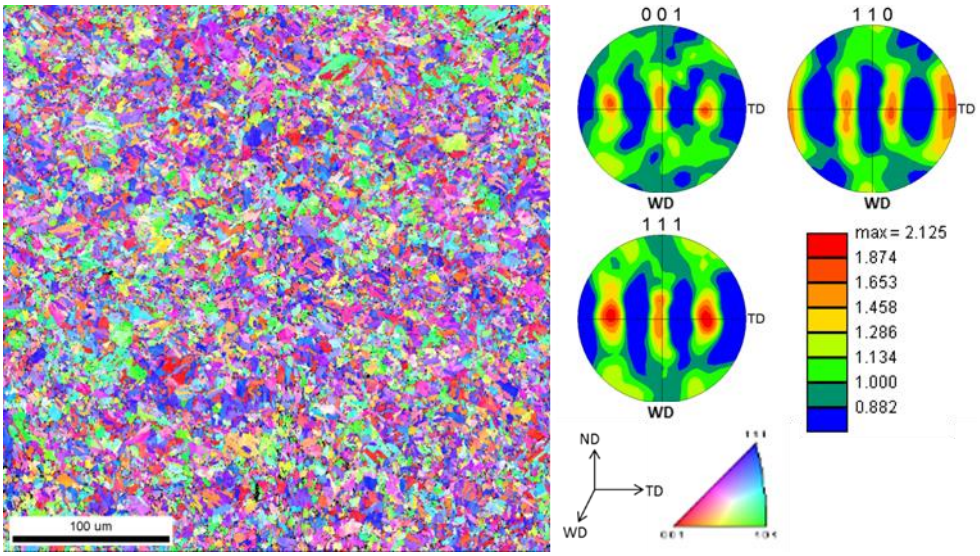

Figure 61 Wrought steel RS BM: BCC rolling texture, with RD of the steel plate normal to WD.

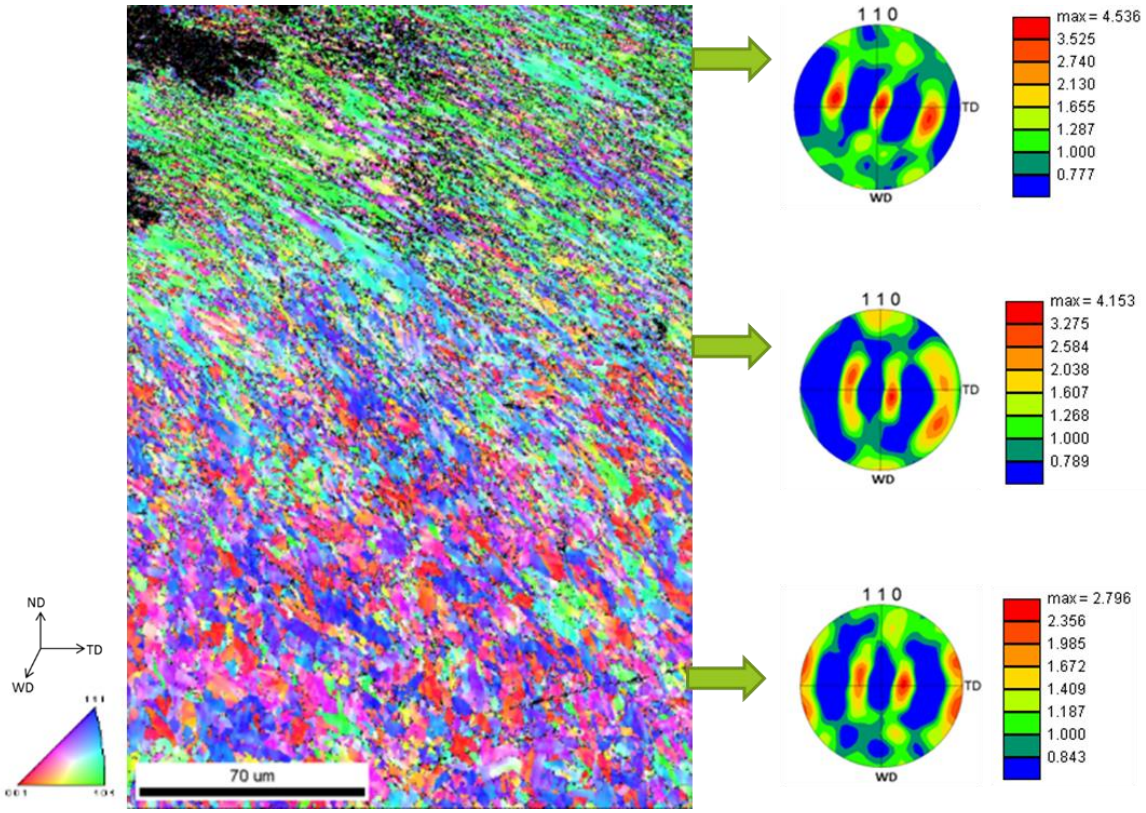

Figure 62 Wrought steel RS TMAZ showing textures that vary with degree of grain elongation.

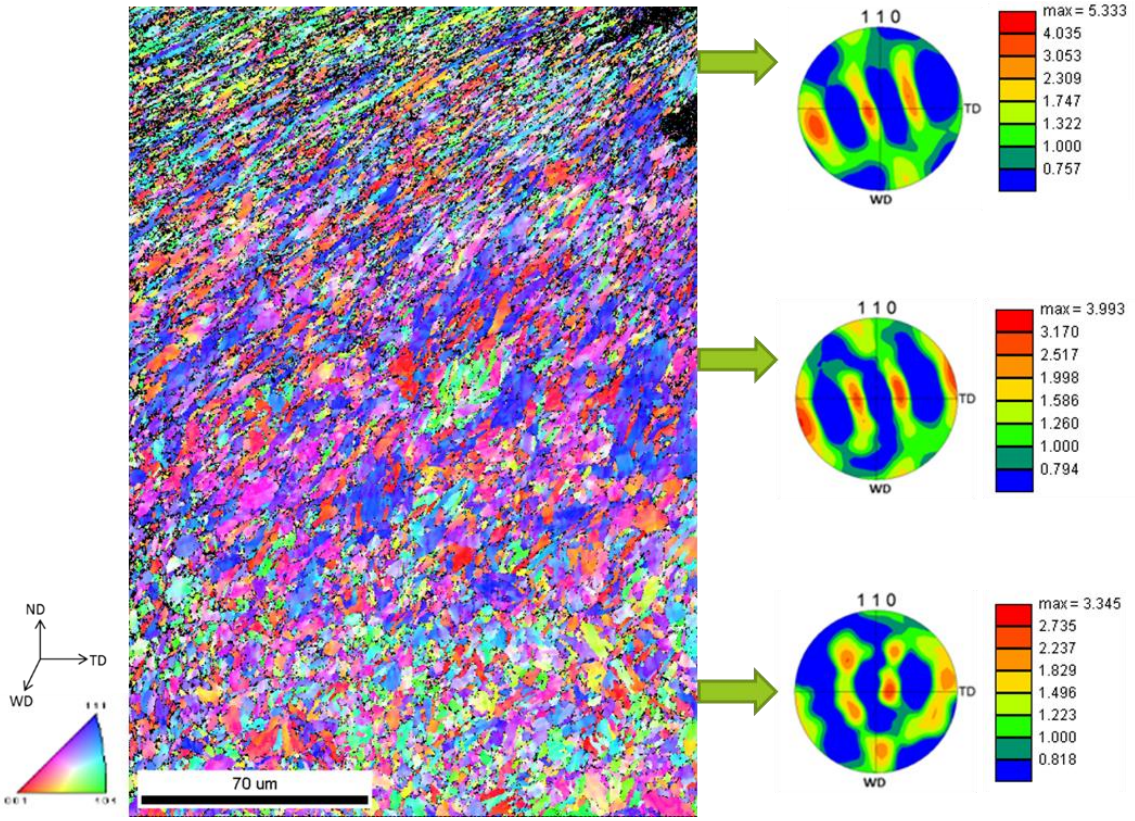

Figure 63 Wrought steel AS TMAZ showing textures that vary with degree of grain elongation.